Numerical Modeling of Post-Seismic Displacement Fields

Von der Fakultät für
Bauingenieur- und Vermessungswesen
der Universität Stuttgart
zur Erlangung der Würde eines
Doktor-Ingenieurs (Dr.-Ing.)
genehmigte Abhandlung

vorgelegt von
M.Sc. Amir M. Abolghasem
aus Tehran, Iran

Hauptberichter:	Prof. Dr.-Ing. habil. Dr. tech. h.c. mult., Dr.-Ing. E.h. mult. E. W. Grafarend
Mitberichter:	Prof. Dr. rer. nat. habil. D. Wolf, Geoforschungszentrum Potsdam
	Prof. Dr.-Ing. E. Groten, Technische Universität Darmstadt

Tag der mündliche Prüfung: 16.August 2000

Geodätisches Institut der Universität Stuttgart

2001

0.1 ABSTRACT

In order to investigate the deformations of the earth under the application of different force fields, several models have been set forth and led to interesting results. Surface loads and earthquakes are two examples of the force fields which have drawn attention in this respect. Since the main purpose of the author when he started this work was the representation of post-seismic surface displacement fields, the present thesis refers more often to that class of applications. In spite of it, the intention to test the method and bench mark one solution by comparison with a present solution, encouraged the author to compute the displacement field under a simple distributed surface load.

In studying the deformations induced by fault motions since STEKETEE [1958] introduced dislocation theory, numerous analytical formulations have been developed. In each new model either a more complicated force field is applied or consideration of more effects in the model has made it more realistic. The deformation source ranges from a point surface source to inclined internal faults. The earth models started from a non-gravitational, homogeneous, isotropic, linear, elastic, semi-infinite, planar model, i.e. elastic half-space, then more effects were taken into account. Earth curvature, surface topography, stratification, lateral heterogeneity, and compressibility are the specifications of the real earth which have been applied in the models one after another. Some of them are still subject of important researches, the complications introduced by lateral inhomogeneity and compressibility effects have not been solved completely yet.

At the same time when scientists have been trying to overcome the present problems in their analytical models step by step, computational ability has broken out and is flying at a speed which nobody could even dream of two decades ago. The present computer power in speed and in storage, moreover our expectation of its future, have drawn the attention of many scientific fields. Numerical methods are propagating to every discipline which is in one or the other way involved with computations.

Yet unsolved problems in the earth deformation analysis, and on the other hand the growth of numerical methods motivated the author to apply the finite element method as the proper numerical technique for the problem of interest and check its output.

The finite element technique is flexible enough to

- model lateral, in addition to radial, heterogeneities,
- include internal discontinuities,
- apply geodetic observations as boundary conditions.

This study presents the results of the application of finite element technique to the earth deformation analysis under specified force fields. Different numerical earth models are specified in which various physical properties are discussed. A homogeneous model, radially non-homogeneous models, one without lithosphere, one with 50 km thick lithosphere, another one with 150 km thick lithosphere, and one model with lateral variation of lithosphere thickness are discussed in the following.

For the finite element computation, the software package *ABAQUS* was applied.

0.2 ZUSAMMENFASSUNG

Um die Deformationen der Erde unter der Einwirkung verschiedener anregender Kraftfelder, z.B. Oberflächenlasten und Erdbeben zu untersuchen, werden mehrere Modelle aufgestellt, die zu hochinteressanten Ergebnissen führen. Obwohl das Hauptanliegen der Arbeit in der Darstellung postseismischer Verschiebungsfelder besteht und sich damit vor allem mit dieser Klasse von Anwendungen beschäftigt, wird - aus der Motivation heraus, die Methode durch Vergleich mit bestehenden Lösungen zu testen - auch das Verschiebungsfeld bei Einwirkung einer einfachen Oberflächenlast berechnet.

Seit der Einführung der Dislokations-Theorie durch STEKETEE [1958] sind zahlreiche analytische Formulierungen zur Beschreibung seismischer Deformationen entwickelt worden, wobei jedes nachfolgende Modell aus Gründen stärkerer Realitätsnähe entweder eine kompliziertere Anregungsfunktion als das vorhergehende verwendet oder weitergehende Effekte berücksichtigt. Die angesetzten Anregungen reichen dabei von punktförmigen Oberflächenlasten bis zu geneigten inneren Verwerfungen.

Das einfachste untersuchte Erdmodell besteht aus einem nichtgravitierenden, homogenen, isotropischen, linearen, elastischen, semi-unendlichen und ebenen Modell, d.h. dem sog. elastischen Halbraum. Die darauf aufbauenden komplizierteren Modelle berücksichtigen dann auch die Eigenschaften der realen Erde, wie z.B. Erdkrümmung, Oberflächentopographie, Schichtung, laterale Inhomogenität und Kompressibilität. Einige

dieser Eigenschaften sind derzeit Gegenstand aktueller Forschungsarbeiten; so sind z.B. die durch laterale Inhomogenitäten und Kompressibilität hervorgerufenen Fragestellungen bisher noch völlig ungeklärt.

Glücklicherweise sind die bei der Anwendung analytischer Methoden auftretenden Probleme inzwischen durch die erhebliche Fortentwicklung der Computer überwunden worden. In fast allen Bereichen der Wissenschaft werden heutzutage analytische Verfahren durch numerische Verfahren ergänzt oder sogar vollständig ersetzt. Diese fortschreitende Entwicklung numerischer Methoden ermöglichen es nun, die Technik der Finiten Elemente bei den bisher ungelösten Problemen in der Erddeformationsanalyse anzuwenden. Die Vorteile sind beträchtlich: Es können nämlich

- zusätzlich zu den radialen auch laterale Inhomogentäten formuliert,
- innere Diskontinuitäten berücksichtigt und
- Geodätische Beobachtungen als Randbedingungen eingebracht

werden.

Die vorliegende Arbeit präsentiert die Ergebnisse des Einsatzes der Finite-Elemente-Technik in der Erddeformationsanalyse unter Berücksichtigung vorgegebener Kraftfelder. Es werden verschiedene numerische Erdmodelle spezifiziert und deren unterschiedliche physikalischen Eigenschaften diskutiert: (i) homogenes Modell, (ii) radial inhomogenes Modell (ohne Lithosphäre, mit 50 km bzw. 150 km dicker Lithosphäre) und (iii) Modell mit lateralen Variationen der Lithosphärendicke. Alle Berechnungen wurden mit dem Softwarepakt *ABAQUS* durchgeführt.

0.3 ACKNOWLEDGMENTS

In completion of this work I am indebted to

- the Ministry of Culture and Higher Education of the Islamic Republic of Iran for its financial support,
- my supervisor Prof. Dr.-Ing. mult. Erik Grafarend who has established a nice research environment at his institute,
- Dr.-Ing. Johannes Engels of the Geodetic Institute, Stuttgart University, for his scientific guidance,
- last not least my wife, who got along with a student's life for more than a decade, for her tolerance and encouragement.

Contents

Chapter 1

INTRODUCTION

The deformation of the earth has been the subject of study of various disciplines for long time. The equation of motion for an elastic body was formulated already by Navier in 1821. In the following two centuries, the solution techniques developed further, great steps were taken ahead, but we still face unsolved problems. The theory of elasticity has played a key role in this field, wherever the instantaneous deformations are sought, or when the deformations after the application of the force fields are vanishing, otherwise viscoelasticity theory is the proper tool to investigate the deformations.

Both theories, elasticity and viscoelasticity, lead to partial differential equations to be solved for the earth, which is a difficult task in general.

1.1 A Historical Review of Dislocation Theory

In the following we try to present an overview of the developing process of dislocation theory, and a few special cases of earth modeling in general, although this can't be a complete historical review, since many authors have worked on different models with various specifications.

Since STEKETEE [1958] introduced the basic idea of dislocation theory in a semi-infinite elastic medium, lots of efforts have been performed to develop this theory further, and represent the earth by more accurate models. CHINNERY [1961,1963] derived analytical solutions for displacement field of a rectangular dislocation source in an elastic half-space, in particular the displacements on the surface of a medium caused by a strike-slip fault. SMYLIE and MANSINHA [1971] generalized the theory of dislocation to real earth models by taking into account: (i) self-gravitation, (ii) radial variation of elastic properties, density and gravity, (iii) initial hydrostatic stress, and (iv) the presence of liquid core. CHINNERY and JOVANOVICH [1972] calculated displacement fields due to vertical strike-slip fault for earth models of up to two layers over a half-space, and studied the correlation of the complications with structure and distance from the fault. JOVANOVICH et al. [1974a,b] examined the effect of the earth structure on earthquake displacement, strain and tilt fields on the earth surface due to a point source in a multi-layered elastic half-space. RUNDLE and JACKSON [1977] developed an analytic expression for the Green function of displacement due to a strike-slip point source in an elastic layer over a a viscoelastic half-space, the point source solution can be integrated over the surface of a finite fault. COHEN [1979] proposed a model for post-seismic surface deformation by attributing them to lithospheric and asthenospheric viscoelasticity, and studied the effect of each of the two layers, he also computed the stress changes due to the same source [1980a]. BOUCHON [1981] reported a method to calculate the Green function for elastic layered media, and applied the method to the cases of a vertical point source, horizontal point source and horizontal shear dislocations. DZIEWONSKY and ANDERSON [1981] made an inversion of 1000 normal mode periods, 500 summary travel times, 100 normal mode Q values, mass and moment of inertia, obtained radial distribution of elastic properties, Q values and density in the earth's interior, and introduced the Preliminary Reference Earth Model (*PREM*). IWASAKI and MATSU'URA [1981] computed quasi-static strains and tilts for a dislocation source in a stratified elastic half-space with an intervenient Maxwellian viscoelastic layer. OKADA [1985] presented a complete set of solutions for surface displacements, strains and tilts due to inclined shear and tensile faults in a half-space for point and finite rectangular sources. BONAFEDE et al. [1986] calculated ground deformation on a viscoelastic half-space for center of dilatation and pressure source. KAGAN [1987a,b] classified all possible elementary sources of internal deformation in an elastic solid. ROTH [1990] used the theory of dislocation to model deformation on the surface of a layered half-space, and extended the method to calculate deformation inside the medium. SUN [1992] studied the potential and gravity changes caused by dislocations in spherically symmetric earth models, and discussed shear dislocations of vertical strike-slip, vertical dip-slip, dip-slip at a 45° dipping plane and a tensile opening and explosion. OKUBO [1993] presented a reciprocity theorem between the static deformation excited by a point dislocation in a SNREI (Spherical Non-Rotating Elastic Isotropic model), and those generated by external forces such as tides, loads and surface shear forces. ROTH [1993] proposed a detailed review of recent developments and the state of the art concerning three dimensional models for crustal deformation in layered media. SUN and OKUBO [1993] continued their earlier works in studying potential and gravity changes caused by dislocations in spherically symmetric earth models, and compared the gravity changes due to dislocation in (i) flat earth models, (ii) homogeneous spheres, and (iii) layered sphere. PAVLOV [1994a,b] showed that the inverse problem of seismic source theory for a general source type distributed over a three dimensional spatial region in infinite homogeneous isotropic medium has no unique solution, and based his discussion on the equivalent force [PAVLOV 1994a] and polynomial moments [PAVLOV 1994b]. PIERSANTI et al. [1995] quantified the effects of post-seismic deformation on the radial and horizontal components of displacement, in the near and far fields of strike- and dip-slip point dislocations, embedded in the elastic layer of a spherical self-gravitating stratified viscoelastic earth. BENNETT et al. [1996] divided a homogeneous elastic half-space to vertical blocks in contact along vertical planar boundaries. FERNANDEZ et al. [1996a,b] modeled dipping faults with various angles in different depths of a model with an elastic gravitational layer overlying a viscoelastic gravitational half-space, and computed horizontal and vertical displacements. SUN et al. [1996] defined dislocation Love numbers and Green functions to study elastic deformation of the earth caused by a point dislocation in a radially heterogeneous spherical earth model, and derived spherical harmonic expansion for the shear and tensile dislocations of four independent solutions. VERMEERSEN et al. [1996a,b] presented an outline of the analytical method of general radially stratified n-layer self-gravitating Maxwell rheological models. POLLITZ [1997] investigated viscoelastic relaxation of a ductile asthenosphere underlying a purely elastic plate in a gravitational compressible spherical layered viscoelastic rheology, and presented approximations suitable for near-field calculations. SABADINI and VERMEERSEN [1997] applied normal mode theory to a class of multi-layered viscoelastic earth models based on PREM, with an incompressible linear viscoelastic Maxwell rheology and modeled co- and post-seismic deformation. SOLDATI et al. [1998] computed gravitational perturbation due to a lithospheric shear dislocation in the co- and post-seismic regimes of a spherically symmetric earth model with a viscoelastic mantle and an inviscid core. MARTINEC and WOLF [1999] presented a semi-analytical solution to the two dimensional forward modeling of viscoelastic relaxation in a heterogeneous model consisting of eccentrically nested spheres.

1.2 Geodetic Data of Deformation

In parallel to the theoretical development of dislocation theory and earth modeling, geodetic methodology has made great steps in both theoretical direction and observation technology. Satellite Laser Ranging (SLR), Very Long Base Line Interferometry (VLBI) and Global Positioning System (GPS) are now common techniques to detect earth's surface displacements, e.g. in the vicinity of faults and plate boundaries. Comparing to tiltmetry, KOSTROV and DAS [1988] wrote:

> "*geodetic measurements, which are representative of larger areas, are a better means of studying tectonic strains.*"

Quantifying the effects of post-seismic deformation on the different components of displacement vector due to various dislocation sources, PIERSANTI et al. [1995] conclude that:

> "*VLBI techniques, with a precision of a few parts per billion over distances of* 1000 *km, can detect global post-seismic deformation induced by large earthquakes.*"

JACKSON et al. [1997] stated that:

> "*combined with detailed models relating earthquake occurrence to strain and stress accumulation, such geodetic observations may also help to identify the places where earthquakes are most likely in the next few decades.*"

SEGALL and MATTHEWS [1997] argued that:

> "*the recent expansion of permanent Global Positioning System (GPS) networks provides crustal deformation data that are dense in both space and time.*"

Japan paid considerable attention to this fact, and established nearly 1000 GPS sites in an average spacing of about 20 km [Miyazaki et al. 1997].

Many authors have documented geodetic measurements in seismic active areas, and in most cases they have interpreted the results to gain information about the geometry of the fault(s). Matsu'ura and Tanimoto [1980] applied co-seismic geodetic data of the Kanto earthquake of 1923, derived a fault model in an elastic dilatational but Maxwell deviatoric half-space, based on the derived model of the fault, they computed post-seismic vertical displacements and compared with the crustal movements of the period 1931-1950. Barrientos and Ward [1990] used 166 sea level data, 130 elevation differences and 16 horizontal strains for the 1960 Chilean earthquake on a Uniform Slip Planar (USP) and a Variable Slip Planar (VSP) faults in an elastic half-space, and analyzed fault slip patterns. Lisowski et al. [1990] derived geometry and orientation of a fault which best fits to the geodetic co-seismic data of Loma Prieta, California, the earthquake of 1989. Yoshida and Koketsu [1990] developed a simultaneous inversion method of strong motion seismograms and geodetic data for inferring earthquake rupture process, and applied their method to the 1984 earthquake of Naganoken, Seibe, Japan. Arnadottir et al. [1991] presented a non-linear inversion procedure of geodetic data to obtain elastic dislocation in a homogeneous half-space, applied the method to the 1989 earthquake of Kilauea, and concluded that a realistic structure is important to estimate source geometry from geodetic data. Williams et al. [1993] used GPS survey of co-seismic displacements in the epicentral region of the 1989 Loma Prieta earthquake, and estimated the parameters of a uniform rectangular dislocation. Arnadottir and Segall [1994] calculated the geometry of the fault and the distribution of slip for the the 1989 Loma Prieta earthquake based on the inversion of EDM, GPS, VLBI and elevation angle measurements. Johnson and Wyatt [1994] investigated the optimal design of geodynamics geodetic networks, due to the growth of highly accurate geodetic measurements. Anzidei et al. [1996] used repeated measurements of a GPS network of 9 sites crossing the Ionian sea from Calabria (Southern Italy) to Northwestern Greece, and detected significant changes in the positions of 5 sites. Bennett et al. [1996] computed slip rates of the north America plate boundary in Southern California and Northern Mexico, based on repeated GPS measurements and their half-space model with vertical blocks (§1.1). Duquency et al. [1996] applied geodetic trilateration and GPS in July 1991 and September 1994, and analyzed the co-seismic deformations in the vicinity of the Southern Great Sumatran Fault (GSF) due to the February 1994 earthquake. Bock et al. [1997] reported the results of the great effort of the Southern California Permanent GPS Geodetic Array (PGGA), established in 1990 to continuously monitor crustal motions. Bürgman et al. [1997] analyzed the GPS and leveling measurements collected in 5 years after 1989 Loma Prieta earthquake to investigate the post-seismic motion, and concluded that the pre-seismic motions were accelerated by the earthquake. Segall and Matthews [1997] introduced a network inversion filter in order to inverse GPS data for crustal deformations in frequently sampled geodetic networks, for estimating the distribution of fault slip in space and time. Wdowinski et al. [1997] applied the observations of 7 sites in the area of the 1992 earthquake of Landers, being observed for 100 days centered on the day of the earthquake, computed the co- and post-seismic displacements and compared with the results of the dislocation problem. Jackson. et al. [1977] discussed the application of triangulation, laser measurements of line length, VLBI and GPS to identify faults that lack clear evidence on the surface, and to determine the rate of motion on the faults. Zhang et al. [1997] analyzed time series of daily positions estimated from the data collected by 10 continuously monitoring GPS sites in Southern California during a 19 month period 1992-1994. Kato et al. [1998] used data from a Japan nationwide continuous GPS network to estimate crustal strains in the Japanese islands. Hunstad et al. [1999] proposed a dislocation model for the two normal faulting earthquakes that struck the Umbria-March, Italy, in 1997, they concluded a geometry of the faults and the ruptures which best fits to the co-seismic displacements observed by GPS. Kenner and Segall [2000] reevaluated triangulation data from Northern California following 1906 San Francisco earthquake, calculated uniform shear strain rates and average station velocities. With the addition of recent geodetic data they inferred an effective relaxation time for long term post-seismic deformation following the 1906 earthquake.

It can be concluded that building up geophysical models without the application of geodetic data is only a theoretical study of how a model of the earth behaves, while collection of geodetic data monitors the surface motions of the real earth, and is by itself not sufficient to investigate the generating mechanism of the motions. Application of geodetic data to geophysical models is the proper way of understanding the real earth behavior. As a matter of fact geodetic data convey the behavior of the real earth to the purely theoretical models, and make a bridge between the real earth and the model earth.

1.3 Application of Numerical Techniques to Compute Deformations

Parallel to the analytical solutions, numerical techniques, e.g. the method of finite elements, have been developed to deal with the equations whose solutions demand an advanced mathematical treatment, if solvable at all. However, these techniques did not spread before the break through of the computational ability.

Advent of new computers and their growth and popularity, brought about more power of numerical computation therefore more attention is drawn to numerical techniques. Analysis of geodetic data and earth deformation are not exceptions to this rule. GRAFAREND [1977] constructed a displacement field characterized by translation, rotation and strain tensors based on the method of finite elements, he derived stress-strain relations, especially of local, homogeneous and isotropic type. SZAMEITAT [1979] built up a numerical model of elastic earth, based on elements of spherical layers. GRAFAREND [1986] represented the local strain and local rotation in terms of irregularly shaped three dimensional finite elements which reflected the structure of a geodetic network. BONAFEDE et al. [1986], in computing the ground deformations of a center of dilatation and pressure source in a viscoelastic half-space, and its application in the volcanic area of Campi Flegrei, Italy, concluded:

> "*the presence of two layers with different rheological properties makes the analytical solution difficult to find out and one must finally resort to numerical technique.*"

The available software and hardware of today let us go much further in complexities of the models, so that consideration of *lateral variations* of the earth material is not a far distance aim any more.

1.4 Objectives and Outline

The main objective of this work is to present a numerical model of the earth as an alternative to analytical models which is flexible enough to:

- *consider lateral, as well as radial, variations of a material within the earth,*
- *model dislocation sources such as rectangular fault inside the earth,*
- *include geodetically observed displacements as boundary conditions.*

This study applies finite element as a technique to show its flexibility to account for the above mentioned factors, detailed discussion of the technique is beyond the scope of this work.

Chapter 2 introduces briefly the focal mechanism of earthquakes. Body waves, different types of sources, geometry of a fault and their relevant terms are defined. Chapter 3 presents a number of different earth models, their specifications, and the relevant definitions, including the elements' sizes and shapes. Computations and results for these models are presented in chapter 4. Chapter 5 presents conclusions and suggestions for further studies. In Appendix A the elements of elasticity theory for a general elastic medium are described, starting from a simple material law, and continuing by generalizing for a continuum. The equation of motion of the medium is derived. Appendix B deals with body forces, in particular with the basic theorem of Betti, when is evaluated for the case of quiescent past and introduces the proper Green function. Equivalent body forces for discontinuities inside an elastic body are discussed. The appendix concludes with the representation of a seismic source by a distribution of force couples. Viscoelasticity theory is the subject of Appendix C, where the motions after the action of a deformation source are formulated. Thi is the proper tool to study the post-seismic displacement field.

Chapter 2

FOCAL MECHANISM

The main aim of this work is to deal with the displacement fields of some *dislocation sources*. By dislocation we mean discontinuous displacement, e.g. fault slippage. A dislocation source acts as a source of continuous displacement over the rest of the globe, and this is what we will compute. Actually, we will deal with a forward problem: given the dislocation value over the source area, we compute the displacement field.

This chapter presents the basic definitions which are required for later chapters.

2.1 BODY WAVES

Although at least one separate chapter could have been devoted to body waves, here we confine to the definitions and propagation patterns of P and S waves only.

The international Dictionary of Geophysics [RUNCORN, 1967] gives the following explanations:

> "Two types of elastic body waves may propagate in a homogeneous, isotropic, solid medium. Both waves involve shearing of the elastic medium, but one entails a volume change without any rotation of the material element whereas the other entails a rotation without any volume change. The former is designated P wave and the latter S wave. At large distances from the source the displacement of the elastic medium associated with the P wave is longitudinal whereas that associated with S wave is transverse. ...
>
> The designation P (for primae) and S (for secundae) were first used by seismologists to identify the first and second prominent arrivals on records of nearby earthquakes. By 1900 it was generally agreed that the events so identified could be associated with the two types of body waves predicted from the mathematical theory of elasticity by Poisson. A more general mathematical theory of these waves had been given by STOKES [1883] who showed that the faster wave would be dilatational and irrotational whereas the slower wave equivoluminal and rotational. In this manner the dilatational wave became known as the P wave and the equivoluminal as the S wave."

BÅTH [1979] writes:

> "P is longitudinal, i.e. particles hit by this wave oscillate back and forth around their equilibrium position in the same direction as the wave propagates. S is transverse, i.e. particle motion is confined to a plane perpendicular to the direction of propagation. For simplicity, we split the S wave motion into a horizontal (SH) and a vertical component (SV)."

One can write:

$$\mathrm{rot}\boldsymbol{U}_P = \mathbf{0} \quad , \tag{2.1}$$

and

$$\mathrm{div}\boldsymbol{U}_S = 0 \quad , \tag{2.2}$$

in which $\boldsymbol{U}_P$ and $\boldsymbol{U}_S$ are the displacement fields of the P and S waves respectively.

2.2 SOURCES

Different sources are responsible for earthquakes, and are classified in three main categories Båth [1979]:

- Collapse earthquakes, caused by the collapse of cavities in the earth's interior
- Volcanic earthquakes
- Tectonic earthquakes

Tectonic earthquakes are of the greatest significance to the earth, and are therefore discussed in more detail in the following, while the shocks of the first two categories were formerly overestimated in importance, although they are nearly always very small. A schematic picture of a tectonic mechanism is shown in figure (2.1). The heavy vertical full line is a fault, with horizontal lines the structure of the earth on both sides of the fault. This structure is continuous before any relative motion (figure2.1a). Slow motions in the earth cause deformation in this area as in figure (2.1b). This process continues until the generated stresses are larger than the strength of the material along the fault, and a rupture, i.e. a sudden motion, occurs (figure 2.1c). Figure (2.1d) shows the propagation pattern of S- and P-waves. In the upper left and lower right areas P-wave causes compression, this is shown by P^+ and positive oscillation values at the beginning of the curve z. In upper right and lower left areas P-wave causes dilatation, shown by P^- and negative values of z in the first oscillations. The diagonal lobes show displacement areas of P-waves. The horizontal lobes are the areas where S-wave propagates. In figure (2.1d) direction of the rupture on each side of the fault is shown by an arrow. As a result of this configuration, if we imagine a cube of unit side centered at the earthquake focus, it is deformed to a parallelepiped, the top view of which is depicted in figure (2.2).

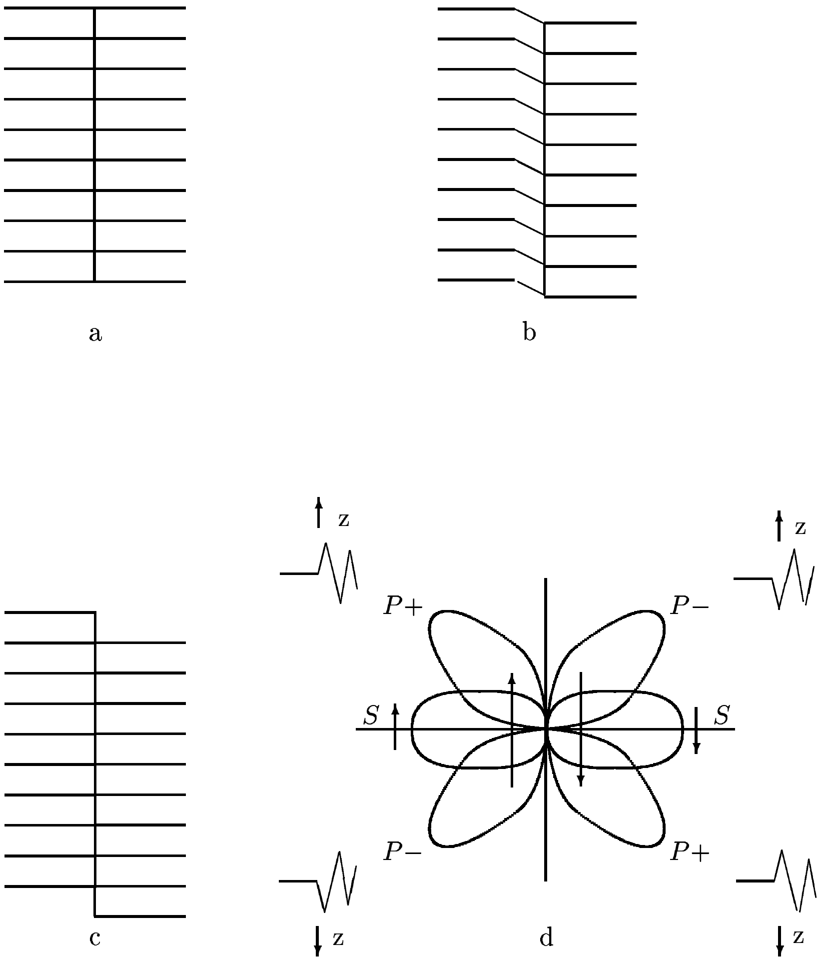

Figure 2.1: Simple model of a tectonic earthquake (a) before any motion, (b) after relative motion, (c) rupture, (d) P- and S-wave radiation patterns

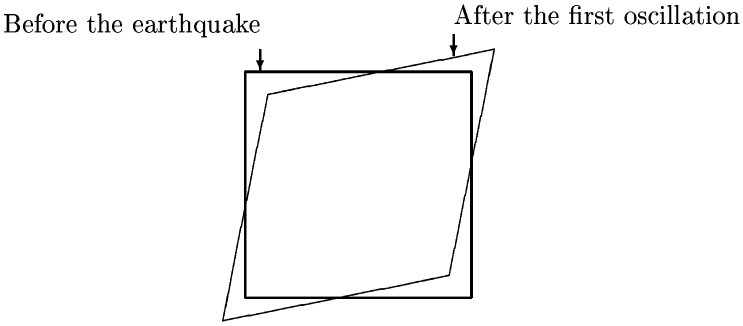

Figure 2.2: Deformation of a unit cube centered at the focus of an earthquake after the first oscillation, as seen from top

Worth mentioning is that the compressional and dilatational areas, as well as the sign of the z curve as shown in figure (2.1) are those of the first oscillation, and alternate in time. Whenever an earthquake occurs, the first wave arriving at the recording station is the direct P-wave. Experimental evidences show that this initial wave reaches at some stations as a compression, and at the others as a dilatation, and that these two types produce a systematic pattern which is related to the focal mechanism.

In the investigations of the focal mechanism we should look for the models which provide these systematic patterns. Different models have been proposed by investigators. Three basic models are noted in the following.

- Point Focus:
  Point focus is the simplest model. It consists of a force couple and produces the quadrantal distribution of compressions (+) and dilatations (-) (figure 2.3). The two perpendicular lines which separate the four quadrants are called *Nodal Lines*. The P-wave amplitude is zero on the nodal lines and is maximum on the bisector of the nodal lines, while S-wave amplitude is zero on one of the nodal lines (the fault) and maximum on its conjugate.

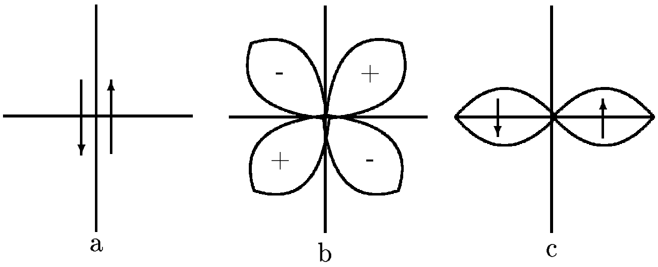

Figure 2.3: (a) Point focus with (b) P-wave, and (c) S-wave radiation patterns

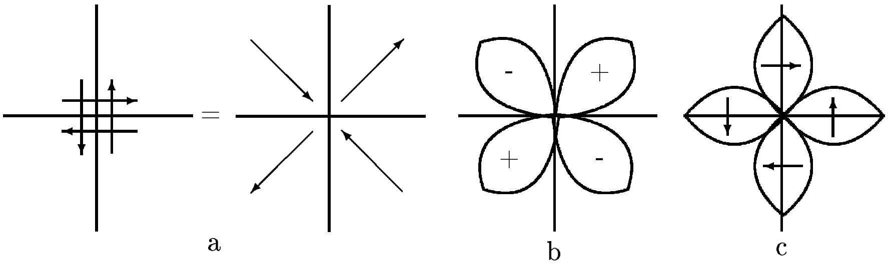

Figure 2.4: (a) Perpendicular pair of couples, its equivalent two pairs of opposite and equal forces at right angles, with (b) P-wave, and (c) S-wave radiation patterns

- Pair of Couples:
  This model consists of two perpendicular couples or equivalently two pairs of equal and opposite forces at right angles (figure 2.4). The P-wave radiation pattern is the same as that of a point force because a force couple normal to the previous one produces the same P-wave radiation pattern, while that of S-wave is different because the second perpendicular force couple generates an S-wave radiation pattern normal to the pattern of the first couple.

- More Sophisticated Models:
  Such models take into account the dimensions of the focus and do not consider them as point sources. Most of such models are based on dislocation theory. In this class there are again different theories which can be classified in two groups of kinematic and dynamic models. Kinematic models are those which regard an earthquake as a sudden release of accumulated strains along a fault, as proposed by KNOPOFF and GILBERT [1959] and KNOPOFF and GILBERT [1960]. In these models the trajectory of the displacement is given as a function of space and time. In dynamic models the forces acting on the particles are given, but the trajectory is unknown. In such models, e.g. VVDENSKAYA [1959], at the moment of failure the stresses accumulated on the surface of the fracture are relieved. Kinematic models deal with quantities as stress drop, average slip, and fracture area, while dynamic models with source volume and strain release.

Usually the earthquake mechanism is not as simple as a point source or a pair of couples, but can be analyzed mathematically as a combination of a number of such simple sources. The mathematical treatment is the subject of appendices A and B.

2.3 FAULT PLANE GEOMETRY

Obviously the radiation pattern of seismic waves varies with the direction of the focus (the fault *orientation*). The fault surface may have any orientation and consequently the displacement along the fault may happen in any direction. Therefore, in order to investigate the displacement field, we have to define a coordinate system and some useful directions or angles. We briefly review such definitions, and some of the interrelations.

- *Geographic system of coordinates* (figure 2.5)

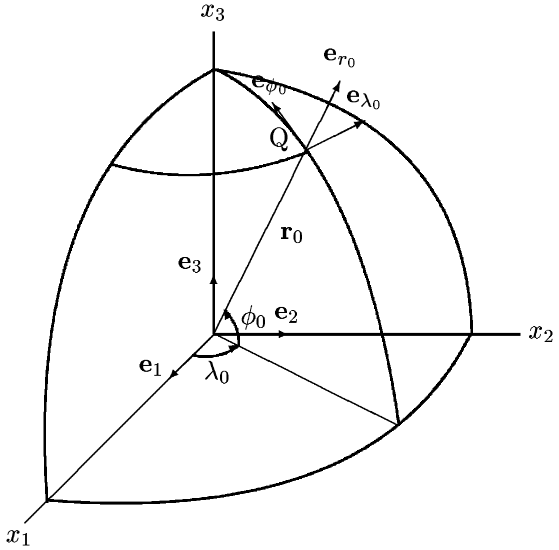

Figure 2.5: Geographic and epicentral systems of coordinates

  - Origin: mass center of the earth
  - e_1 axis: to the Greenwich meridian, in the equatorial plane
  - e_3 axis: through the North Pole
  - e_2 axis: so that the system is right handed

- *Epicentral system of coordinates* (figure 2.5)

  - Origin: epicenter
  - $\boldsymbol{e}_{r_0}$: upward
  - $\boldsymbol{e}_{\phi_0}$: northward
  - $\boldsymbol{e}_{\lambda_0}$: eastward

- The *rotation* between the geographic and the epicentral systems:

	$\boldsymbol{e}_1$	$\boldsymbol{e}_2$	$\boldsymbol{e}_3$
$\boldsymbol{e}_{\lambda_0}$	$-\sin\lambda_0$	$\cos\lambda_0$	0
$\boldsymbol{e}_{\phi_0}$	$-\sin\phi_0\cos\lambda_0$	$-\sin\phi_0\sin\lambda_0$	$\cos\phi_0$
$\boldsymbol{e}_{r_0}$	$\cos\phi_0\cos\lambda_0$	$\cos\phi_0\sin\lambda_0$	$\sin\phi_0$

- *Fault* (or *dislocation*) *plane*: the plane defined by the fracture, or simulated by its normal at the dislocation point

- *Auxiliary plane*: plane perpendicular to the fault plane and to the slippage. Either in double couple model of figure (2.4) or in single couple model of figure (2.3), fault plane and auxiliary plane are not distinguishable by the radiation pattern of P-waves, i.e. if these two planes are interchanged, the radiation pattern does not alter. Because of this ambiguity these two planes are called *conjugate planes.*

- *Strike direction* (or *strike of the fault*): the intersection line of the fault plane with the surface of the earth (figure 2.6)

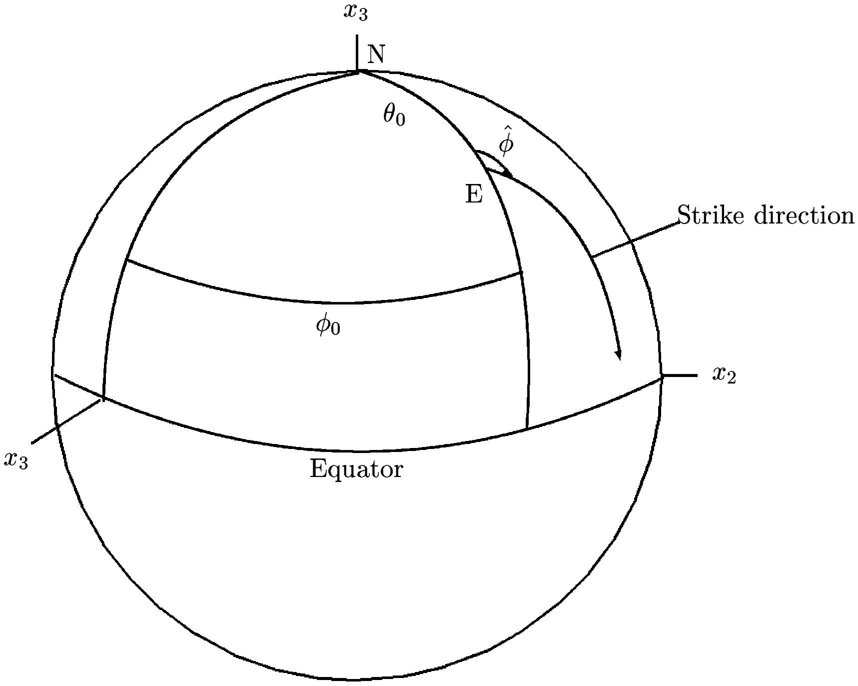

Figure 2.6: Strike direction and strike azimuth

- *Fault* (or *strike*) *azimuth*: the angle between the strike direction and north, measured clockwise from the north, $0 \leq \hat{\phi} < 2\pi$, (figure 2.6)

- *Foot wall*: the mass of the rock below an inclined fault (figure 2.7)

- *Hanging wall*: the mass of the rock above an inclined fault (figure 2.7)

- *Dip direction*: a line on the earth's surface perpendicular to the strike drawn in the direction in which the fault plane is dipping (figure 2.7)

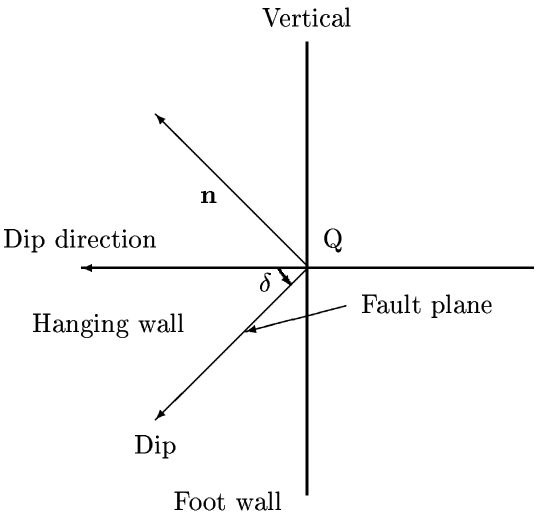

Figure 2.7: Dip direction, dip and dip angle δ

- *Dip of the fault*: a line in the fault plane perpendicular to the strike downward (figure 2.7)
- *Source system of coordinates*: the system obtained by rotating the epicentral system about $\mathbf{e}_{r_0}$ through an angle $\pi - \hat{\phi}$ (figures 2.8 and 2.9). This generates the
  - $\boldsymbol{e}_1^0$: in the strike direction
  - $\boldsymbol{e}_3^0$: upward
  - $\boldsymbol{e}_2^0$: so that the system is right handed

	$\boldsymbol{e}_{\phi_0}$	$\boldsymbol{e}_{\lambda_0}$	$\boldsymbol{e}_{r_0}$
$\boldsymbol{e}_1^0$	$-\cos\hat{\phi}$	$\sin\hat{\phi}$	0
$\boldsymbol{e}_2^0$	$-\sin\hat{\phi}$	$-\cos\hat{\phi}$	0
$\boldsymbol{e}_3^0$	0	0	1

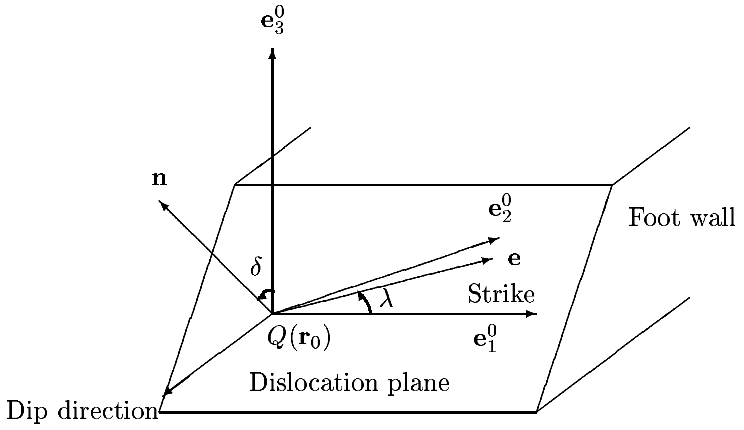

Figure 2.8: Slip angle, dip angle and the source system

- *Slip angle* (λ): the angle between the vector $\boldsymbol{e}$ (the unit vector in the slip direction) and the strike direction, measured counterclockwise from the strike direction so that $0 \leq \lambda < 2\pi$ (figure 2.8).
- *Dip angle* (δ): the acute angle between the normal to the fault plane ($\boldsymbol{n}$) and the vertical ($\boldsymbol{e}_3^0$), measured from the vertical direction so that $0 \leq \delta < \pi/2$ (figures 2.7 and 2.8)

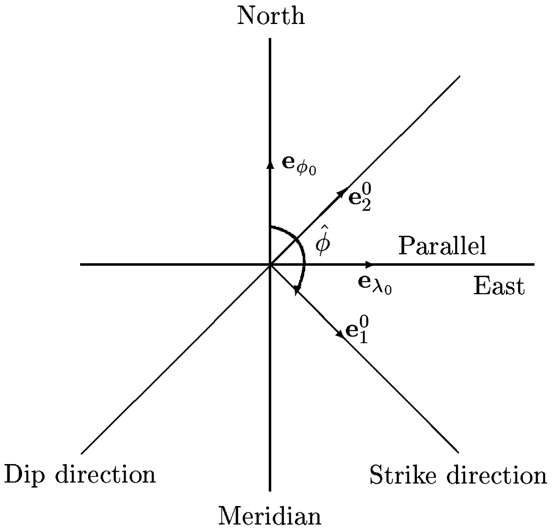

Figure 2.9: Side view with dip direction, strike direction, epicentral system and source system

- *Strike slip, lateral, transcurrent* or *wrench fault*: a fault for which $\lambda = 0$ or 2π, that means slippage in strike direction or opposite to it
- *Dip-slip fault*: a fault with an slip of $\lambda = \pi/2$ or $3\pi/2$, that means slippage in dip direction or opposite to it
- *Oblique slip fault*: a general fault which is a superposition of a strike-slip and a dip-slip fault, in other words the slip U_0 of a general fault can be decomposed to a slip of a strike-slip, $U_s = U_0 \cos\lambda$, and a slip of dip-slip fault, $U_d = U_0 \sin\lambda$
- *Dextral* or *right lateral fault*: a strike-slip fault in which to the eyes of an observer the opposite side of the fault moves rightward (figure 2.10a)
- *Sinistral* or *left lateral fault*: a strike slip fault in which to the eyes of an observer the opposite side of the fault moves leftward (figure 2.10b)

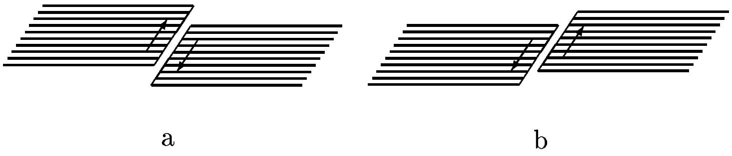

Figure 2.10: Two kinds of strike-slip faults: (a) right lateral and (b) left lateral

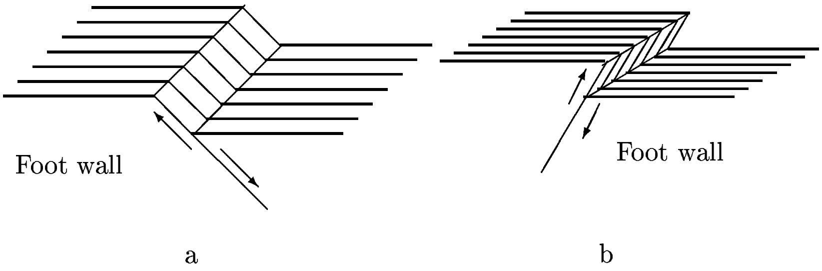

Figure 2.11: Two kinds of dip slip faults: (a) normal and (b) reverse

- *Normal fault*: an inclined fracture along which the hanging wall moves downward relative to the footwall (figure 2.11a)

- *Reverse fault*: an inclined fracture along which the hanging wall moves upward relative to the footwall (figure 2.11b)
- *Thrust fault*: a reverse fault with $\delta < 45°$
- *Overthrust fault*: a reverse fault with $\delta < 10^o$

Chapter 3

NUMERICAL EARTH MODEL

In the appendices we discuss the basic theory of the earth deformation analysis. The fundamental theories of elasticity (appendix A) and viscoelasticity (appendix B) were introduced as the proper theories to describe the response of the earth to various types of sources, e.g. dislocation sources. This chapter discusses the numerical definition of an earth model, which is then followed by a chapter on its solution.

3.1 EARTH MODEL DEFINITION

Our planet earth is highly heterogeneous. Its material varies from point to point so non-homogeneously that the variations can't be described by mathematical formulae. Moreover our knowledge of its material and the variations of density, elastic parameters, viscosity and temperature inside the earth is very limited. By earth modeling we understand specification of a model body which resembles the earth. A good model can be used as the only choice of studying the earth deformations when the internal structure of the earth is required. By earth model specification we mean specification of geometry and physics of the model earth. Geometry of the model is specified by its shape and size, while physics of the model is specified by its material content. Material specification in turn comprises assignment of properties and behavior. The parameters to be specified as the material properties in our applications, are mass density, elastic constants and viscosity for viscoelastic models. Material behavior specification determines whether the model, or each of its sub-domains, is elastic or viscoelastic, linear or nonlinear, and in case of viscoelastic, which model of viscoelasticity, Maxwell, Kelvin or more complicated (Appendix C).

In numerical modeling, there are more parameters to be assigned, i.e. size and shape of the elements. Size and even shape of the elements may also be a function of position, according to the area of interest, or when the source is so that in order to consider it more accurately, a finer network of nodes and elements within a specified area is the best and most economic way of modeling it with the required accuracy, or due to the local variations of the material properties.

Many analytical models have been specified and used, the models in which the material variations are specified as analytical functions of positions. PREM [Dziewonski and Anderson 1981] is the most widely accepted elastic spherical model which defines density, $P-$ and $S-$wave velocities, quality factors, seismic parameters, bulk modulus, shear modulus, Poisson's ratio, pressure, variations of bulk modulus with pressure and gravity as a function of radial distance or depth in 94 layers. SABADINI and VERMEERSEN, [1997] showed that in modeling glacial-isostatic adjustment, a ten layer model is sufficient to reflect the effective material variations of the model, and inclusion of more layers brings no further achievement about. MARTINEC and WOLF [1999] took the first step towards a laterally heterogeneous model by first designing a test model consisting of eccentrically nested spheres.

3.2 SPECIFICATION OF A NUMERICAL EARTH MODEL

As stated in §3.1, a number of parameters are to be specified to make a numerical model, in the following we introduce them step by step.

3.2.1 Elements' Shapes

The software ABAQUS to be used for finite element analysis in this work is able to handle a number of geometrically different elements [Hibbit, Karlsson and Sorensen, Inc. 1995]. We pick out the topologically simplest figure, a tetrahedron. Tetrahedron has the property that if each side of an equilateral tetrahedron is subdivided into two, eight tetrahedra are obtained. Four of them are again equilateral, and each of the other four figures has two equilateral triangles and two right angle isosceles triangles. The important property is that if the latter types of the subdivided tetrahedra are subdivided again in the same way, the set of the eight included tetrahedra contains four tetrahedra similar to the subdivided one, and four equilateral tetrahedra. This means that if a large tetrahedron, circumferencing a sphere, is subdivided further, the generated smaller tetrahedra approximate the sphere better, while the geometry of the tetrahedra does not deteriorate. What remains problematic is the area close to the sphere surface where the tetrahedra's sides intersect the surface. This problem is overcome by projecting the outer and inner nodes onto the sphere surface so that the subdivided tetrahedra exactly fill the spherical volume. Of course this deteriorates the geometry of the surface tetrahedra a little, but the degree of deterioration depends on the projection scheme. The mesh generator tool of the software MSC/PATRAN performs this job in a rather efficient way.

If the model is taken radially heterogeneous, the projection scheme is repeated on the boundaries of the inner spheres, while a finer grid of elements is required in order to prevent a geometry deterioration.

The next important point is that the elements could be either linear or quadratic. A Linear element (figure 3.1) is defined by its corner nodes only, the edges are lines, and a linear approximating function is used inside it, while a quadratic element includes midpoints in addition to its corners. The edges are quadratic lines, and the approximating function is quadratic (figure 3.2). Linear and quadratic tetrahedra are formed by 4 and 10 nodes respectively.

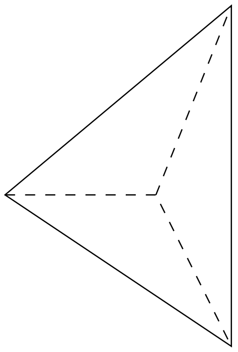

Figure 3.1: Linear tetrahedron

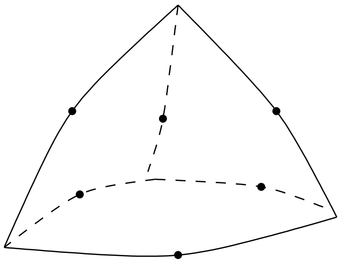

Figure 3.2: Quadratic tetrahedron, the midpoints are marked.

It is advisable to use linear elements only to fill the gaps of special areas, otherwise in order to obtain a reasonable accuracy, one needs too many elements.

In case of quadratic bodies, e.g. a sphere, there is another motivation for quadratic elements. They exactly fill the body. Edges of surface linear tetrahedra are only the sphere chords, while those of a quadratic tetrahedron lie on the spherical surface (figure 3.3). The homogeneous sphere of interest is subdivided into 1849 quadratic tetrahedra with an average side length of 2457 km. There are 2862 nodes for this decomposition. An internal and a surface tetrahedron are presented in figures (3.3 and 3.4), respectively. The elements are given in table 3.1. Node specification, including the node numbers and Cartesian coordinates is presented in table 3.2.

Although tetrahedron is used in this work as the main element shape, in some of the models it is not an efficient shape for the whole spherical body, in particular in multi layer models. A good example is a four layer model which consists of a spherical core, lower mantle, upper mantle and lithosphere, where the thicknesses of the two top layers, upper mantle and lithosphere, are relatively small in comparison to the

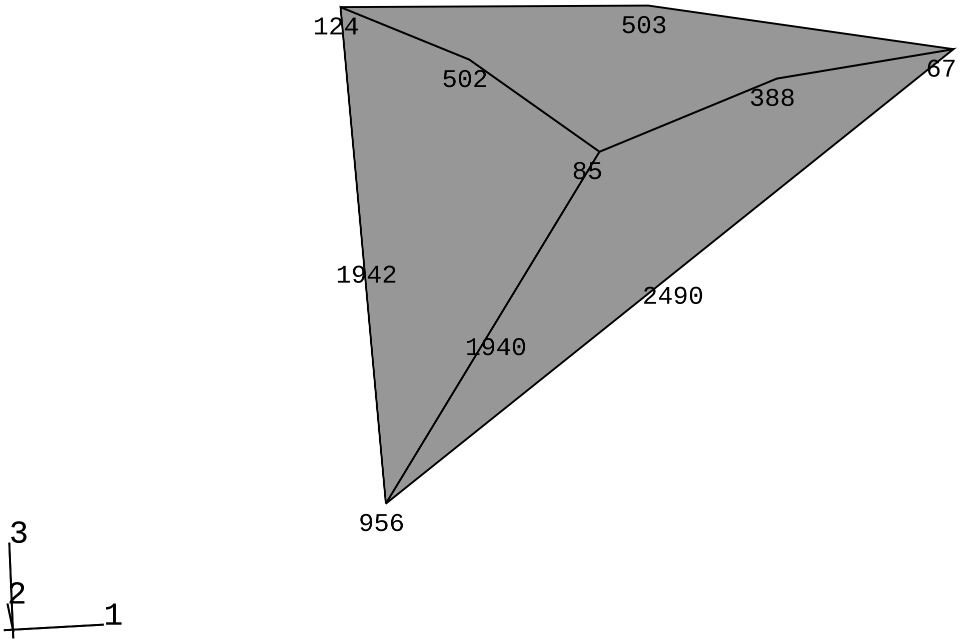

Figure 3.3: A surface element, the upper surface is a spherical triangle which lies on the model surface

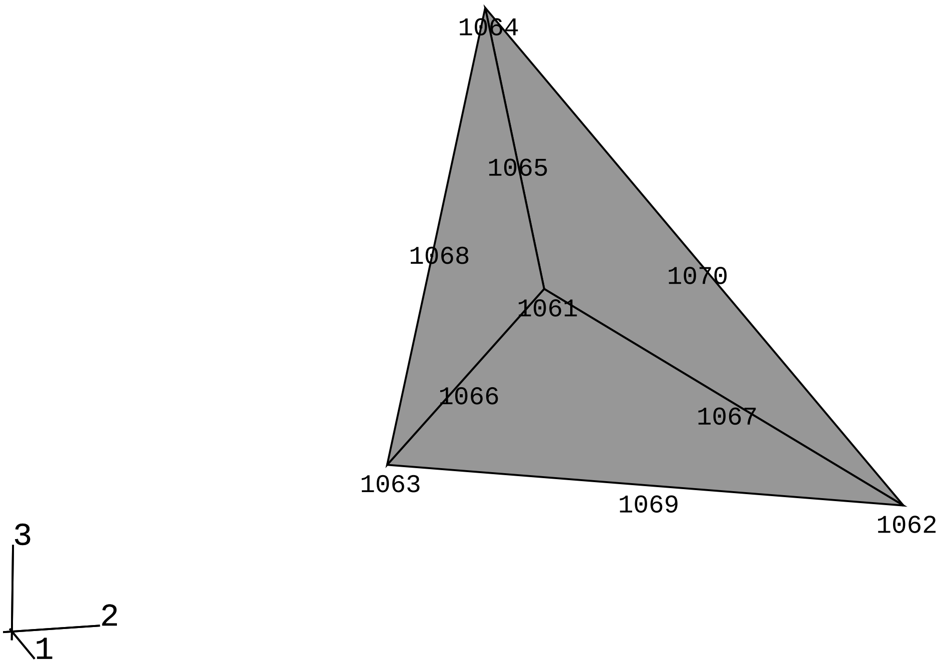

Figure 3.4: An internal element

365	1064	1063	1062	1061	1068	1069	1070	1065	1066	1067
1184	956	85	67	124	1940	388	2490	1942	502	503

Table 3.1: Element definition for the elements of figures (3.4 and 3.3) respectively. The first column shows the element number, columns 2 to 11 are the node numbers.

radius of the core and the thickness of lower mantle. If all the layers are to be descretized by tetrahedra, in the thinner layers, e.g. a 50 km thick lithosphere, one needs small elements in order to keep a good geometry of the elements, while in the lower layers this is not necessary. On the other hand, the nodes of the successive layers must be identical on the border. This means that for such layers too many small elements must be specified. To have a reasonable accuracy, 10^5 elements may be required, which increases the size of the problem.

n	x	y	z
67	1602891	593679	6137420
85	430074	-822451	6303035
124	-270010	834108	6310388
388	1020931	-104767	6287795
502	80153	5308	6370493
503	673843	720183	6294197
956	-203956	635086	4763783
1061	636615	-4495782	1450578
1062	-257575	-3129338	387696
1063	-387084	-4712731	584022
1064	-897696	-4290795	1849004
1065	-130540	-4393289	1649791
1066	124766	-4604257	1017300
1067	189520	-3812560	919137
1068	-642390	-4501763	1216513
1069	-322329	-3921035	485859
1070	-577635	-3710067	1118350
1940	113059	-93682	5533409
1942	-236983	734597	5537085
2490	699468	614383	5450601

Table 3.2: Node definition for the elements of the figures (3.3 and 3.4)

One method to overcome this problem is to model different areas of the model by different figures. In case of four layer sphere with a thin lithosphere and a relatively thin upper mantle, the best solution is to fill the lower mantle by tetrahedra, and the two thin layers by pentahedra. Each pentahedron of the upper mantle is made based on the triangular base of a tetrahedron in the lower mantle, and each pentrahedron of the lithosphere stands on the upper triangular base of a pentahedron in the upper mantle.

The next point is that since we are going to design different models with different thicknesses of the lithosphere, we must design a 5 layer model, with sandwich layer, that can be associated with the upper mantle or the lithosphere. This layer is modeled by pentahedra. A vertical cross section of the model is presented in figure (3.5). The darker part of the figure shows the surface of the fault.

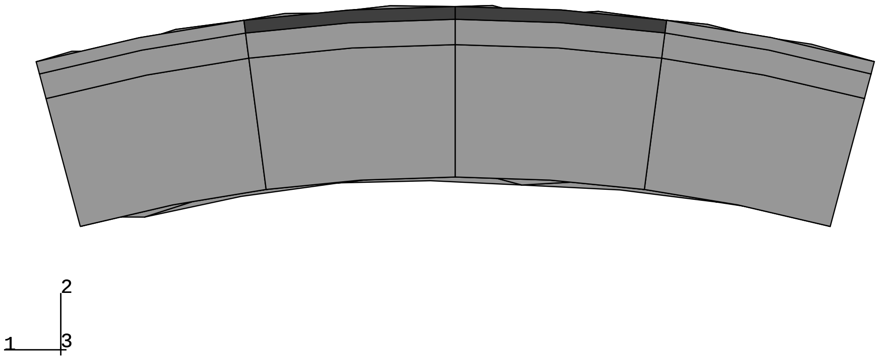

Figure 3.5: Cross section of the upper layers, descretized by pentahedra, the lower and upper levels show upper mantle and lithosphere, respectively, the intermediate level is in one model regarded as part of the upper mantle, and in another model as lithosphere. This helps to illuminate the role of lithosphere thickness in the model behaviour. The darker area is the fault surface.

This set up ensures the flexibility of changing the thickness of lithosphere, while keeping the geometry of the model constant, so that the responses are affected by the change of rheology only, and not by different model geometries.

3.2.2 Model Geometry

Next, the model size and shape are defined. The model is taken as a sphere, with no discontinuity surface inside. It is important to choose a spherical boundary, because in case of internal discontinuities the spherical boundary is extended so that it includes the discontinuity surface (figure B.1). The size of the sphere is described by its radius, which is taken as the average radius of the earth, 6371 km.

3.2.3 Physical Properties of the Model

When choosing the physical properties, some specifications must be specified.

Compressibility: Shows to which extent the model is undertaking volume changes. In this study, we confine ourselves to incompressible models, i.e. there is no volume change assumed. This implies zero dilatation everywhere in the model:

$$\epsilon_{ii} = 0 \ . \tag{3.1}$$

Incompressible response of material is not trivial for a numerical analysis, since a purely hydrostatic pressure does not change the displacement field. The nearly incompressible case, or Poisson's ratio of greater than 0.49 exhibits a singular behavior. λ in eq. (A.65) approaches infinity by $\nu = 0.5$. This cause the numerical solution to be too sensitive to be used in practice. This singularity is removed by treating the pressure stress as an independently interpolated basic solution variable, in the so called 'hybrid elements'. A detailed explanation is presented in HIBBIT et. al (1995).

Isotropy: specifies whether there are directional changes of the material properties at each point, an isotrope material is one without directional dependencies of the properties.

Homogeneity: Whether a parameter is constant over the whole model, or they change with position, e.g. homogeneity in elastic parameters implies (no positional dependency of the parameters) that:

$$\frac{\partial \lambda}{\partial x_i} = \frac{\partial \mu}{\partial x_i} = 0 \ , \tag{3.2}$$

while in a non-homogeneous model at least one of the above derivatives doesn't vanish.

Rheology: Determines in which way the model behaves, elastic or viscoelastic, linear or non-linear, and in case of a viscoelastic model, whether it behaves like a Maxwell fluid, Kelvin solid or a more complicated body. In the following we assume linear models and in particular Maxwell fluid.

Gravitation: Self gravitation of the model can play an important role. When it is present, its prestress field is taken into account according to the theoretical discussion of §A.2.5. We do not consider the rotation of the earth in this work. A spherically symmetric, i.e. laterally homogeneous, isotropic sphere generates a hydrostatic gravitational field, i.e. it causes no shear component. In the computations (chapter 4) the effect of the gravitational pre-stress field is presented by comparing the responses of two models with common geometrical and physical properties, but with and without gravitational pre-stress field.

A number of different models are formed, they are explained in the following.

3.2.3.1 Incompressible, Homogeneous, Isotropic, Linear Elastic Sphere

The simplest spherical model is taken into account first, in order to make a comparison of the results with a known solution for the displacement field of a simple surface distribution of loads. This is required to check the ability of the finite element technique. The required parameters have the following values:

- The mass of the earth is chosen so that it generates a gravity modulus of $g = 10$ m s^{-2} on the surface. With a radius of $R = 6371$ km, a universal gravitational constant of $G = 6.672.10^{-11}$ m^{3}kg^{-1}s^2, the total mass of the model is computed from:

  $$g = \frac{GM}{R^2} \tag{3.3}$$

  as $M = 6.083579287 \times 10^{24}$ kg. If distributed homogeneously over the sphere, the mass density is: $\rho = 5616$ kgm^{-3}.

- Average elastic constants are used in the model. Incompressibility implies that $\lambda \to \infty$. The rigidity is taken as $\mu = 6 \times 10^{10}$ Pa. Young's modulus (E) and Poisson's ratio (ν), from Eringen [1980]:

$$\lambda = \frac{E\nu}{(1+\nu)(1-2\nu)} \tag{3.4}$$

and

$$\mu = \frac{E}{2(1+\nu)} \ , \tag{3.5}$$

which imply that

$$E = \mu \frac{3\lambda + 2\mu}{\lambda + \mu} \tag{3.6}$$

and

$$\nu = \frac{\lambda}{2(\lambda + \mu)} \ . \tag{3.7}$$

This yields $E = 1.8 \times 10^{11}$ Pa and $\nu = 0.5$.

- Linear elasticity is assumed.

3.2.3.2 Incompressible, Pre-Stressed, Homogeneous, Isotropic, Elastic Sphere

The previous model applies, except that the gravitational pre-stress filed of masses is taken into account. The pre-stresses are formulated as shown in §A.2.5. What remains is to compute the gravitational stress as a function of radius.

The equilibrium state of a self gravitating sphere is given by matching its body force with the pressure gradient [Aki and Richards 1980]:

$$-\rho g(r)\boldsymbol{r} = \nabla P(r) \ , \tag{3.8}$$

where ρ is the constant density, e.g., $g(r)$ the positive valued modulus of gravity, $\boldsymbol{r}$ the unit radial vector, ∇ the gradient operator, and $P(r)$ is the pressure. $P(r)$ is in fact the pre-stress field we seek. Because of the spherical symmetry, the gradient is equal to the radial derivative:

$$\nabla P = \frac{\partial P}{\partial r} = -\rho g = -\rho\left(\frac{4}{3}\pi G \rho r\right) = -\frac{4}{3}\pi G \rho^2 r \ . \tag{3.9}$$

Integration yields:

$$P = -\frac{2}{3}\pi G \rho^2 r^2 + C \ , \tag{3.10}$$

where C is the integration constant. If we assume no pressure on the model surface:

$$P(R) = -\frac{2}{3}\pi G \rho^2 R^2 + C = 0 \ . \tag{3.11}$$

Therefore:

$$C = \frac{2}{3}\pi G \rho^2 R^2 \ , \tag{3.12}$$

which means with eq. (3.10):

$$P(r) = \frac{2}{3}\pi G \rho^2 (R^2 - r^2) \ . \tag{3.13}$$

For a hydrostatic equilibrium state, the prestress tensor is:

$$\boldsymbol{\sigma}_0 = -P\boldsymbol{I} \ . \tag{3.14}$$

3.2.3.3 Incompressible, Non-gravitational, Homogeneous, Isotropic, Viscoelastic Sphere

The model is assumed of the same geometry, density and elastic parameters as in §3.2.3.1, and the average viscosity is $\nu = 10^{20}$ Pa s .

3.2.3.4 Incompressible, Pre-Stressed, Homogeneous, Isotropic, Viscoelastic Sphere

As for the previous model, except that the gravitational effect of mass is taken into account as pre-stress. The pre-stresses are treated as discussed in §A.2.5, similar to the previous model.

3.3 NON-HOMOGENEOUS MODELS

It is not intended to end this work with homogeneous models. One of the main purposes is to investigate the possibility of applying a numerical technique to more complicated models, especially in response to dislocation sources. We therefore design a number of non-homogeneous models in addition to the simple homogeneous ones.

In order to investigate the effect of different parameters, e.g. rigidity and viscosity, of different earth layers, the following models are analyzed. In all modes the total mass is constant so that it generates a gravitational acceleration of 10 m s^{-2} on the surface. All models except the last have five layers with respect to rigidity and differ in viscosity profile. The last model is designed to study the effect of rigidity.

3.3.1 Model A: Core, Lower Mantle, Upper Mantle

This model includes a core, a perfect fluid, a lower mantle, a Maxwellian viscoelastic solid, and an upper mantle, another Maxwellian viscoelastic solid with a lower rigidity than that of lower mantle.

Mass, rigidity and viscosity values are given in table 3.3, they are adopted from PREM [Dziewonski and Anderson, 1981] and Sabadini and Vermeersen [1997].

Layer	R(km)	μ(N m^{-2})	ρ(kg m^{-3})	ν(Pa s)
1	0 – 3480	–	10932	–
2	3480 – 5700	2.17×10^{11}	4878	2.4×10^{22}
3	5700 – 6221	1.10×10^{11}	4003	1.6×10^{21}
4	6221 – 6321	6.7×10^{10}	4003	1.6×10^{21}
5	6321 – 6371	4.6×10^{10}	4003	1.6×10^{21}

Table 3.3: Material properties of a multi-layered model without lithosphere (Model A)

Although a model without lithosphere is far from the real earth, it is useful for investigating the role of the lithosphere in the earth behaviour.

3.3.2 Model B: Core, Lower Mantle, Upper Mantle, 50 km Lithosphere

A thin lithosphere is added on top of the upper mantle. The practical difference with the previous model is that the viscosity of the upper 50 km is set to infinity, while the rigidity and density profiles are kept unchanged. In this way the effect of an elastic layer in the earth behaviour is revealed. The relatively thin lithosphere resembles an oceanic plate. Table 3.4 shows the model properties.

Layer	R(km)	μ(N m^{-2})	ρ(kg m^{-3})	ν(Pa s)
1	0 – 3480	–	10932	0
2	3480 – 5700	2.17×10^{11}	4878	2.4×10^{22}
3	5700 – 6221	1.10×10^{11}	4003	1.6×10^{21}
4	6221 – 6321	6.7×10^{10}	4003	1.6×10^{21}
5	6321 – 6371	4.6×10^{10}	4003	∞

Table 3.4: Material properties of a multi-layered model with a 50 km thick lithosphere (Model B)

3.3.3 Model C: Core, Lower Mantle, Upper Mantle, 150 km Lithosphere

The thickness of the lithosphere is increased to 150 km. The viscosity of this layer is set to infinity, while the rigidity profile remains unchanged again (table 3.6).

The relatively thick lithosphere may be thought of as a continental plate. Adding the results of this model to models A and B gives a more complete picture of the effect of the lithosphere and its thickness. On the other hand the comparison of this model with model B can give an impression of the different behaviour of oceanic and continental lithosphere.

Layer	R(km)	μ(N m^{-2})	ρ(Kg m^{-3})	ν(Pa s)
1	0 – 3480	–	10932	0
2	3480 – 5700	2.17×10^{11}	4878	2.4×10^{22}
3	5700 – 6221	1.10×10^{11}	4003	1.6×10^{21}
4	6221 – 6321	6.7×10^{10}	4003	∞
5	6321 – 6371	4.6×10^{10}	4003	∞

Table 3.5: Material properties of a multi-layered model with a 150 km thick lithosphere (Model C)

3.3.4 Model D: Core, Lower Mantle, Upper Mantle, Laterally Heterogeneous Lithosphere

The main argument of applying a numerical technique to the analysis of earth deformations, for example in response to a dislocation source, is its flexibility to model different material behaviours in different parts of the model as opposed to the limitations of analytical techniques. The final purpose is actually to go beyond these limitations. An important limitation of analytical techniques is the assumption of lateral homogeneity, an assumption which may not be true around faults. Taking into account that many of the important earthquakes happen on the borders of oceanic and continental plates, one may appreciate the importance of the factor which is neglected in analytical models. The model properties are presented in table 3.6. In this model the continental plate covers an area of about 4500×9000 km^2 (figure 3.6), and the fault is in the middle of its lower border. The rest of the globe is covered by the oceanic plate, i.e. 50 km thick lithosphere. In the computation step, displacement curves are plotted for points on the margin, in the middle of, and out the the continental plate. They will be compared to the results of radially symmetric models.

Layer	R(km)	μ(N m^{-2})	ρ(kg m^{-3})	ν(Pa s)
1	0 – 3480	–	10932	0
2	3480 – 5700	2.17×10^{11}	4878	2.4×10^{22}
3	5700 – 6221	1.10×10^{11}	4003	1.6×10^{21}
4	6221 – 6321	6.7×10^{10}	4003	∞ or 1.6×10^{21}
5	6321 – 6371	4.6×10^{10}	4003	∞

Table 3.6: Material properties of a multi-layered model with a heterogeneous lithosphere (Model D), the viscosity of layer 4 is ∞ and 1.6×10^{21} Pa s in the continental and oceanic plates respectively

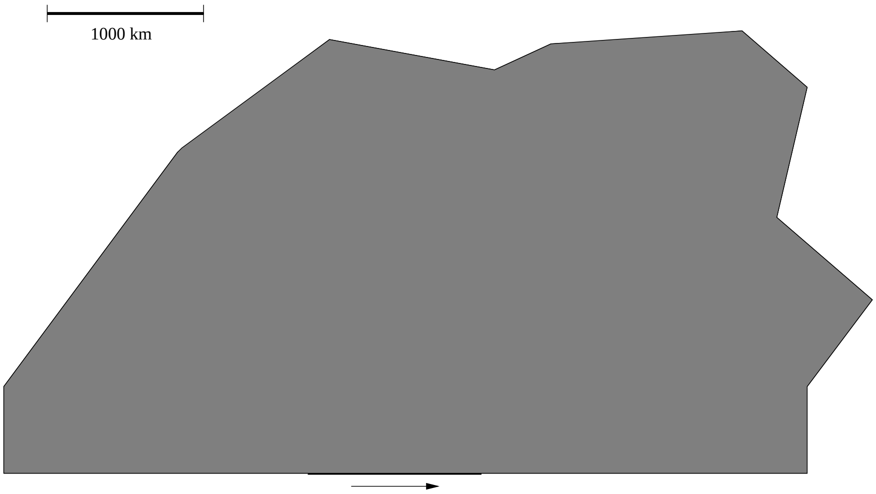

Figure 3.6: Continental plate in model D, fault is located in the middle of the lower border

3.3.5 Model E: Core, Lower Mantle, Upper Mantle, 150 km Lithosphere of Constant Rigidity

In this model the lithosphere is of 150 km thickness and constant rigidity. The only difference with model C is therefore that the rigidity of the upper 50 km is set equal to that of the lower 100 km. This is stated in table 3.7. The purpose of this model is to investigate the effect of rigidity, when compared to the results of model C.

Layer	R(km)	μ(N m^{-2})	ρ(kg m^{3})	ν(Pa s)
1	0 – 3480	–	10932	0
2	3480 – 5700	2.17×10^{11}	4878	2.4×10^{22}
3	5700 – 6221	1.10×10^{11}	4003	1.6×10^{21}
4	6221 – 6321	6.7×10^{10}	4003	∞
5	6321 – 6371	6.7×10^{10}	4003	∞

Table 3.7: Material properties of Model E

3.4 DEFORMATION SOURCE

Although the first aim of the this study is to apply the model for the analysis of the displacement discontinuity sources, e.g. discontinuous motion of the fault surfaces, and in particular post-seismic displacements, we first investigate the displacement field of a simplified surface load. This is because the analytical solution of this problem is well known, and is therefore a good bench mark to test the accuracy of the numerical solution.

3.4.1 Surface Load

We apply a simple surface load proportional to the second degree zonal spherical harmonic:

$$L(\theta) = L_m Y_2(R, \theta) \ , \tag{3.15}$$

where L_m is the maximum pressure amplitude, R the radius of the model earth, θ the colatitude measured from the north pole, and:

$$Y_2(R, \theta) = \frac{1}{2}(3\cos^2\theta - 1) \ . \tag{3.16}$$

As the load thickness, we take $H_L = 3$ km and thick assuming ice, a density of $\rho_L = 900$ kg m^{-3}:

$$L_m = \rho_L g H_L = 2.7 \times 10^7 \ \mathrm{Pa} \ . \tag{3.17}$$

where g is the surface modulus of gravity, $g = 10$ m s^{-2}. From the last three equations:

$$L(\theta) = 1.35 \times 10^7 (3\cos^2\theta - 1) \ \mathrm{Pa} \ . \tag{3.18}$$

3.4.2 Dislocation Sources

As the final aim of this work, dislocation sources are applied, a dipolar source of the type discussed in §B.5.1, a one dimensional strike-slip fault, and a two dimensional vertical strike-slip fault.

The dipole is assumed to be located on the surface of the earth, with center and forces on the $x-$axis. This is shown as $(1, 1)$ in figure (B.4). A pressure of 1×10^{19} Pa is applied on each side of the $(R, 0, 0)$ point.

The first dislocation source is assumed as a one dimensional displacement discontinuity on the earth's surface. The length and the prescribed amount of dislocation are introduced. The importance of a dipole is that, as discussed in appendix B, a displacement discontinuity, e.g. slip on the surface of a fault, can be analyzed as a distribution of dipolar sources on the fault surface.

The last and the most interesting source being dealt with in this work is a two dimensional dislocation source, a vertical right lateral strike-slip fault, i.e. a vertical plane on which discontinuous displacement may occur as a source of continuous displacement over the rest of the model. A vertical section of the model is depicted in figure (3.5).

The sources and the results are discussed in the next chapter.

Chapter 4

RESULTS

This chapter presents results of the numerical computations for the model earth deformations under the application of the force fields mentioned in chapter 3. Various models are investigated, all the models considered are incompressible and isotropic, what make the difference of the models are the rheology and the self gravitational pre-stress field. We consider both elastic and viscoelastic models, with and without pre-stress field, under surface loads, dipolar sources, one and two dimensional strike-slip faults. In one case, where the analytical solution is well known, the effect of the pre-stress field is discussed.

Some results presented in the following are location dependent, e.g. displacement curves at different points, figure (4.1) shows the position of the points with respect to the fault and the lithospheric plate for model D (chapter 3). Exact locations of the points are listed in table 4.1. The source is the planar fault of figure (3.5), with the corner nodes given in table (4.2).

Figure 4.1: Relative positions of the selected points with respect to the fault location of continental plate of model D (chapter 3), point 6 is on the north pole, while the fault is located in the equator.

Since one important question in numerical analysis is the numerical stability, first of all we try to investigate this important point. There are some signs of numerical instability in response to the dislocation source. Then we start the analysis of the earth behaviour under the surface load and dislocation source in turn. Surface load is applied only to the simple homogeneous models only, in order to compare the results with the given analytical solution. Dislocation sources, as the aim of this analysis, are discussed afterwards.

4.1 NUMERICAL STABILITY

In order to answer the question of numerical stability of the solution, we plot the displacement values for a longer time span. In studying the earth responses, a time span of $5,000$ years is used; for investigating the stability, we extend this to $60,000$ years in order to see if the model is unstable beyond the time span of interest in the deformation analysis. The figures (4.2-4.11) show parallel, perpendicular and vertical

n	x	y	z
1	553	6323	632
2	-553	6323	-555
3	1617	6039	-1226
4	1253	6138	1162
5	-1865	6003	-1033
6	0	0	6371
7	0	6345	278
8	537	6146	1589
9	-553	6323	555
10	-544	6219	1274
11	-1563	6176	0
12	-1557	6153	555
13	-1899	5985	1079
14	-528	6034	1976

Table 4.1: Exact locations of the analysis points in km.

n	x	y	z
200037	551	6297	0
200044	-551	4559	2000
400037	555	6347	0
400044	-551	6297	0

Table 4.2: Node numbers and position (in km) of the corners of the source fault (figure 3.5)

components of displacements at points 1 and 4 (figure 4.1). The quantities given in the legends of the following graphs are given in §4.3. The figures do not show any sign of numerical instability, the more refined finite element model depicted by thicker line (§4.3) show the relaxation of the model after the time period of $60,000$ years, particularly in horizontal components.

Relatively small values of the vertical components are due to the horizontal dislocation source.

Abbreviations used in the graph annotations are introduced in §4.3

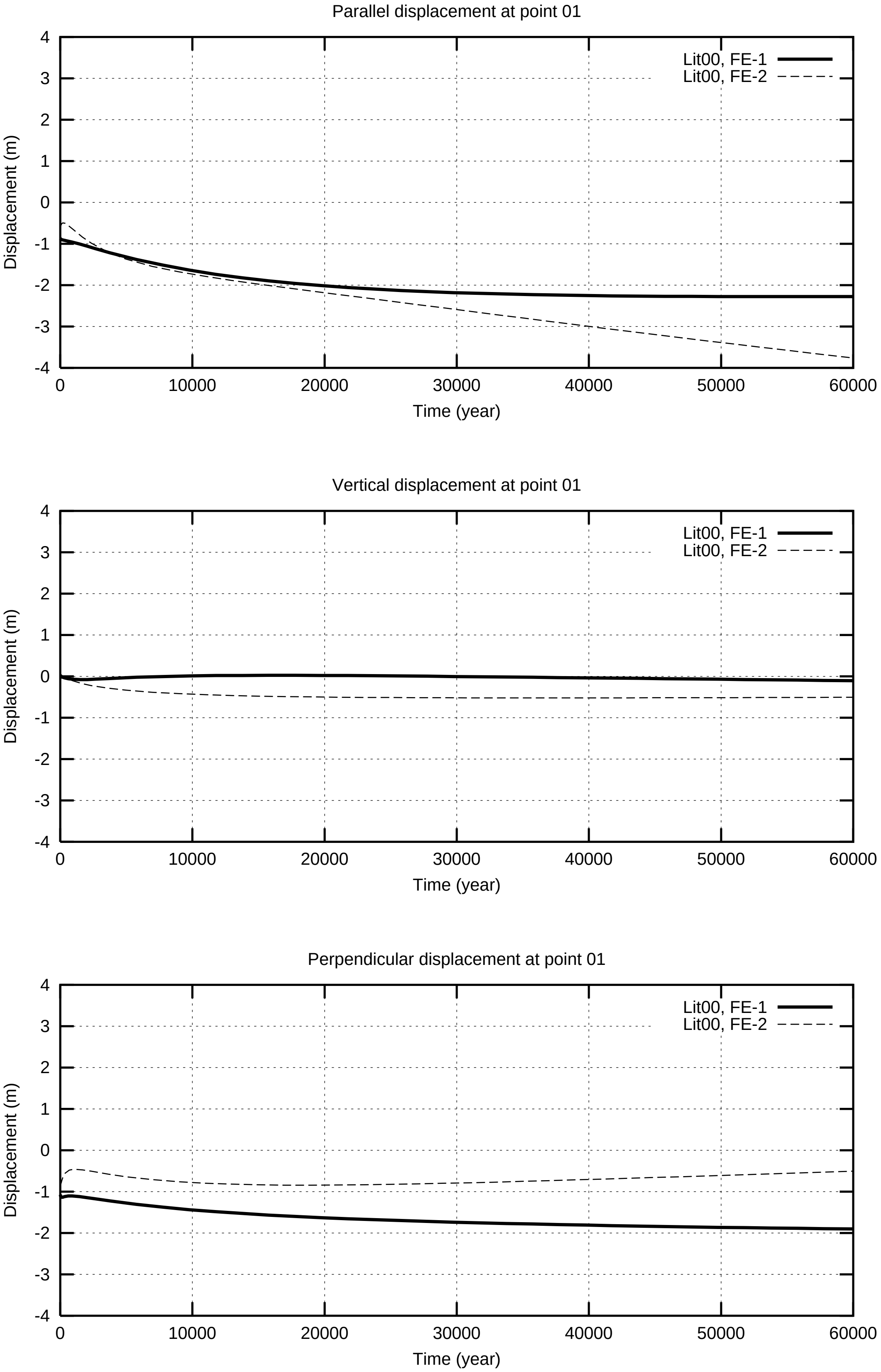

Figure 4.2: Parallel, perpendicular and vertical components of displacements at point 1 (figure 4.1) on the surface of model A

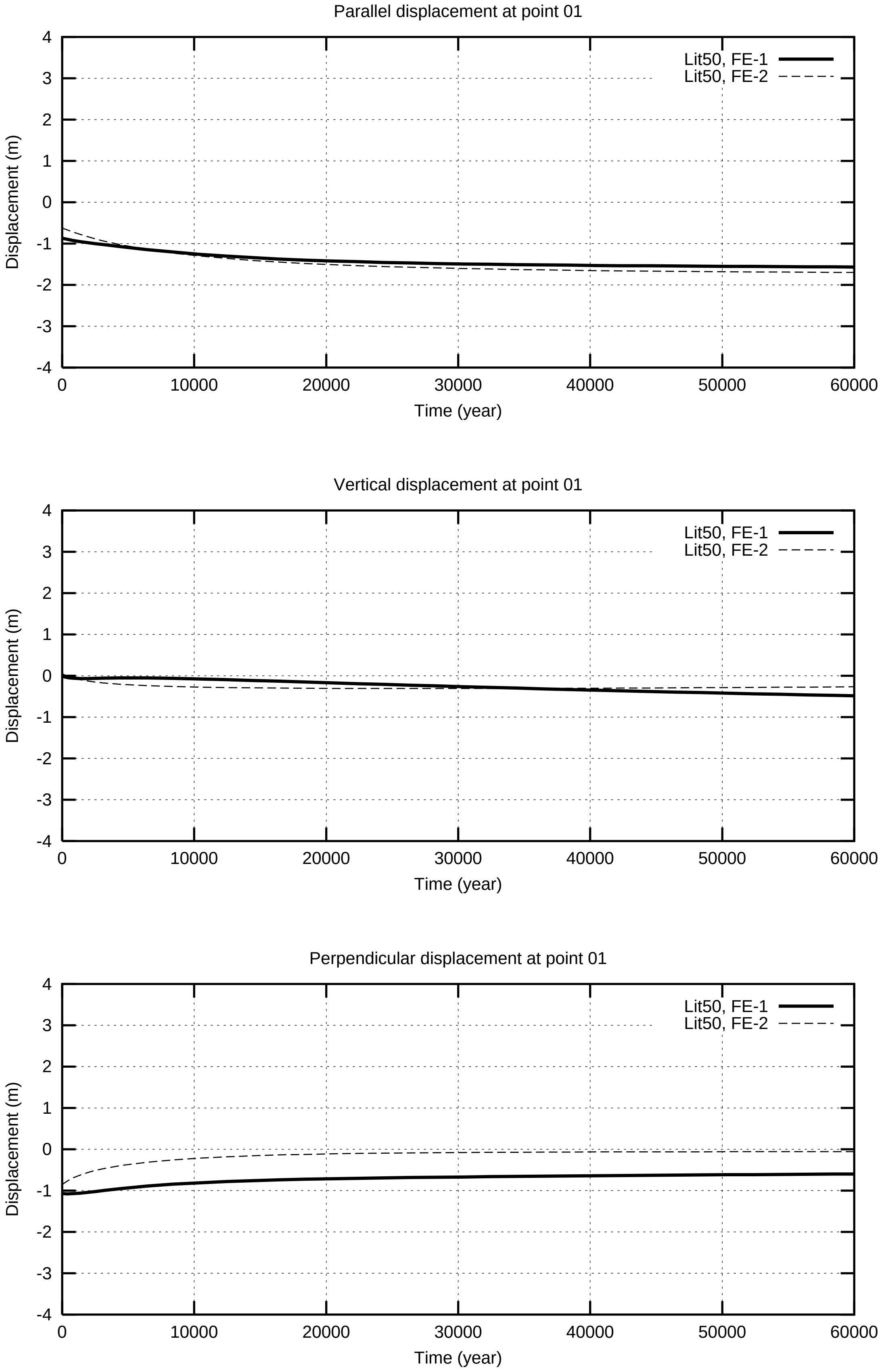

Figure 4.3: Parallel, perpendicular and vertical components of displacements at point 1 (figure 4.1) on the surface of model B

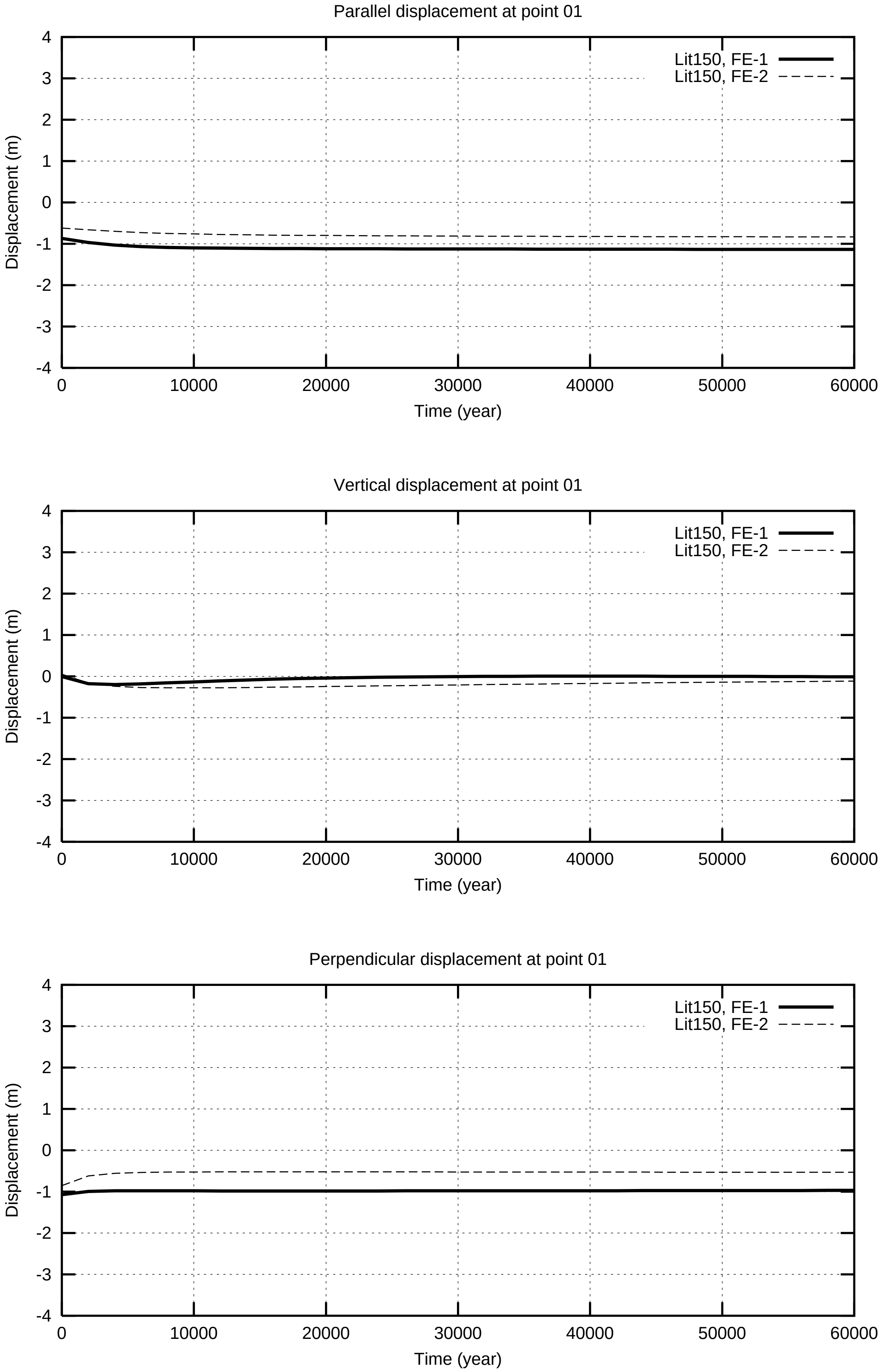

Figure 4.4: Parallel, perpendicular and vertical components of displacements at point 1 (figure 4.1) on the surface of model C

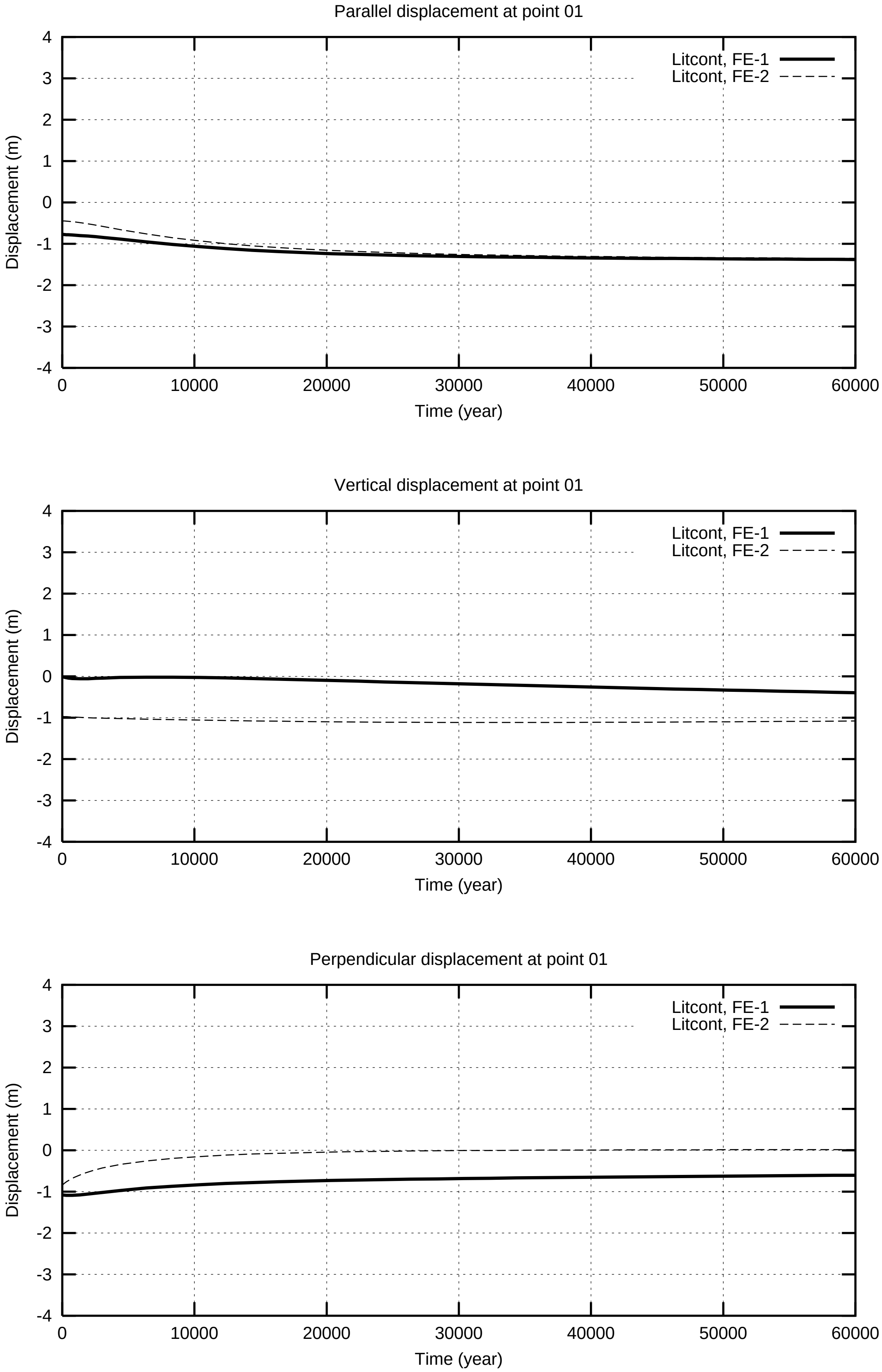

Figure 4.5: Parallel, perpendicular and vertical components of displacements at point 1 (figure 4.1) on the surface of model D

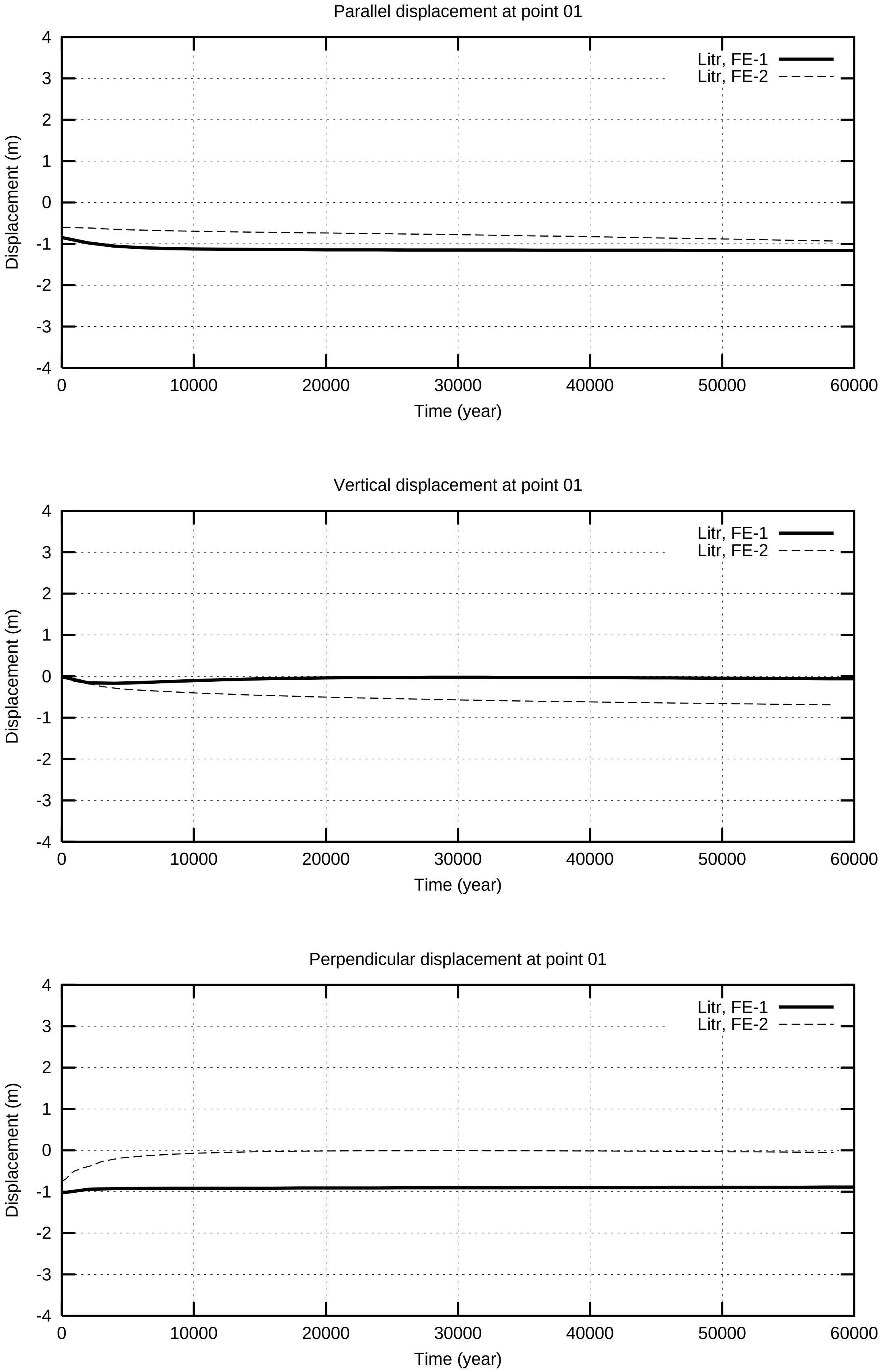

Figure 4.6: Parallel, perpendicular and vertical components of displacements at point 1 (figure 4.1) on the surface of model E

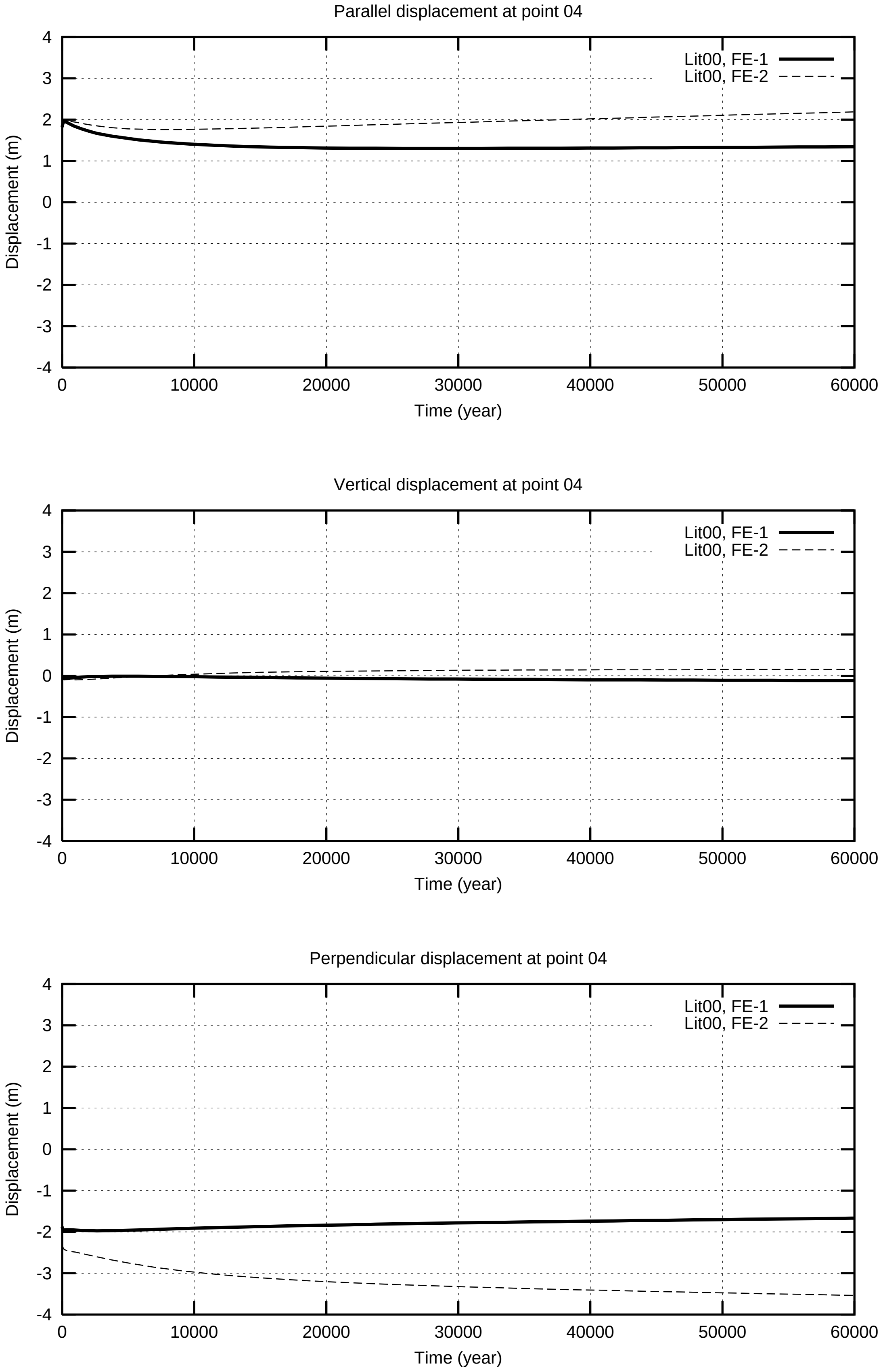

Figure 4.7: Parallel, perpendicular and vertical components of displacements at point 4 (figure 4.1) on the surface of model A

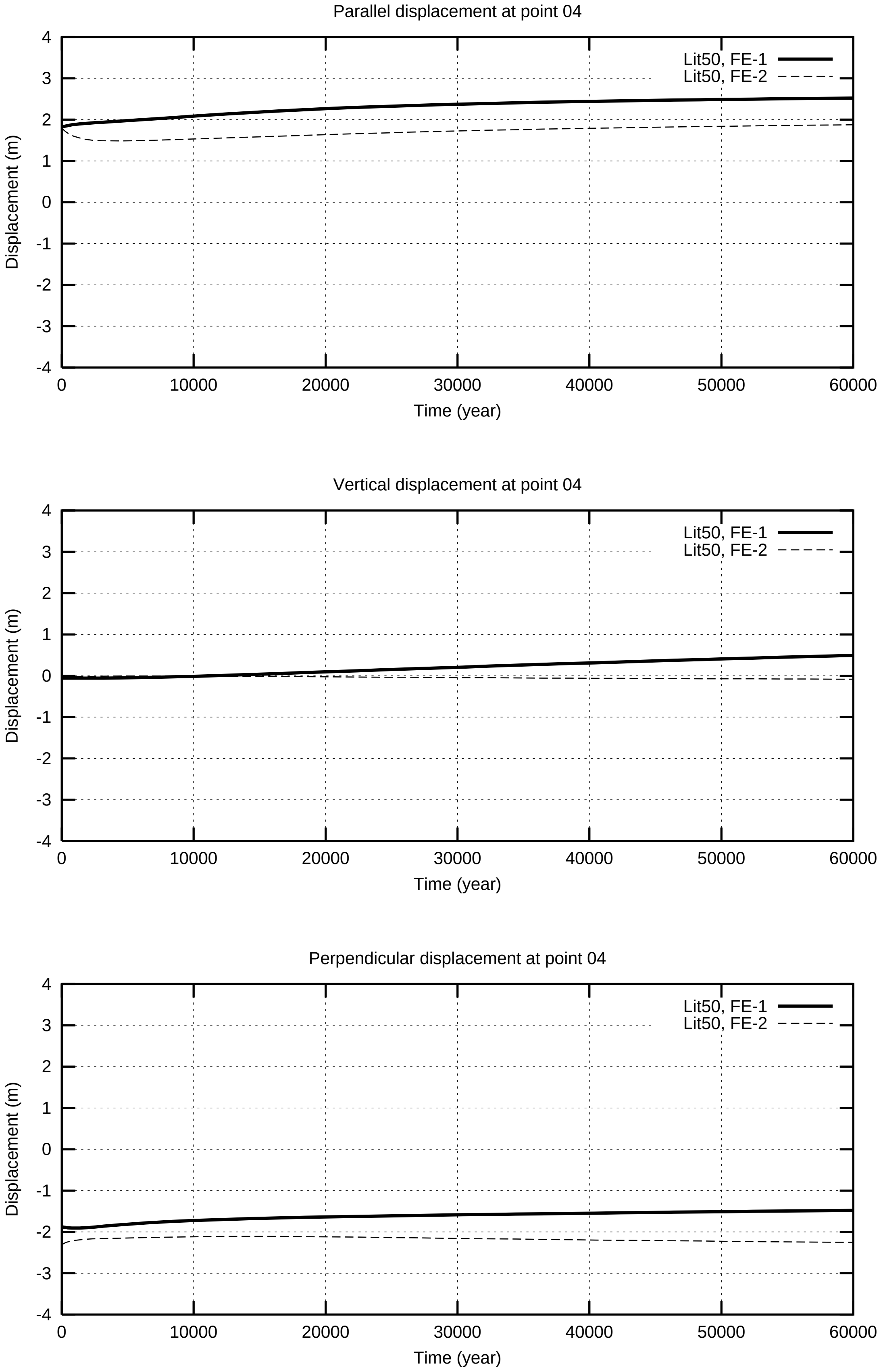

Figure 4.8: Parallel, perpendicular and vertical components of displacements at point 4 (figure 4.1) on the surface of model B

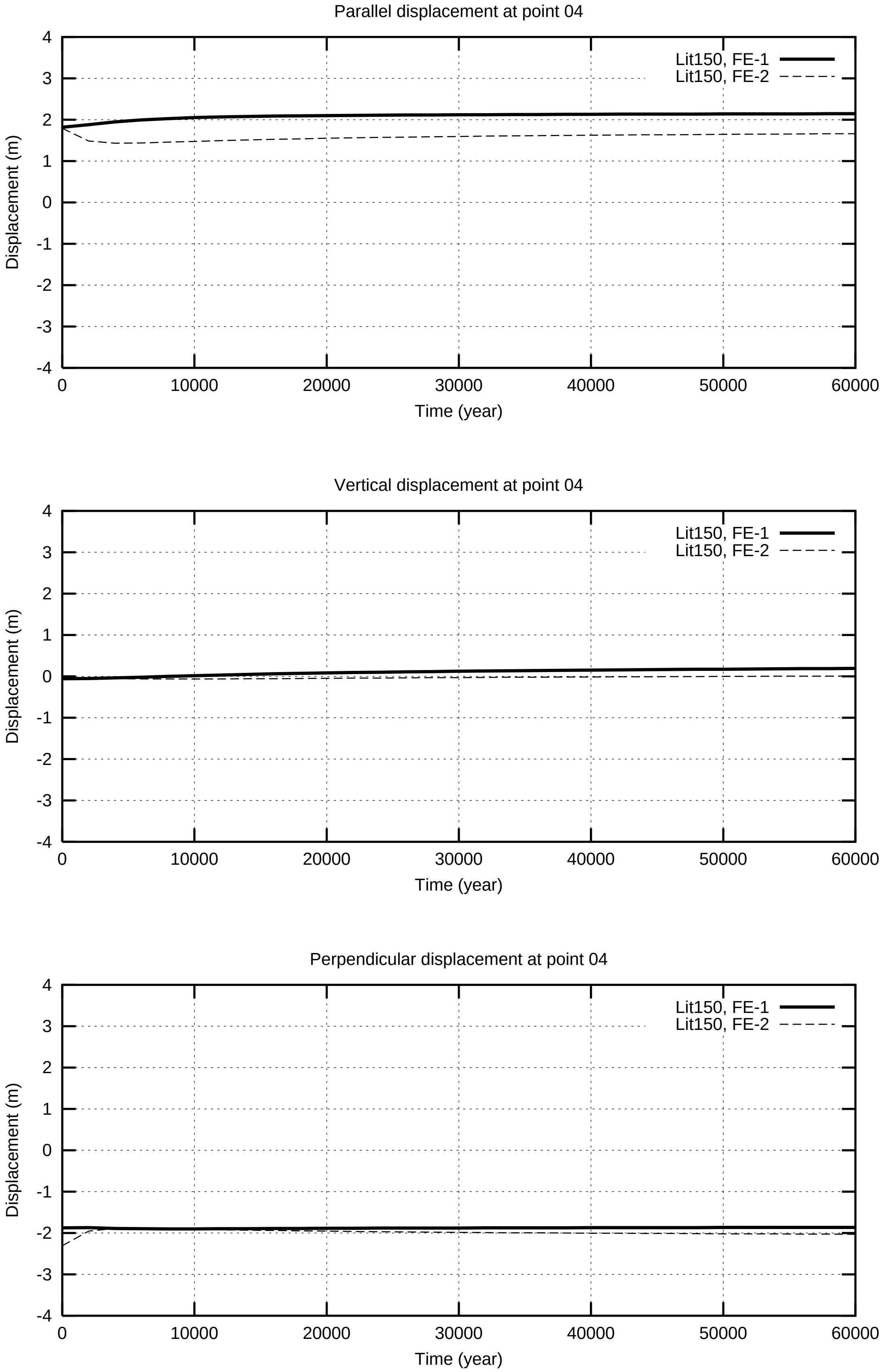

Figure 4.9: Parallel, perpendicular and vertical components of displacements at point 4 (figure 4.1) on the surface of model C

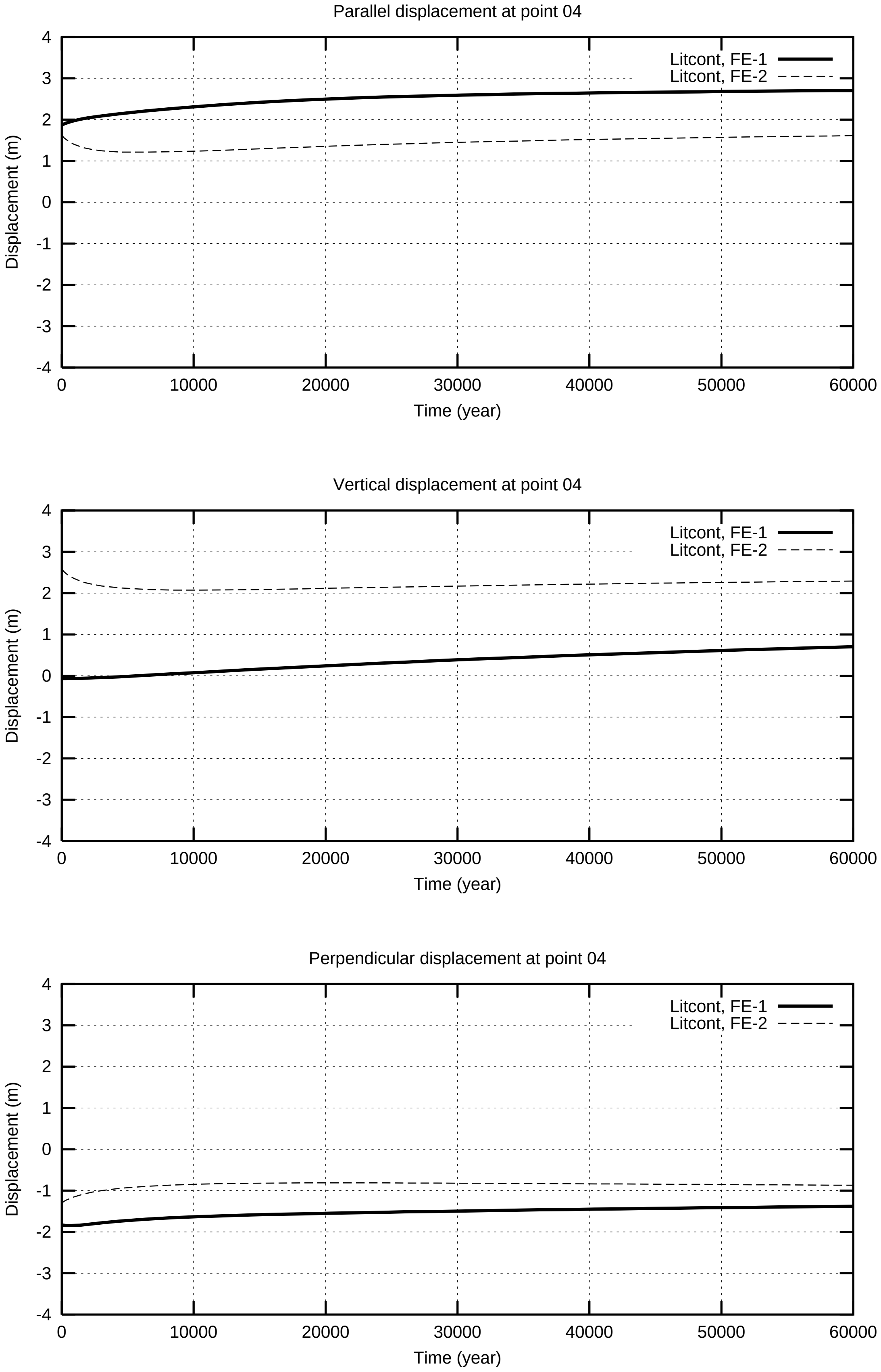

Figure 4.10: Parallel, perpendicular and vertical components of displacements at point 4 (figure 4.1) on the surface of model D

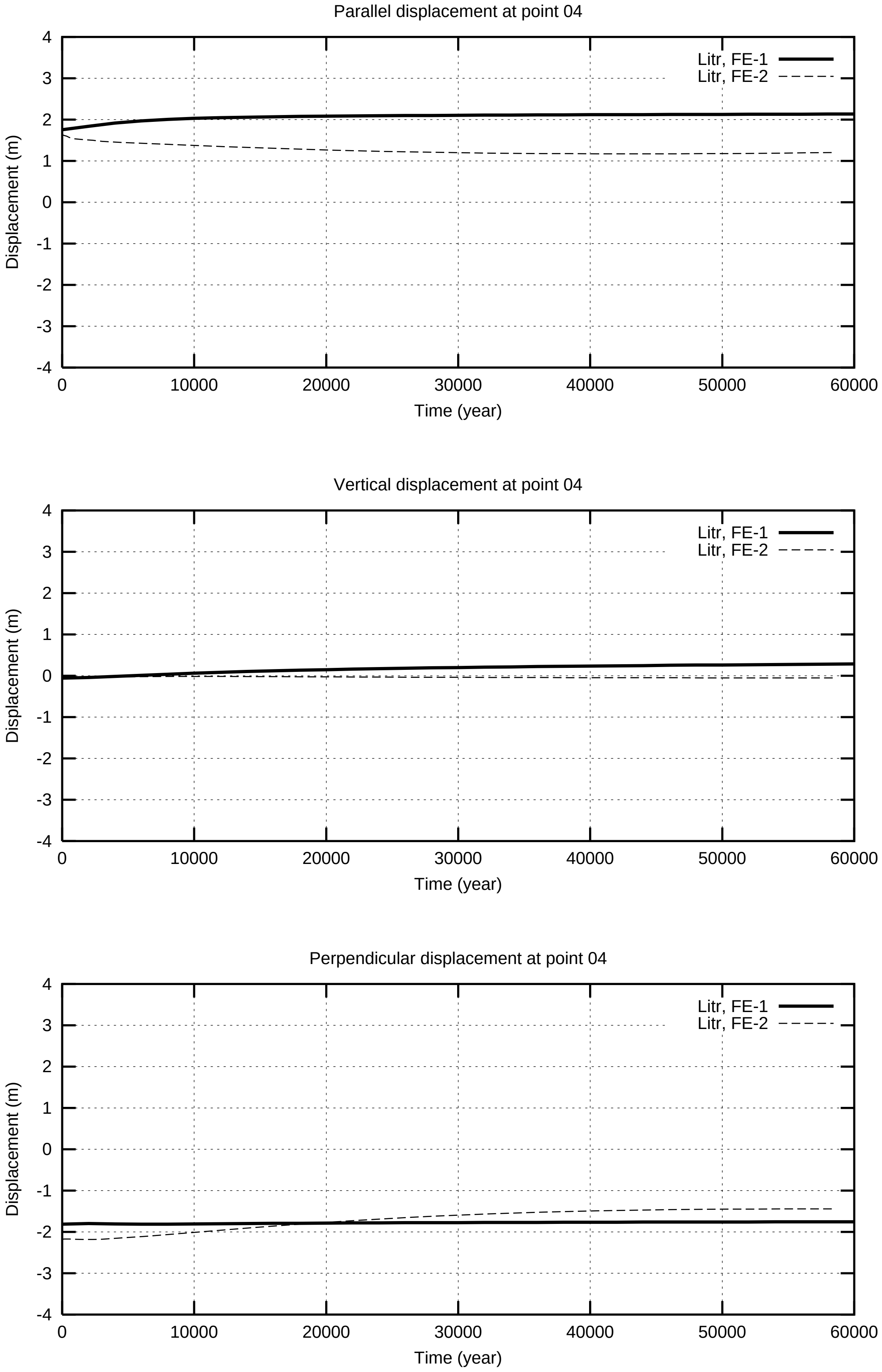

Figure 4.11: Parallel, perpendicular and vertical components of displacements at point 4 (figure 4.1) on the surface of model E

4.2 HOMOGENEOUS MODELS

4.2.1 Incompressible, Homogeneous, Isotropic, Linear Elastic Sphere

We start from the simplest spherical model. An advantage of this model is that this is one of our two models whose analytical solutions for the displacement field under surface loads are known. This can help us compare:

- Analytical solutions with and without the pre-stress field
- Analytical and numerical solutions

The view of the descretized model in polar orthographic projection system is represented in figure (4.12). The model properties are taken from §3.2.3.1 and are briefly reviewed here:

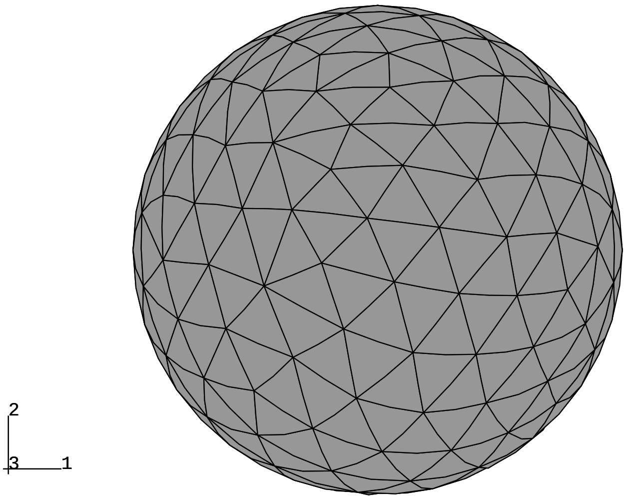

Figure 4.12: The tetrahedral model of the earth in polar orthographic projection

$$\begin{cases} R = 6371\ km \\ \rho = 5616\ \frac{kg}{m^3} \\ \lambda \to \infty \\ \mu = 6.10^{10}\ Pa \end{cases}$$

4.2.1.1 Surface Load

The surface load of §3.4.1 is applied to the model:

$$L(\theta) = 1.35 \times 10^7 (3\cos^2\theta - 1)\ Pa\ .$$

4.2.1.2 Results

The displacement field is shown in figure (4.13). Analytical solution of the radial component of displacement is known (Jeffreys [1970], Engels [1991] and Wolf [1997]).

The surface load of §3.4.1 is applied to the model (eq. 3.18). According to Jeffreys [1970] and Engels [1991], the radial component of surface displacement is computed by:

$$u_r(\theta) = \sum_{l,m} u_{r_{lm}} Y_{lm}(\theta)\ , \tag{4.1}$$

where $u_{r_{lm}}(\theta)$ are the spherical harmonic coefficients of the radial surface displacement (Wolf [1984]):

$$u_{r_{lm}} = -\frac{2l+1}{2(l-1)} \frac{R^3 \rho C^{ext}_{lm} + C^L_{lm} R}{\gamma_R \rho R + \mu \frac{2l^2+4l+3}{2}}\ , \tag{4.2}$$

(Wolf [1984], Amelung and Wolf [1994]) where:
R =earth's radius,

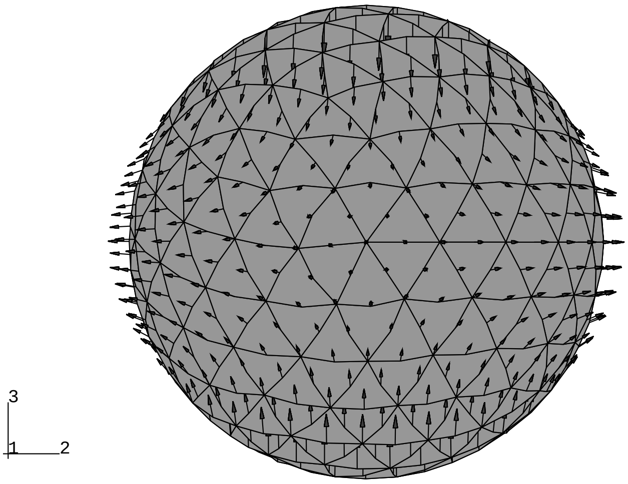

Figure 4.13: Numerical solution of displacement field of surface loads in equatorial orthographic projection

$\rho =$ density;
$\gamma_R =$surface gravity modulus,
$\mu =$ rigidity,
$C^{ext} =$load's potential,
$C^{L} =$load's pressure.

Pre-stress field is not considered in the present model, i.e. $\rho = 0$ in eq. (4.2). The load potential is not considered, the pressure of the load is introduced to the problem as an external stress field, therefore $C^{ext}_{lm} = 0$, and:

$$u_{r_{lm}} = -\frac{2l+1}{2(l-1)}\frac{C^L_{lm}R}{\mu\frac{2l^2+4l+3}{2}} \ . \tag{4.3}$$

The applied surface load is proportional to the second degree zonal harmonic, therefore only $C^L_{2,0} \neq 0$, and:

$$u_r(\theta) = u_{r_{2,0}} Y_2(\theta) \ , \tag{4.4}$$

from eq. (4.3):

$$u_{r_{2,0}} = -\frac{5}{19}\frac{C^L_{2,0}R}{\mu} \ . \tag{4.5}$$

Substitutions for the model parameters:

$$u_{r_{2,0}} = -754.46 \ m \ ,$$

$$u_r(\theta) = -337.23(3\cos^2\theta - 1) \ . \tag{4.6}$$

The analytical and numerical solutions for the radial component of the displacement vector of a meridian section are plotted in figure (4.14). The two values are plotted from the north pole on a meridian towards the south pole. At the equator the dislocation has a maximum.

As expected from figure (4.13) the maximum subsidence and uplift are on the poles and the equator, respectively. Figure (4.14) shows a promising coincidence of the analytical and numerical results. Taking into account the points that this is only for 1849 elements, we can expect that for more difficult problems, e.g. a more complicated force field or structure of the model earth, increase of the number of the elements can keep an acceptable accuracy, an assumption that should be checked.

The following figures show contours of Cartesian displacement components.

Figure (4.15) shows that the maximum u_1 takes place on the $x-$axis.

According to figure (4.16) the u_2 component vanishes on $x-$axis.

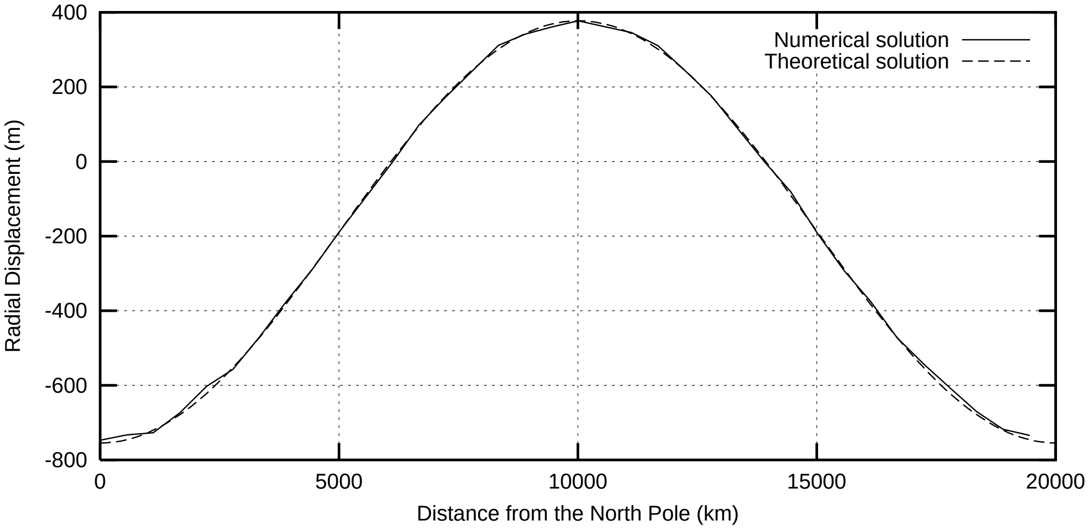

Figure 4.14: Comparison of radial displacements on the surface of an incompressible, elastic, homogeneous, isotropic, non-gravitational sphere under surface loads. There are 2862 nodes and 1849 elements in the model, with a characteristic length of 2457 km.

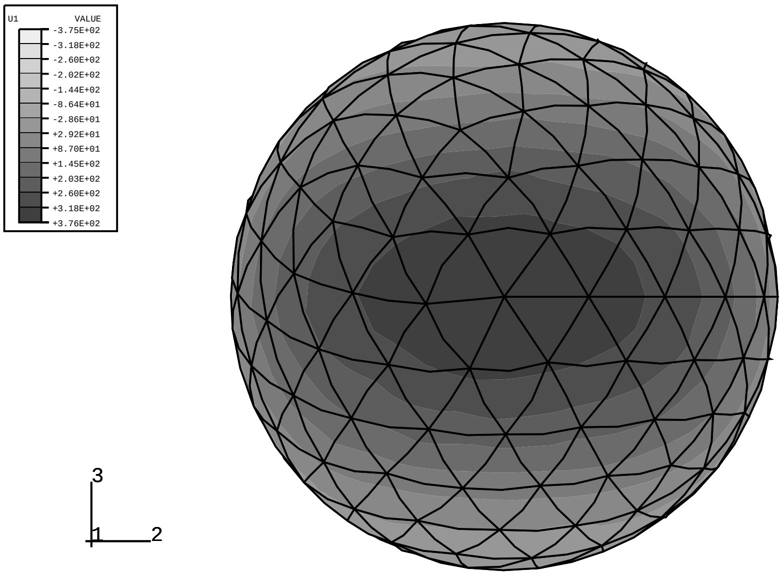

Figure 4.15: View of the displacement component u_1 along the $x-$axis in equatorial orthographic projection, values presented in meters

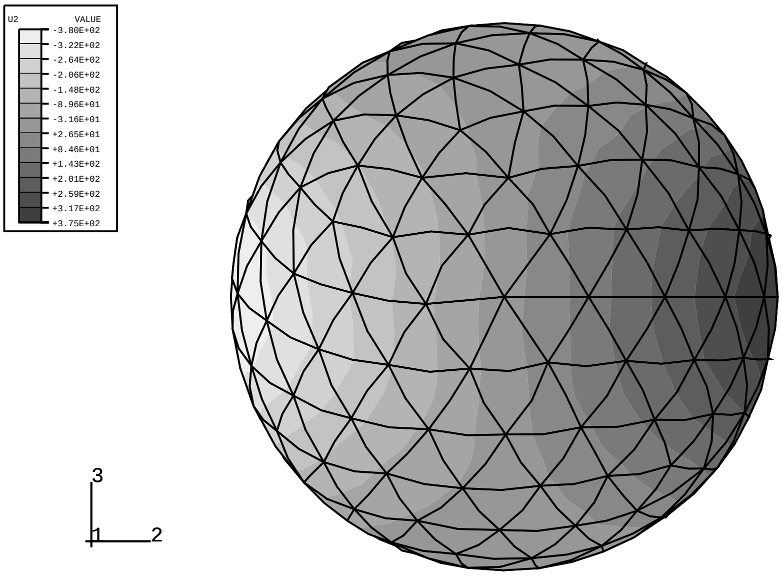

Figure 4.16: View of the displacement component u_2 along the $x-$ axis in equatorial orthographic projection, values presented in meters

Figures (4.17)-(4.20) are self explanatory.

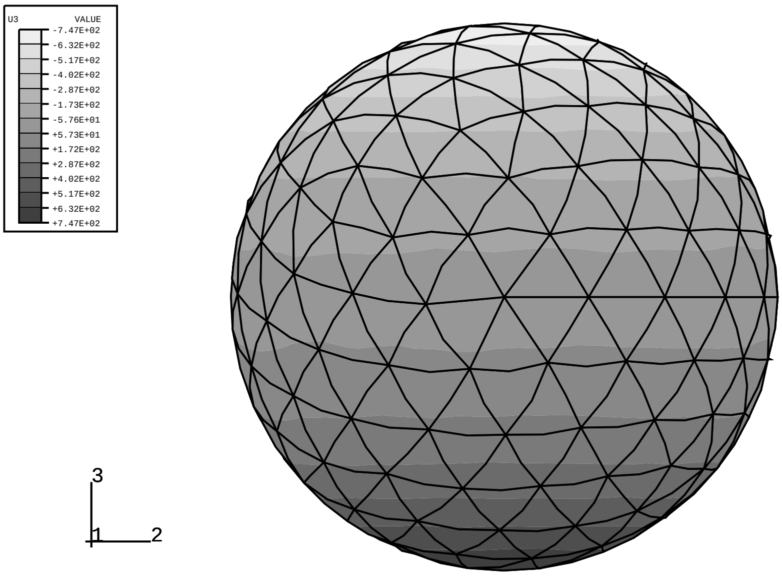

Figure 4.17: View of the displacement component u_3 along $x-$axis in equatorial orthographic projection, values presented in meters

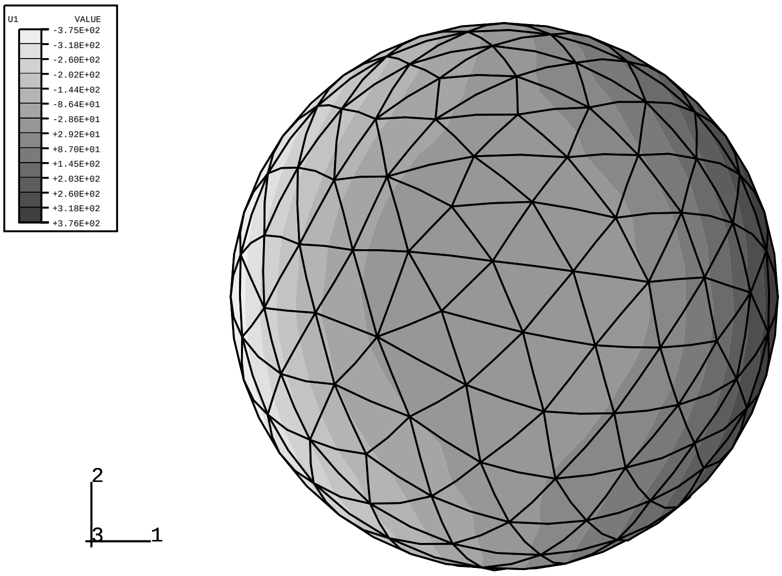

Figure 4.18: View of the displacements component u_1 along $z-$axis in equatorial orthographic projection, values presented in meters

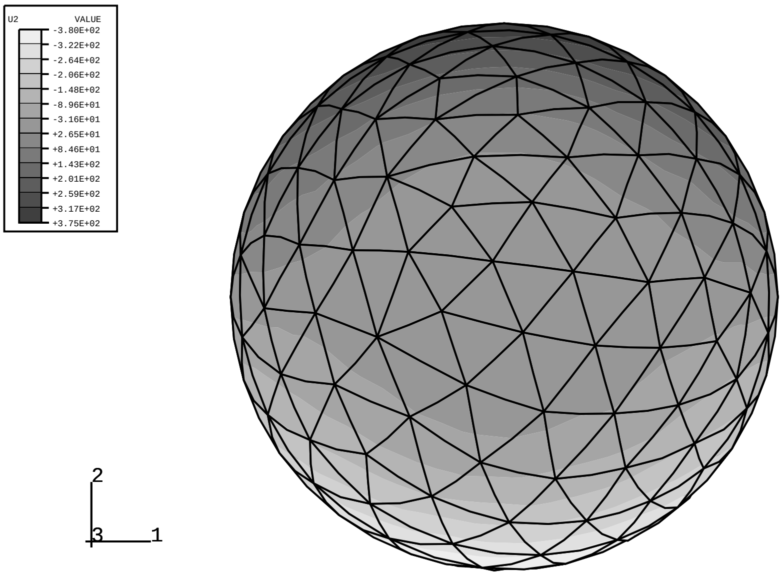

Figure 4.19: View of the displacement component u_2 along $z-$axis in equatorial orthographic projection, values presented in meters

4.2.2 Incompressible, Pre-Stressed, Homogeneous, Isotropic, Linear Elastic Sphere

Now we turn to a pre-stressed model, and take into account the self-gravitational prestress field according to the eqs. (3.13) and (3.14). We apply a surface load again, and in the model response investigation we compare the analytical solutions of the pre-stressed and non-gravitational models.

4.2.2.1 Surface Load

With $\rho = 5616\frac{kg}{m^3}$ in eq. (4.2), instead of $\rho = 0$ for a non-gravitational model, we end up with:

$$U_r = -\frac{5}{2}\frac{C_2^L R}{2\rho g R + 19\mu} Y_2 \tag{4.7}$$

for the pre-stressed model.

Let us start with the analytical solution for the radial displacement field of the surface load specified

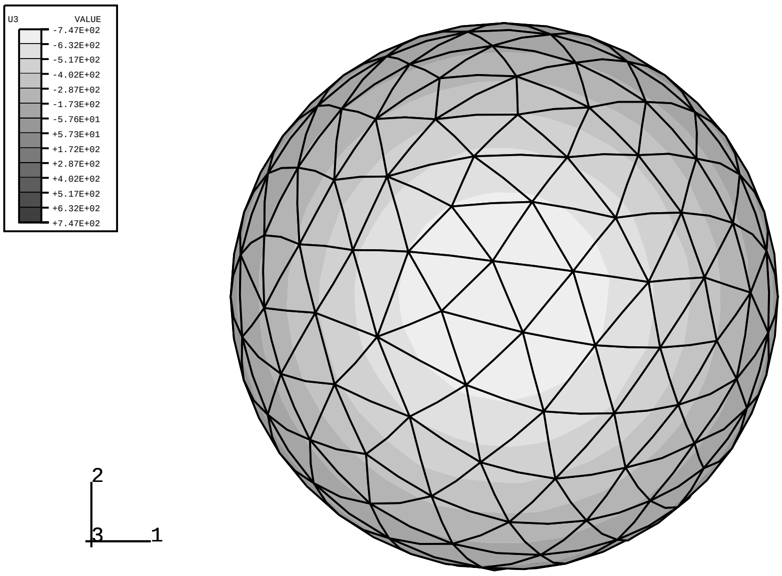

Figure 4.20: View of the displacement component u_3 along $z-$axis in equatorial orthographic projection, values presented in meters

above, and compare it with that for the pre-stress-free case (§4.2.1.2). The two cases are shown in figure (4.21), which underlines the importance of self-gravitational prestress field.

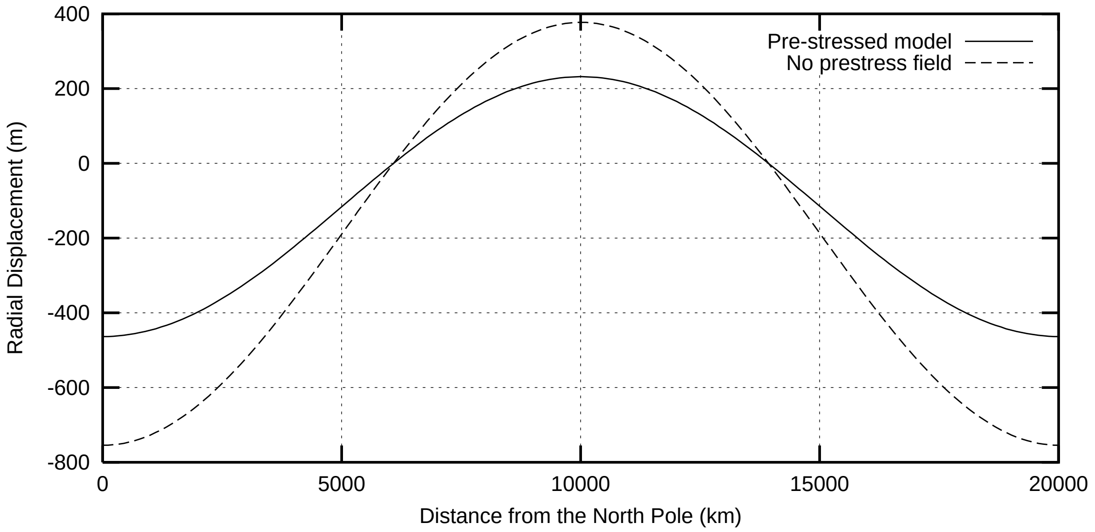

Figure 4.21: Comparison of analytical radial displacement fields under the surface loads for pre-stressed and no-pre-stress spheres

4.2.2.2 Results

Analytical and numerical solutions for the radial displacement field are compared in figure (4.22)

An important point is how a numerical method can handle the pre-stress effect, although this can be observed by comparing the figures (4.14 and 4.22). In order to get a clear picture, we compute the differences between analytical solutions for the radial component of displacement of not pre-stressed and pre-stressed models under surface loads, and the same difference for numerical solutions. The former difference is the effect of gravitational pre-stress on analytical solution, and the latter on numerical solution, the last two curves are compared.

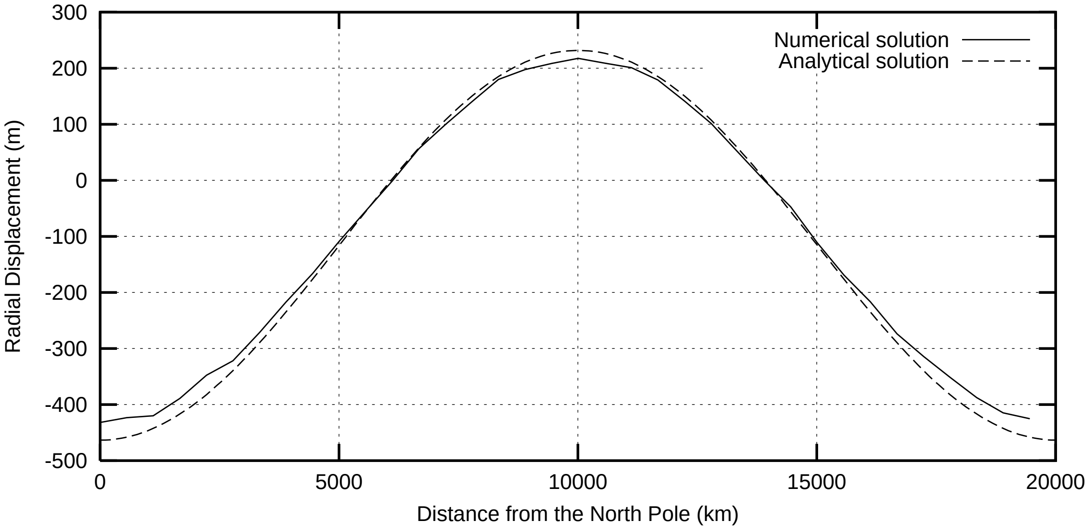

Figure 4.22: Analytical and numerical solutions of the radial displacement field due to surface loads applied to an incompressible pre-stressed homogeneous isotropic linear elastic sphere

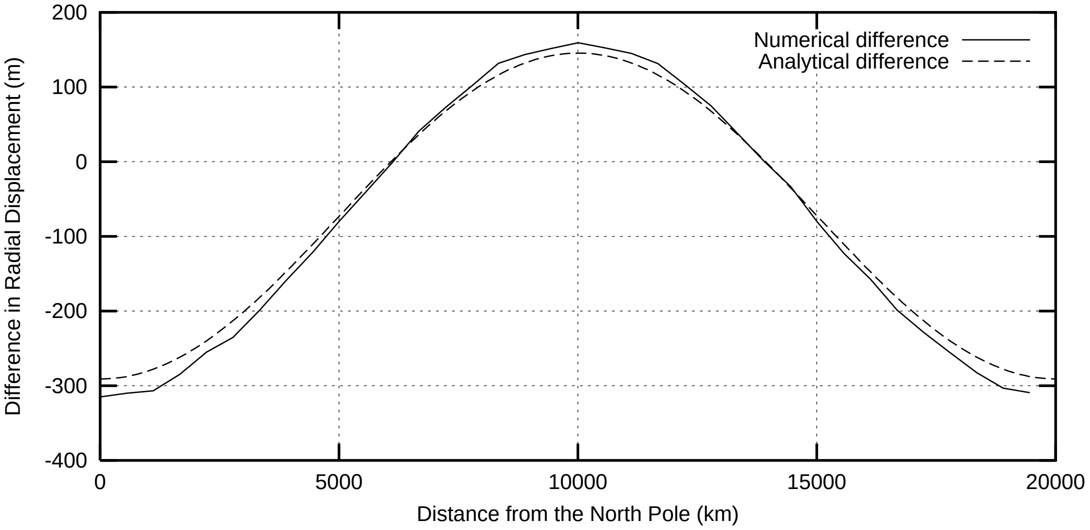

Figure 4.23: Pre-stress effect on analytical and numerical earth models respectively, the effect in each case is computes as the difference of the pre-stressed and no-prestress model

4.2.3 Incompressible, Homogeneous, Isotropic, Maxwell, Viscoelastic Sphere

For the case of a viscoelastic sphere, we apply two different deformation sources, surface load, similar to the previous models, and dipolar source. The importance of the latter source is that fault motions can be described by the accumulation of dipolar sources, as discussed in §B.5.2.

Since time is an important factor in viscoelastic deformation, in the application of the surface loads, we apply the load for a short time, then remove the load gradually to see how the model responds to this stress field variation. The model response is computed for a long time after stress removal. This type of computation is only of interest to see how the model responds to a time varying source, otherwise the source is far from the real sources.

4.2.3.1 Surface Load

We apply the surface load as given in eq. (3.18). After a short time the load is removed linearly and slowly with time. In this example it is applied for 20 minutes, then removed linearly in 4 months. The strain variations are investigated up to one year after the application of the surface loads.

4.2.3.2 Results of Application and Removal of the Surface Load

The results for this temporal load field are plotted in figure (4.24). Comparison of the first curve, i.e. right after the stress application, with that for an elastic, non-gravitational sphere reveals that the instantaneous response of the model is as in the elastic case. This is expected for a Maxwell fluid, as discussed in §C.2.1 and shown in figure (C.4).

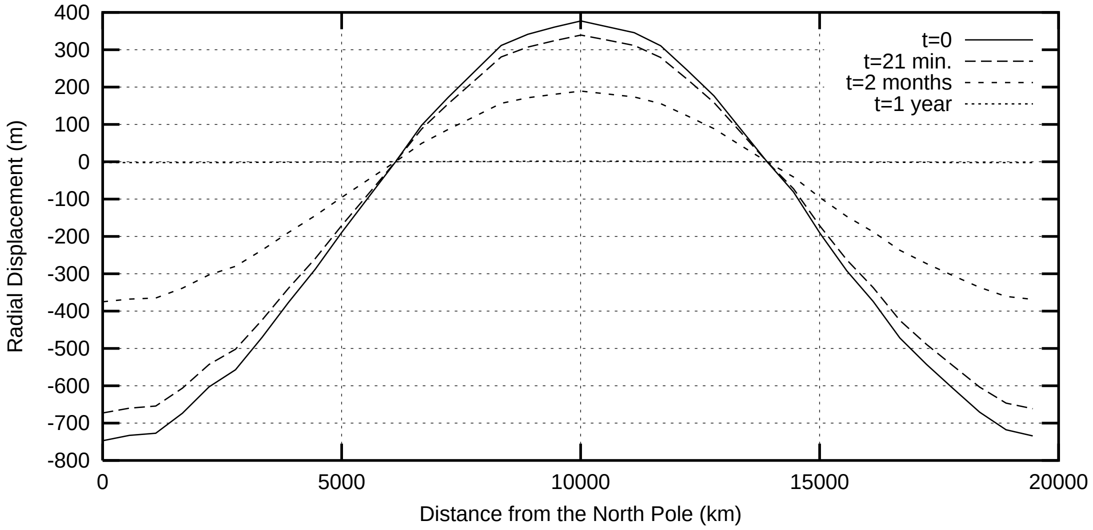

Figure 4.24: Temporal variations of the radial displacement field, the plotted curves are in the legend from top to the bottom, radial displacement right after the application of the surface load, shortly after starting its removal, in the middle of the stress removal phase, and long after the total stress removal, exact times are stated in the legend

Then, as the stress is removed, the model earth relaxes gradually to its hydrostatical equilibrium state. In contrast to the Maxwell model of figure (C.4) which remains deformed even long time after stress removal, the model earth recovers its original shape, the phenomenon is due to the pre-stress field.

4.2.3.3 Dipolar Source

As a primary dislocation source, we apply a dipole, and investigate the behavior of our model earth. A pressure of 1.10^{19} Pa is applied at two points whose connecting line is parallel to the $x-$axis, with the point $(0, R, 0)$ where R is the radius of the model earth (figure 4.26).

Contours of the displacement component u_1 and strain component ϵ_{11} are presented in figures (4.27) and (4.28). Both figures apply to the time right after the application of the dipole.

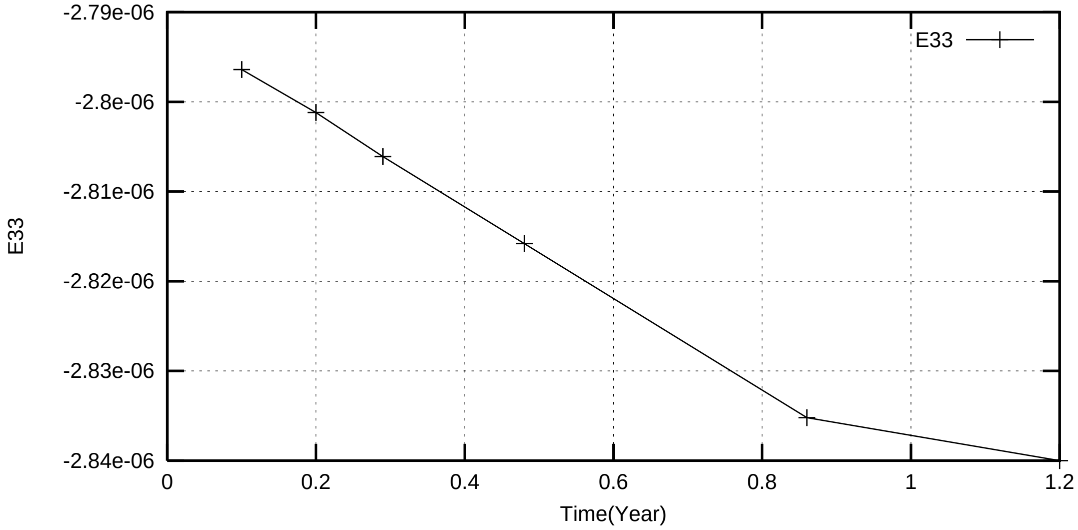

Figure 4.25: Temporal variations of the strain component ϵ_{33} at the north pole

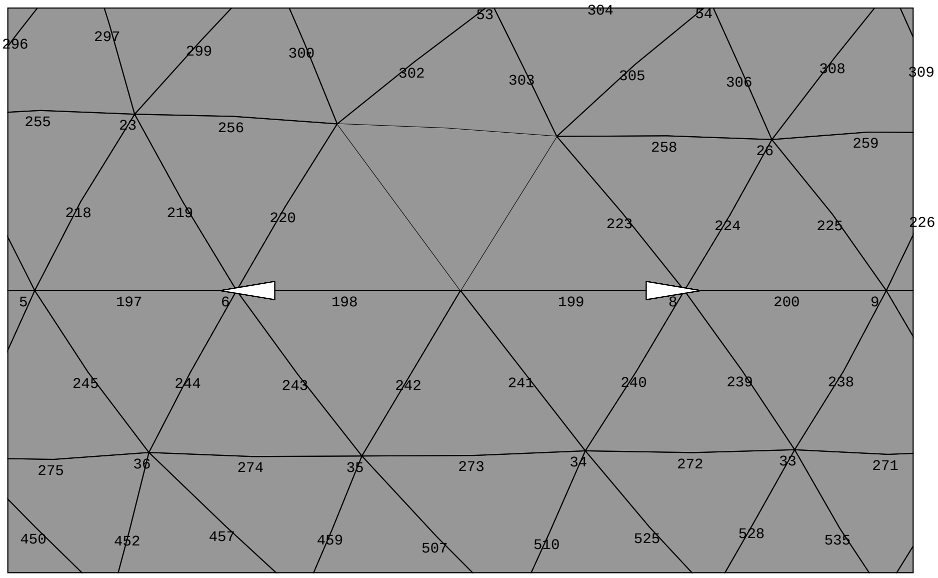

Figure 4.26: A dipole, applied on the the two sides of the point $(0, R, 0)$ in the $x-$direction, dipole $(1, 1)$ according to figure (B.4)

4.3 NON-HOMOGENEOUS MODELS

This section presents the results for the non-homogeneous models introduced in §3.3. Comparison of the models leads to insight into the role of the individual parameters. The effect of the lithosphere and its rigidity are investigated. Temporal variations of displacement components are presented, i.e. displacement versus time curves.

In the remainders of this chapter, the deformation sources are always a two dimensional vertical right lateral strike-slip fault, a cross section of which is the dark area of figure (3.5). In order to have an estimate of the approximation error, each quantity is computed two times based on different finite element models. Finite element model 1 is consists 13248 elements with an average length of 1025 km, while finite element model 2 is made of 8503 elements with an average side length of 1263 km. Linear approximation (appendices A-C) is used everywhere in this study, on account of the small displacement with respect to the model size, i.e. a few meters in a sphere of $R = 6371$ km.

Some abbreviations are used in the plots and their legends, the abbreviations are as follows:

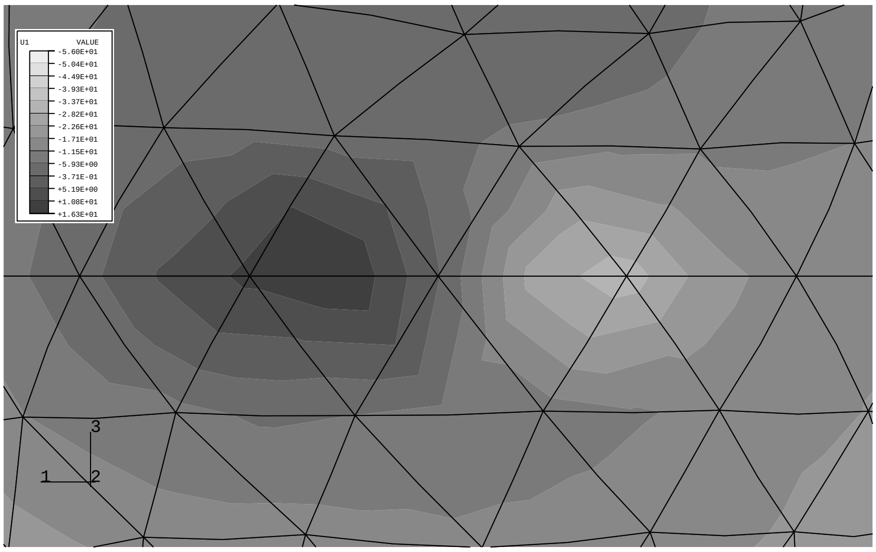

Figure 4.27: u_1 component of the displacement field of $(1, 1)$ dipole, values presented in meters

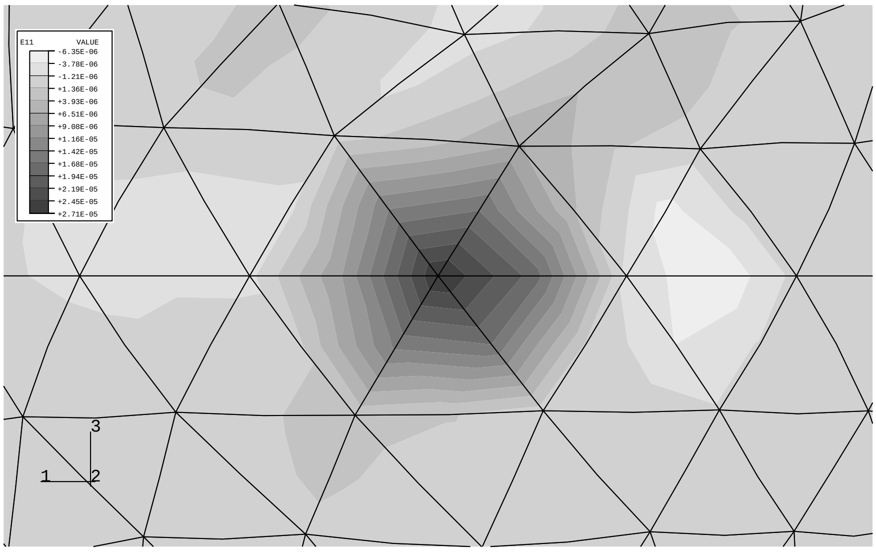

Figure 4.28: ϵ_{11} strain component of the displacement field of $(1, 1)$ dipole

- Lit00 := No lithosphere (Model A, §3.3)
- Lit 50 := 50 km thick lithosphere (Model B, §3.3)
- Lit150 := 150 km thick lithosphere (Model C, §3.3)
- Litcont := Laterally heterogeneous lithosphere (Model D, §3.3)
- Litr := 150 km thick lithosphere with constant rigidity (Model E, §3.3)
- FE-1 := Finite element model 1 (see above)
- FE-2 := Finite element model 2 (see above)
- Point xx := Point numbers (figure 4.1)

4.3.1 Model A, no Lithosphere (Lit00)

We begin this part of the analysis with the three layer model A, which includes core, lower and upper mantle, but no lithosphere. This model gives an impression of the creep phase of a Maxwellian viscoelastic body (§C.2).

A vertical fault of 1000 km length and 50 km depth is assumed in this model, a 2 m slip is applied instantaneously to the fault, each side of the fault slips 2 m horizontally, then the fault is assumed to remain without any motion after the slip. The displacement field over the rest of the model is computed. The temporal variations of the displacement at a point, not far from the fault, is plotted in figure (4.29). Three different components are plotted, parallel to the fault slip, perpendicular to the fault slip in horizontal direction and vertical. The deformation starts with the elastic response and continue to creep. According to the figures the vertical component is rather small (figures 4.29-4.31).

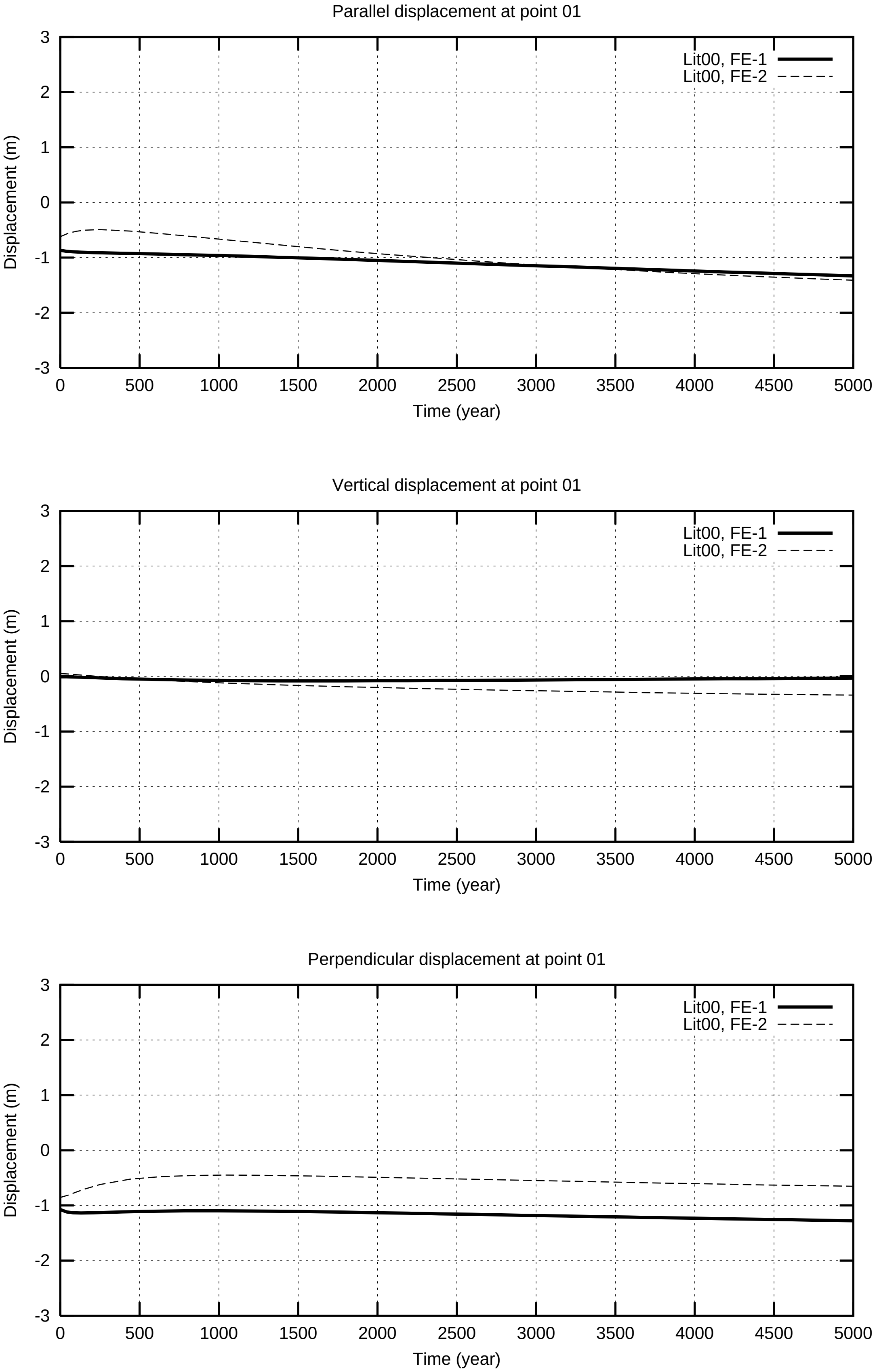

Figure 4.29: Temporal variations of displacement at point 1 (figure 4.1), in response to a right lateral strike-slip dislocation of 2 m on a vertical fault in Model A (no lithosphere).

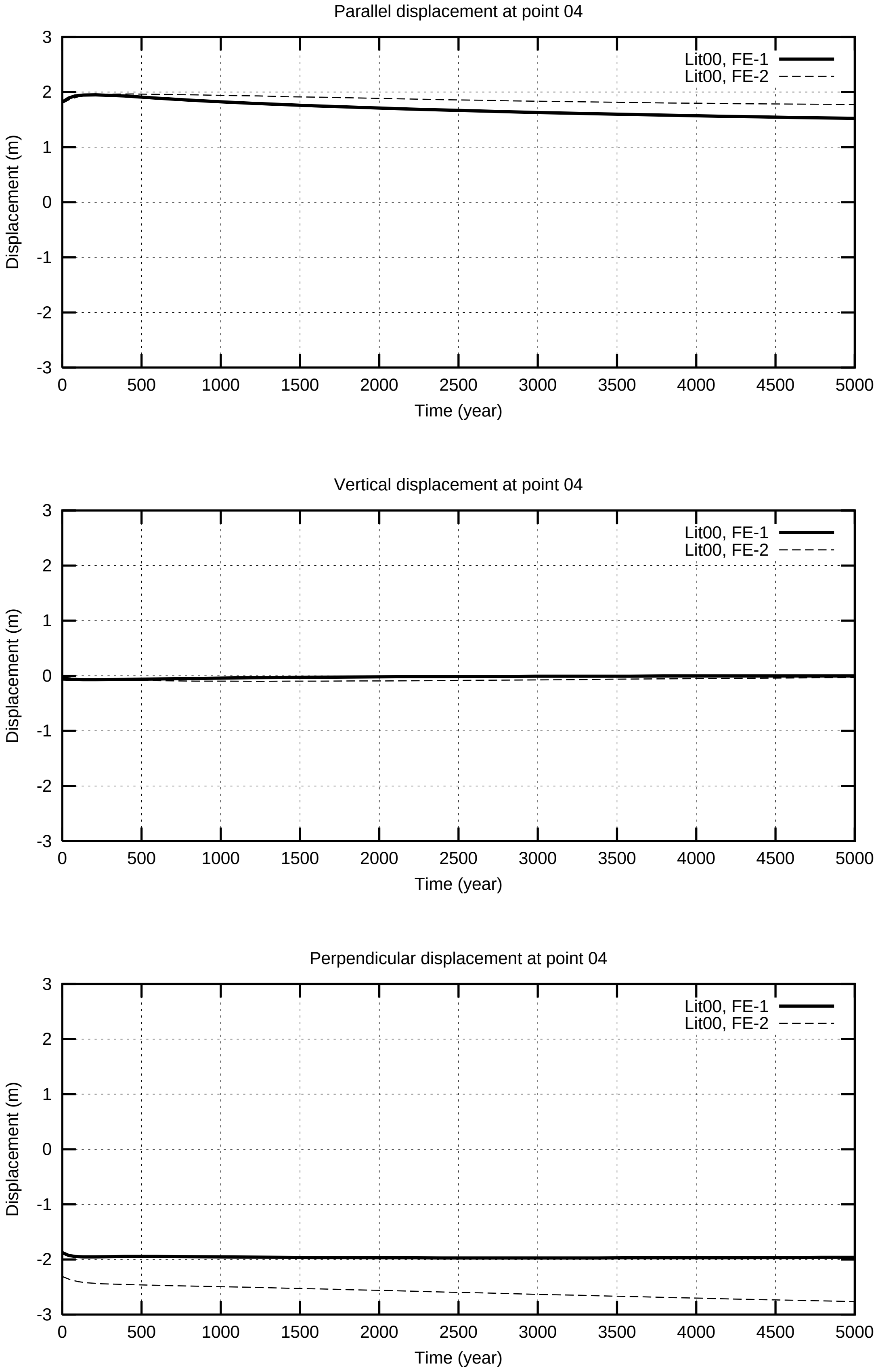
Parallel displacement at point 04

Vertical displacement at point 04

Perpendicular displacement at point 04

Figure 4.30: Temporal variations of displacement at point 4 (figure 4.1), in response to a right lateral strike-slip dislocation of 2 m on a vertical fault in Model A (no lithosphere).

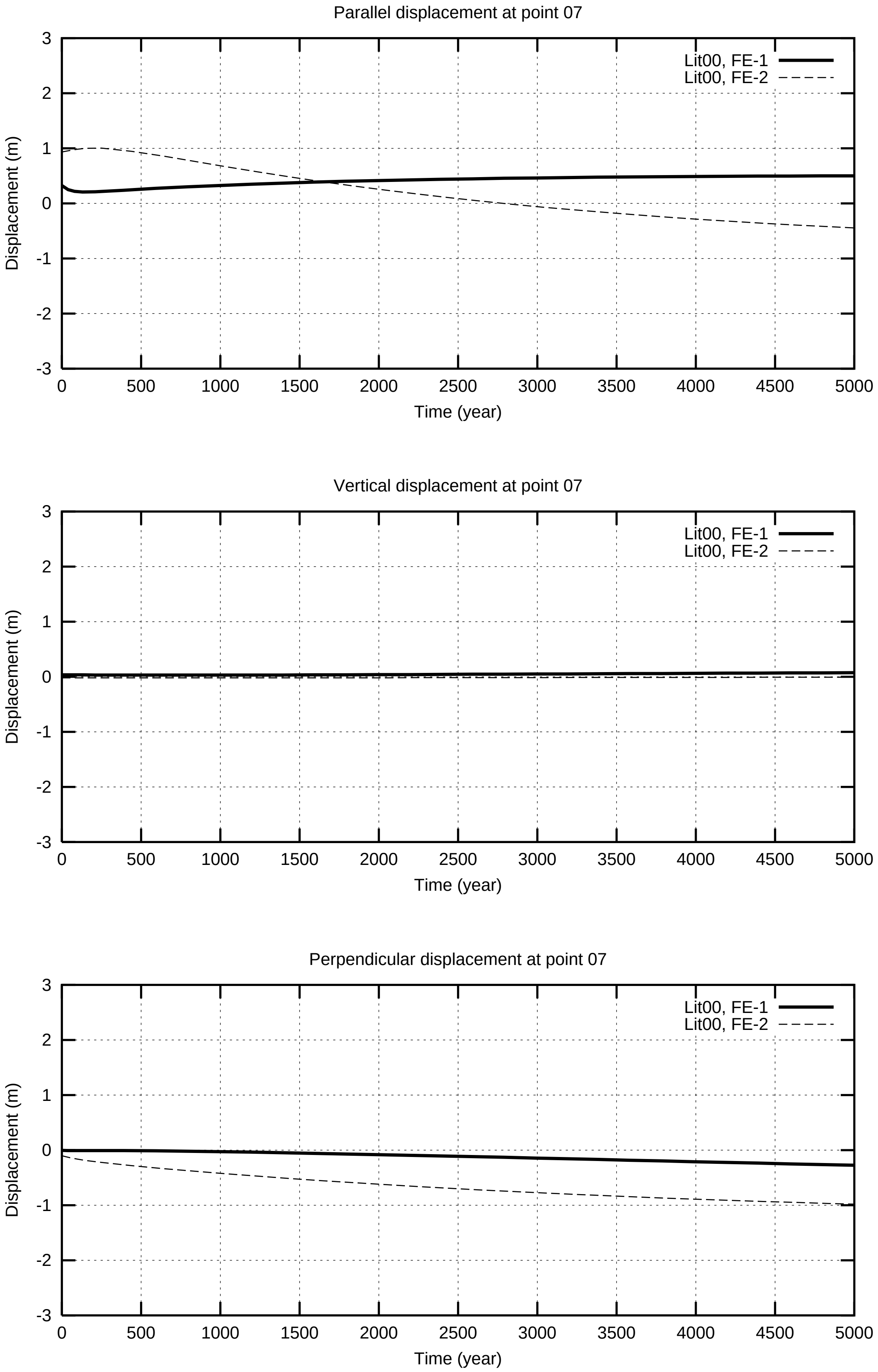

Figure 4.31: Temporal variations of displacement components at point 7 (figure 4.1), in response to a right lateral strike-slip dislocation of 2 m on a vertical fault in Model A (no lithosphere).

4.3.2 The Effect of Lithosphere

The components of the displacement vectors at the given points are plotted versus time for different thicknesses of the lithosphere, a comparison of which can lead to an assessment of the role of the lithosphere in the earth response to the applied source.

Figure (4.32) represents a comparison of parallel displacement component for the three models A, B and C, i.e. with 0, $50km$, and $150km$ thick lithospheres. Figures (4.33-4.37) plot the same curves at other points.

All these figures show that without lithosphere the displacements continue to relatively large values in the long run, while an elastic lithosphere is like an obstacle in this process. The thicker the lithosphere, the faster the displacements after the dislocation, and the faster the relaxation.

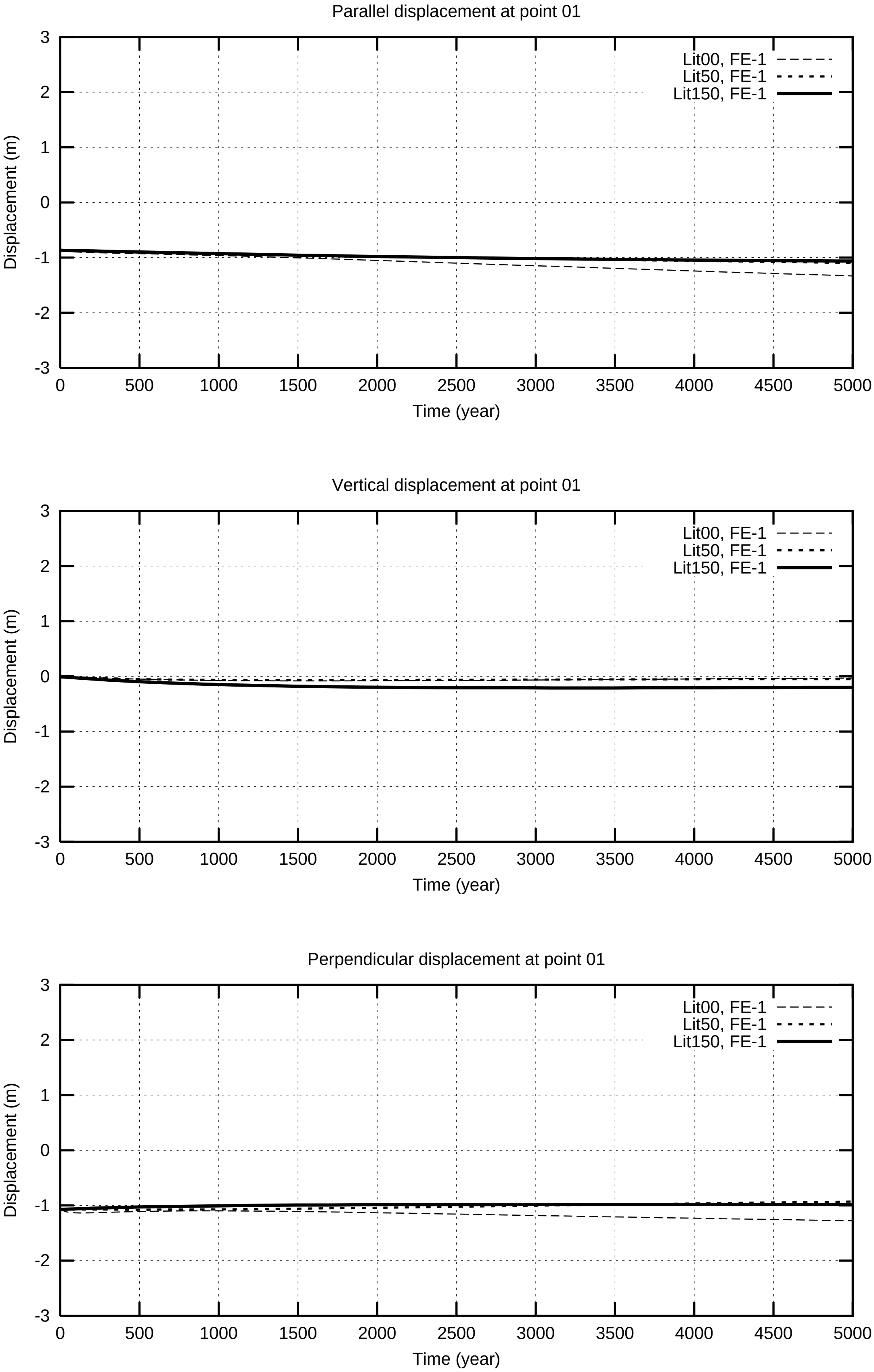

Figure 4.32: Temporal variations of displacement components for three models: without lithosphere (Model A, Lit00), with a 50 km thick lithosphere (Model B, Lit50) and 150 km lithosphere (Model C, Lit150) at point 1 (figure 4.1).

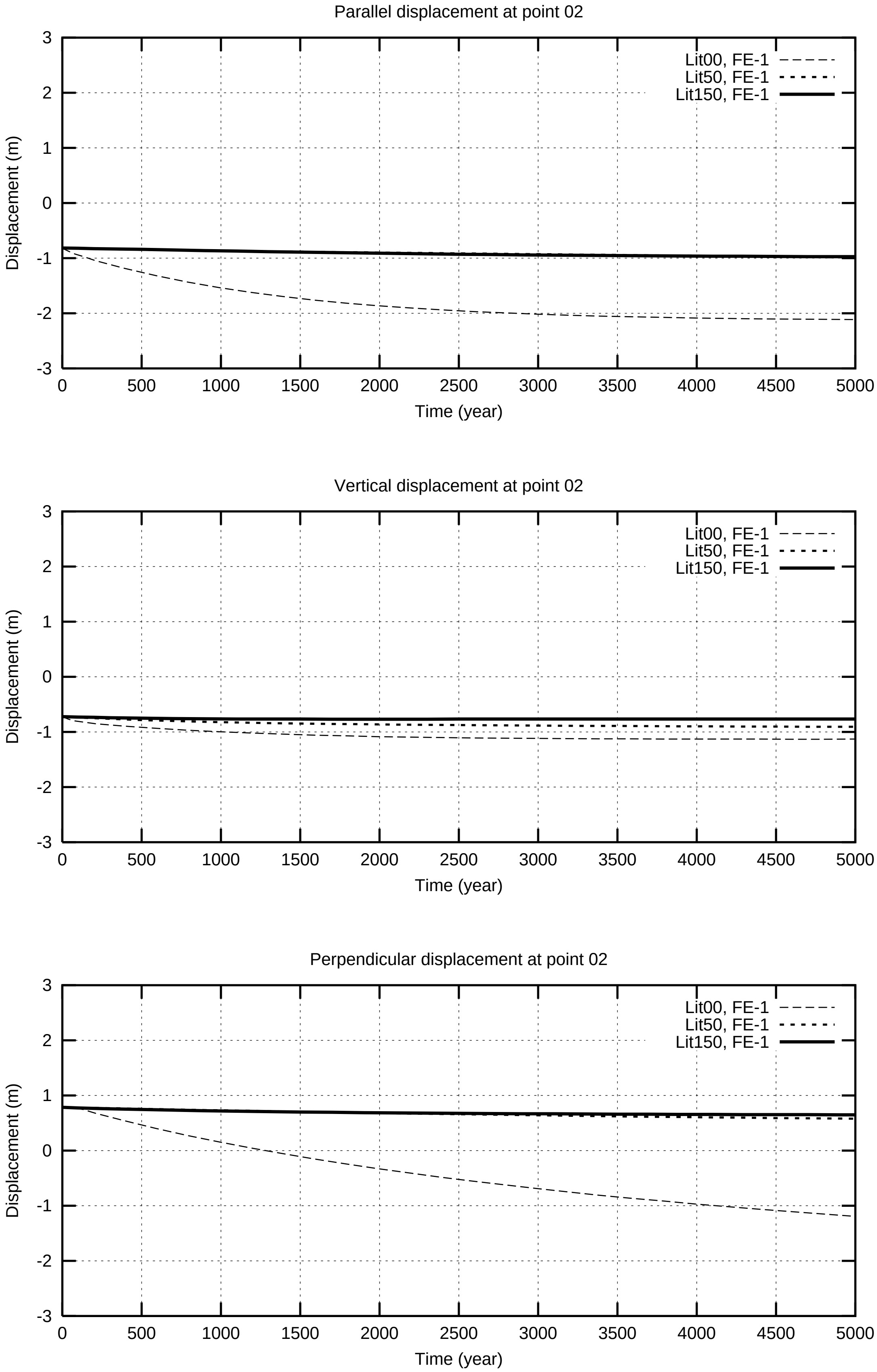

Figure 4.33: Temporal variations of displacement components for three models: without lithosphere (Model A, Lit00), with a 50 km thick lithosphere (Model B, Lit50) and 150 km lithosphere (Model C, Lit150) at point 2 (figure 4.1).

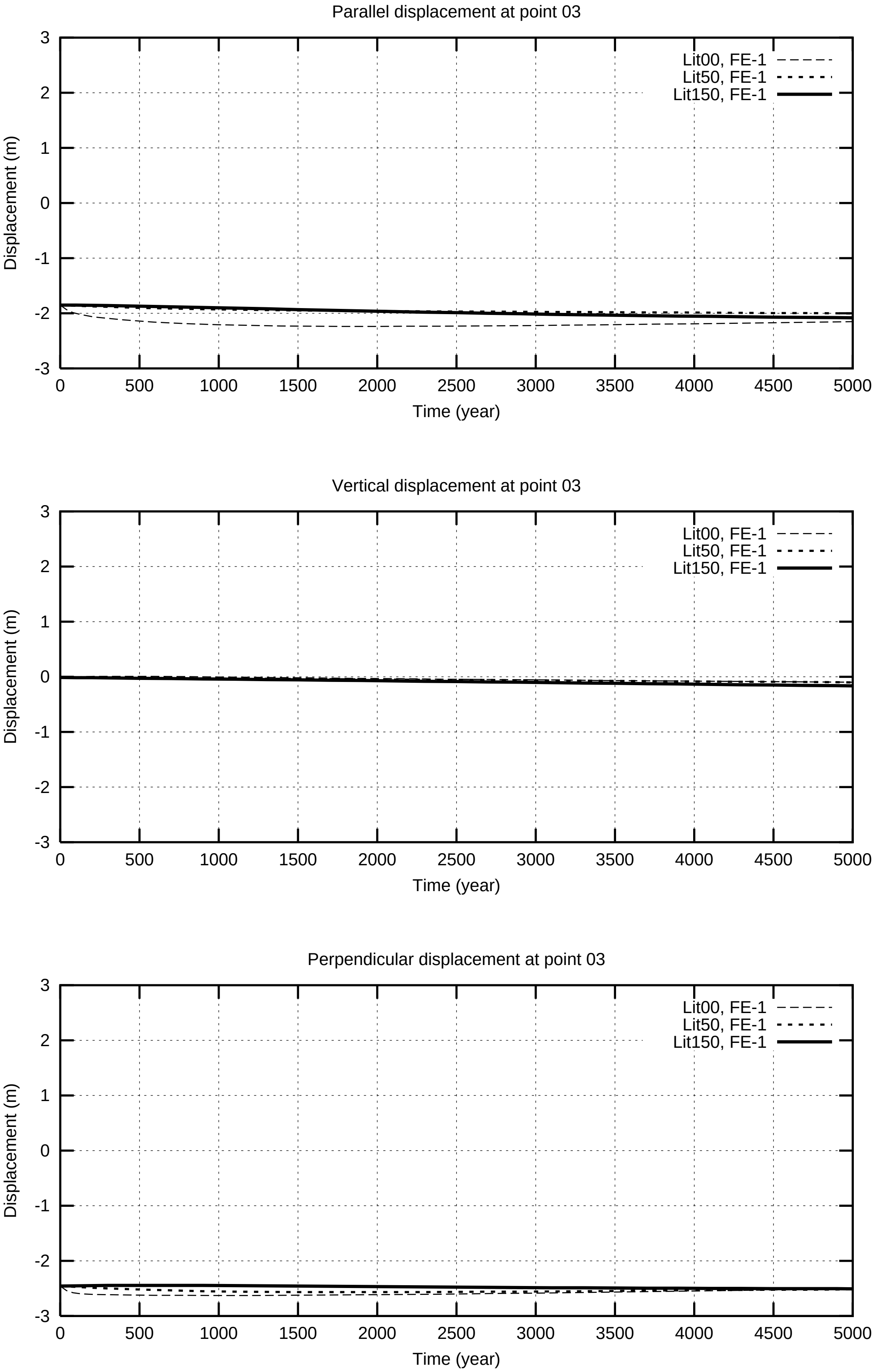

Figure 4.34: Temporal variations of displacement components for three models: without lithosphere (Model A, Lit00), with a 50 km thick lithosphere (Model B, Lit50) and 150 km lithosphere (Model C, Lit150) at point 3 (figure 4.1).

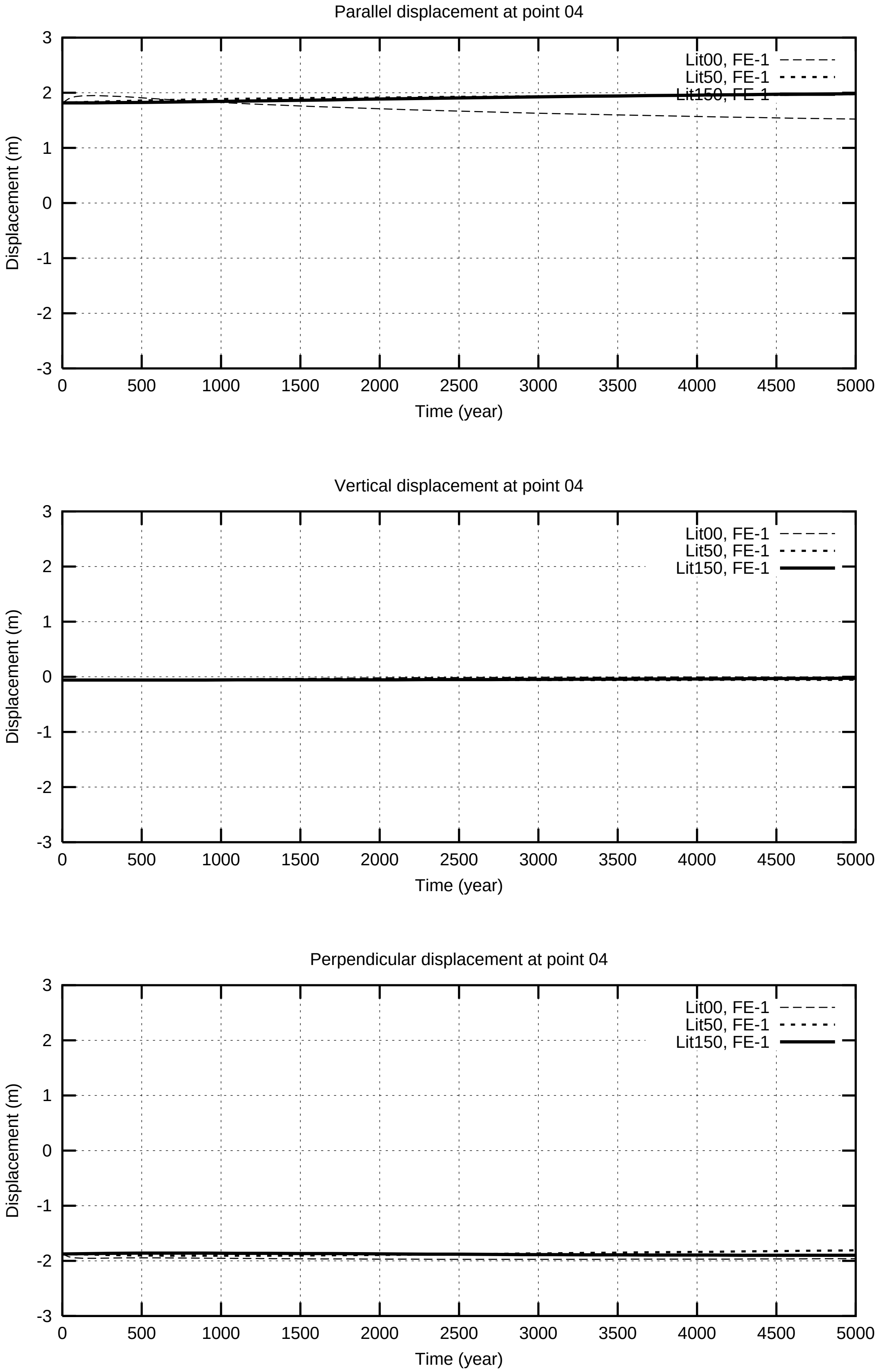

Figure 4.35: Temporal variations of displacement components for three models: without lithosphere (Model A, Lit00), with a 50 km thick lithosphere (Model B, Lit50) and 150 km lithosphere (Model C, Lit150) at point 4 (figure 4.1).

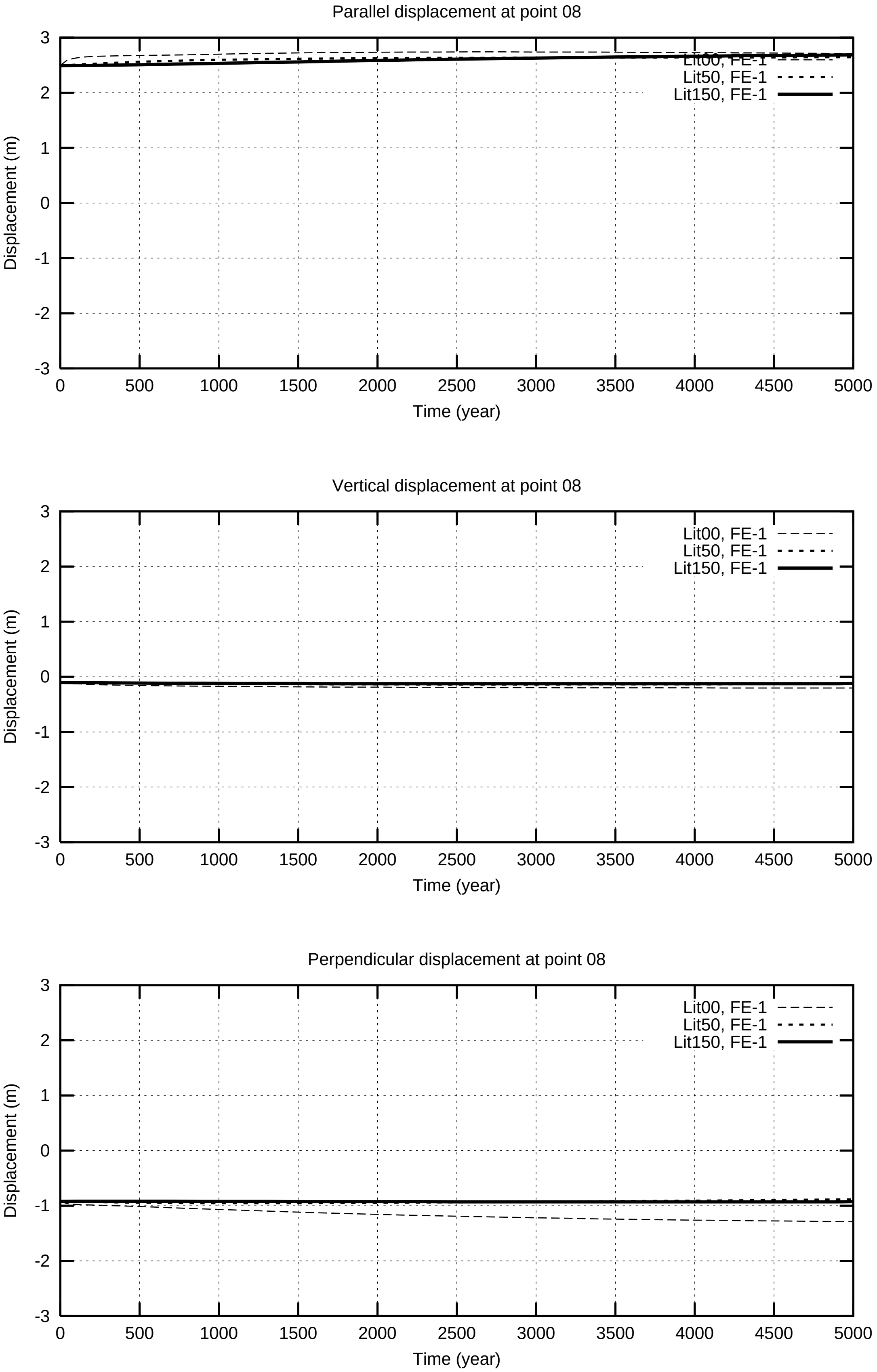

Figure 4.36: Temporal variations of displacement components for three models: without lithosphere (Model A, Lit00), with a 50 km thick lithosphere (Model B, Lit50) and 150 km lithosphere (Model C, Lit150) at point 8 (figure 4.1).

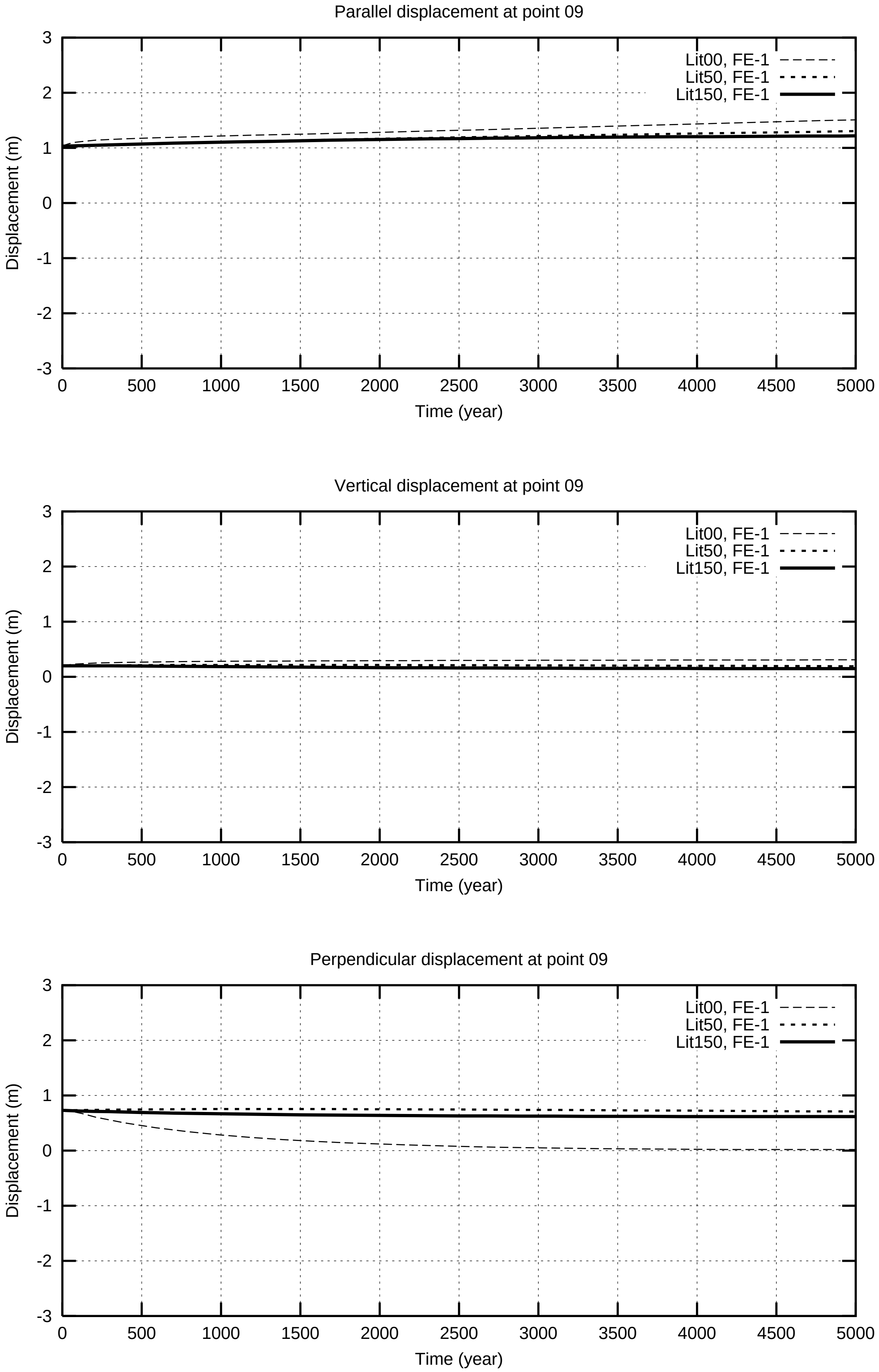

Figure 4.37: Temporal variations of displacement components for three models: without lithosphere (Model A, Lit00), with a 50 km thick lithosphere (Model B, Lit50) and 150 km lithosphere (Model C, Lit150) at point 9 (figure 4.1).

4.3.3 Laterally Heterogeneous Lithosphere

In this section the response of the laterally heterogeneous model (model E, §3.3.4) is computed and compared with the radially symmetric models. The displacement curves are plotted for different points, in the middle and on the margin of the continental plate, and on the oceanic plate. They are then compared with the motions of the same points in radial models and the same source.

Figures (4.38-4.40) show the displacement curves of three points on the continental plate, and at the same points in two radially symmetric models, with 50 km (model B) and 150 km (model C) thicknesses of lithosphere. The three figures show that as the point of interest goes further from the fault neighborhood towards the middle of the continental plate, the displacement curve approaches the corresponding curve in model C in which the lithosphere is as thick as the continental plate. This means that in this model the continental points, far from the oceans are not affected by the variations of viscosity under the oceanic plate, particularly in the short run. As times goes on, the continental curve diverges from that of model C, i.e. the effect of non-homogeneity is felt after a long time in the middle of the continent. A comparison of motions on three different points, point 11 on the extension of the fault, points 12 and 13 at different distances from the fault plane, reflects the same conclusion (Figs. 4.41-4.43).

The same quantities are plotted for point 14 on the continental plate, far from the fault and close to the oceanic plate (figure 4.1). In the beginning the continental model curve is close to that of symmetric models, but separates from it earlier. This means that on the margin of the continental plate, the viscosity of the mantle is felt earlier: the closer to the shallower plate, the sooner it is affected by the mantle beneath the ocean.

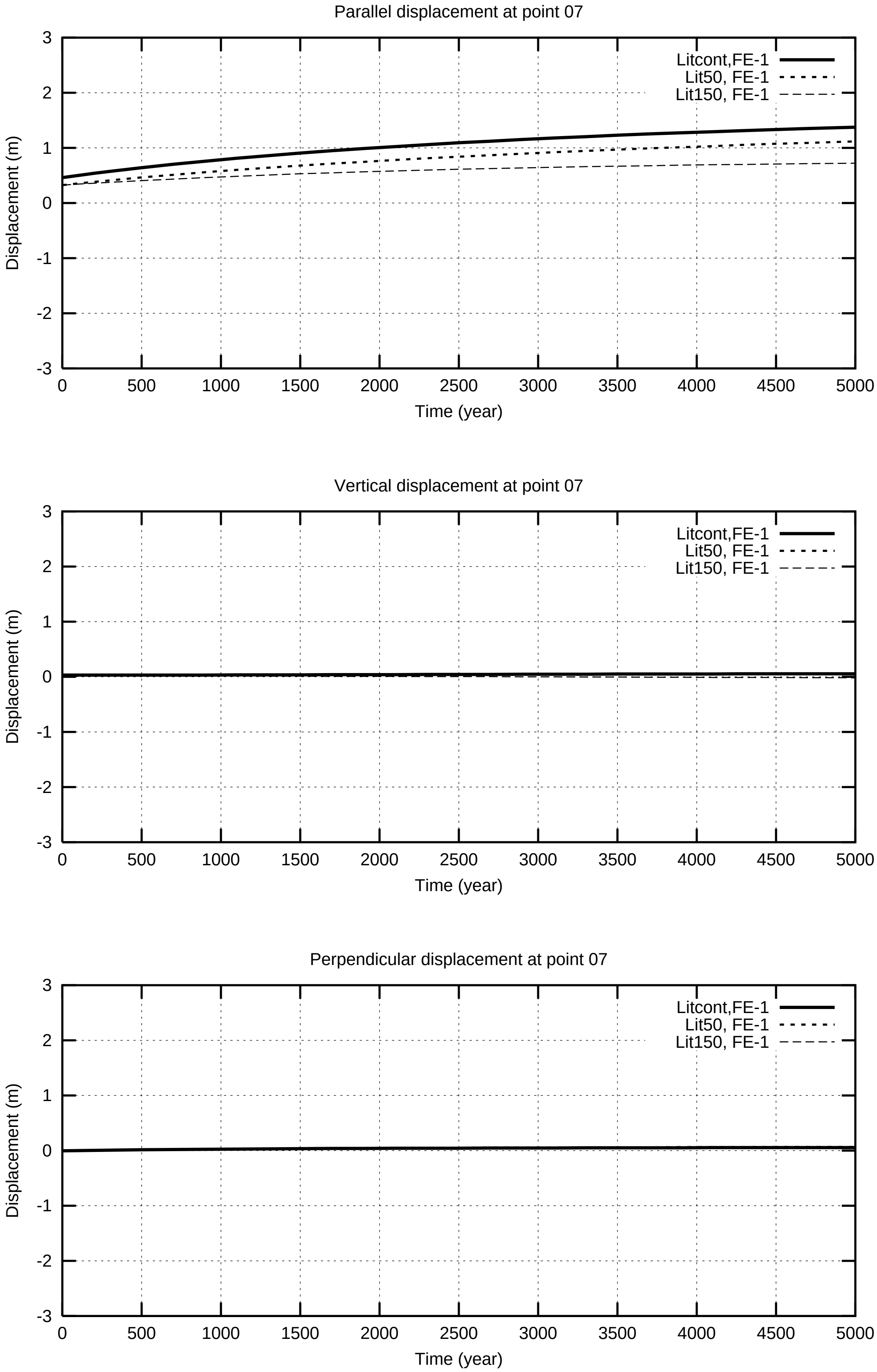

Figure 4.38: Temporal variations of displacement components at point 7 (figure 29) on the continental plate (Model D, Litcont), in radial models B and C (Lit50 and Lit150, 50 km and 150 km thick lithospheres, respectively) close to the fault

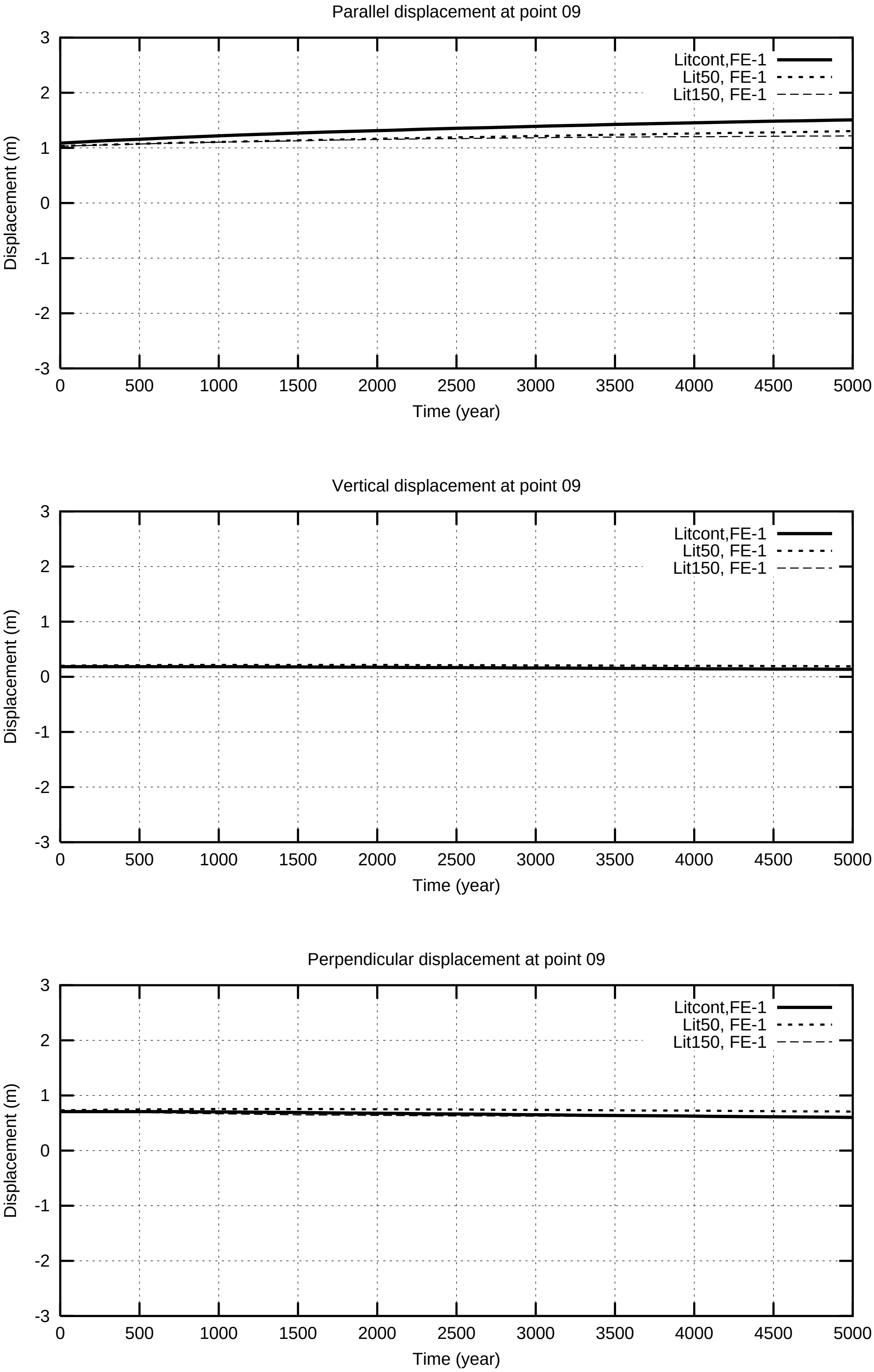

Figure 4.39: Temporal variations of displacement components at point 9 (figure 29) on the continental plate (Model D, Litcont), in radial models B and C (Lit50 and Lit150, 50 km and 150 km thick lithospheres, respectively) further from the fault

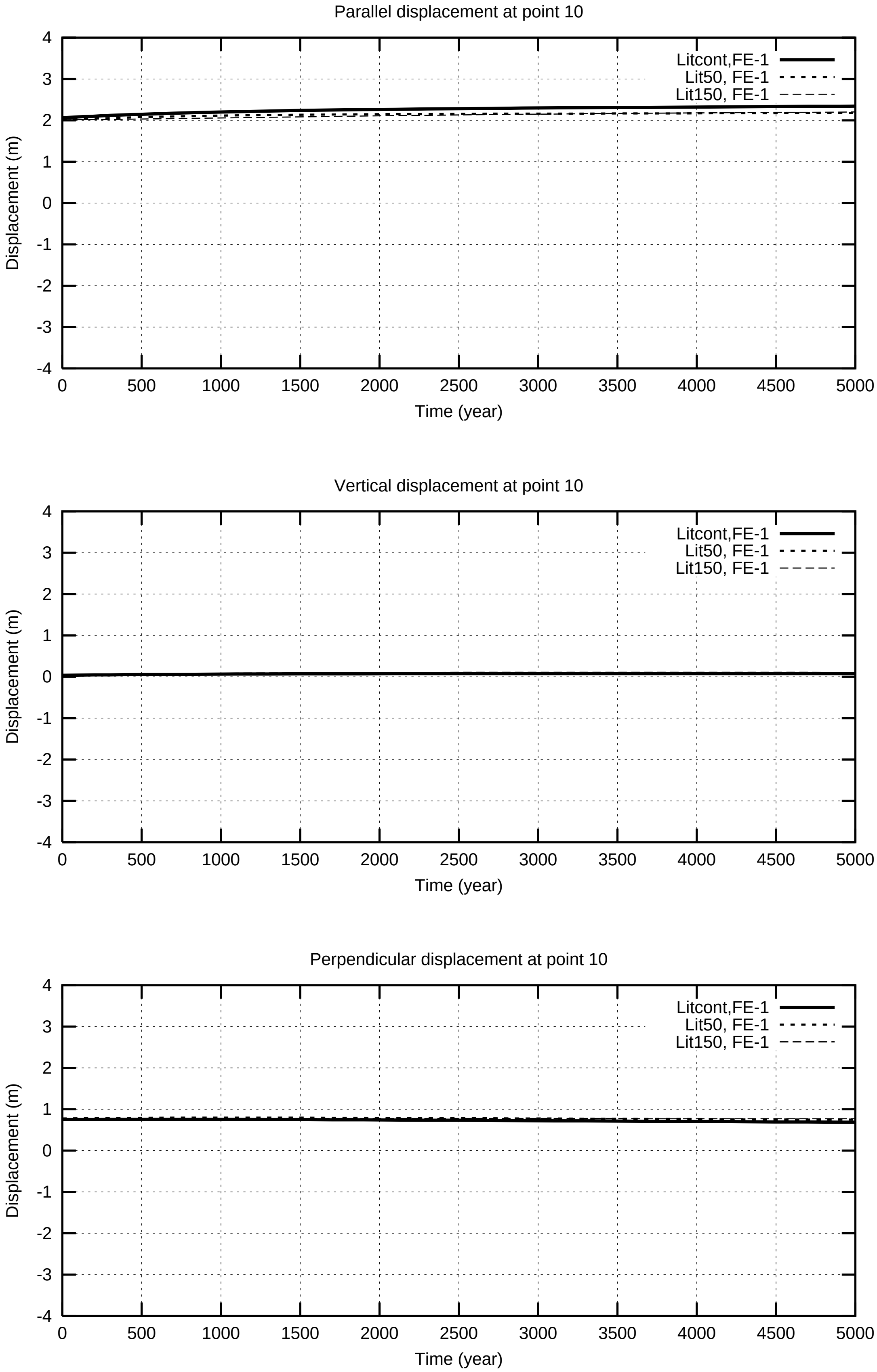

Figure 4.40: Temporal variations of displacement components at point 10 (figure 29) in the middle of the continental plate (Model D, Litcont), in radial models B and C (Lit50 and Lit150, 50 km and 150 km thick lithospheres, respectively)

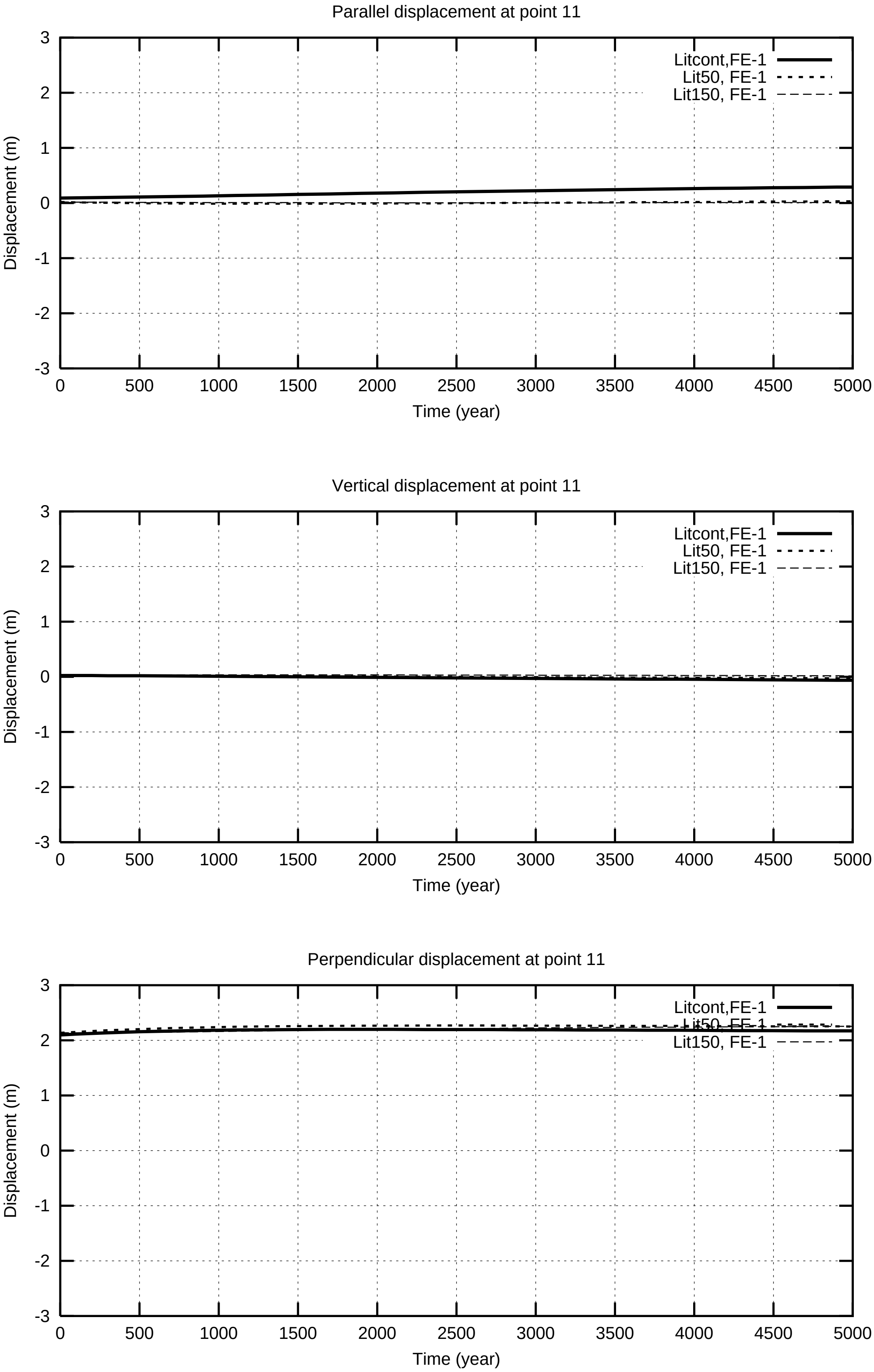

Figure 4.41: Temporal variations of displacement components at point 11 (figure 29) on the continental plate (Model D, Litcont), in radial models B and C (Lit50 and Lit150, 50 km and 150 km thick lithospheres, respectively) close to the fault

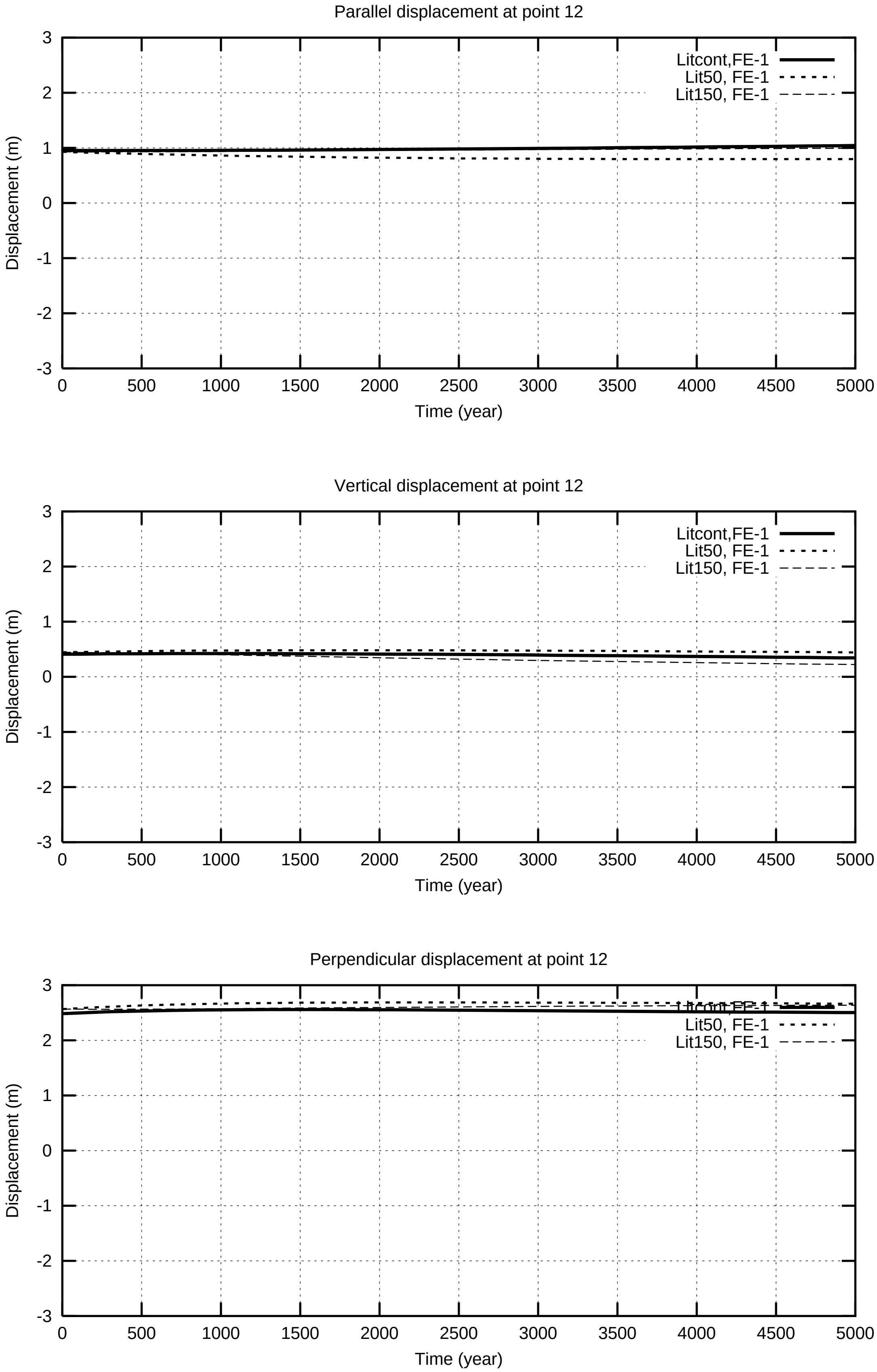

Figure 4.42: Temporal variations of displacement components at point 12 (figure 29) on the continental plate (Model D, Litcont), in radial models B and C (Lit50 and Lit150, 50 km and 150 km thick lithospheres, respectively) further from the fault

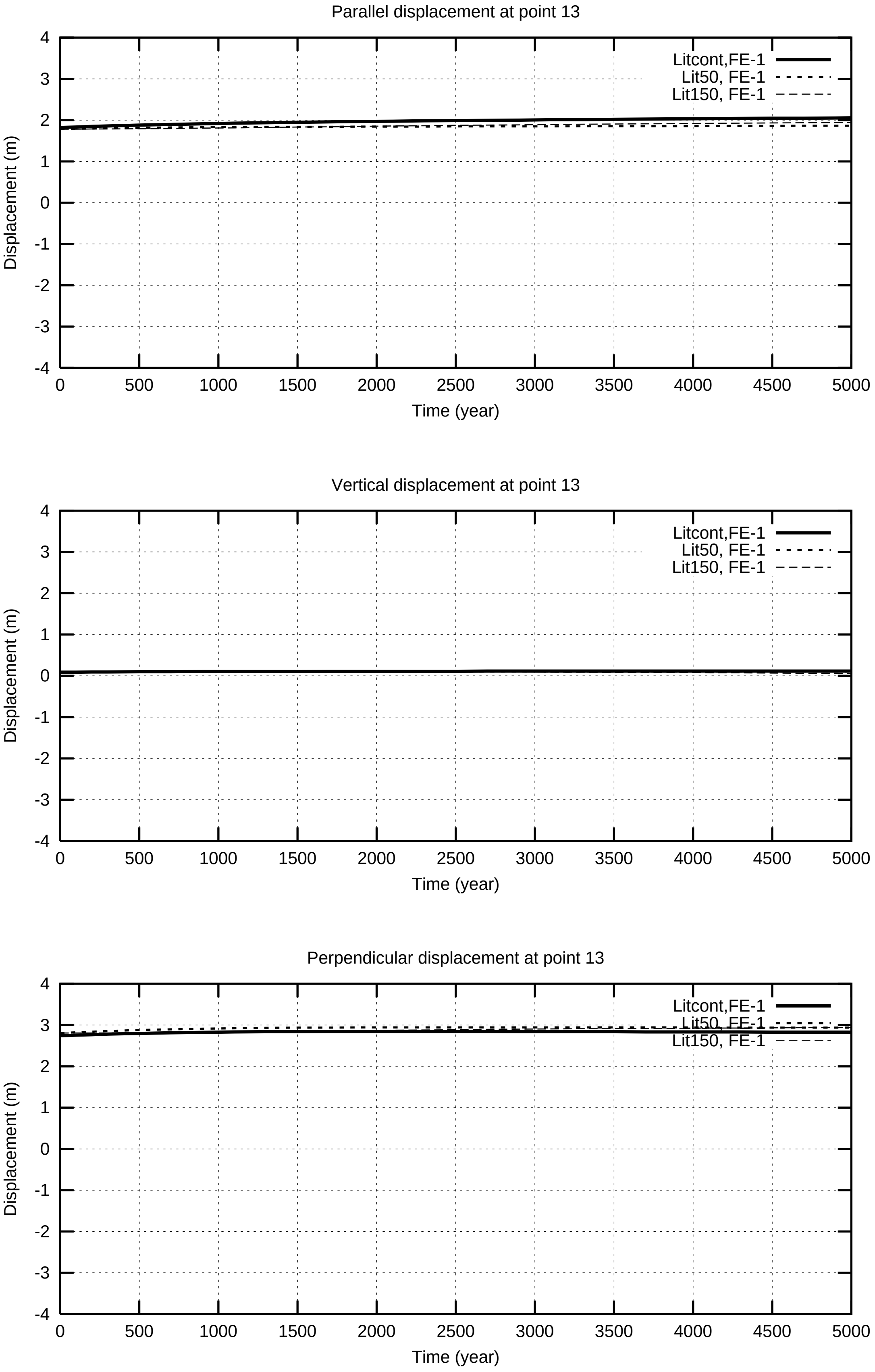

Figure 4.43: Temporal variations of displacement components at point 13 (figure 29) on the continental plate (Model D, Litcont), in radial models B and C (Lit50 and Lit150, 50 km and 150 km thick lithospheres, respectively)

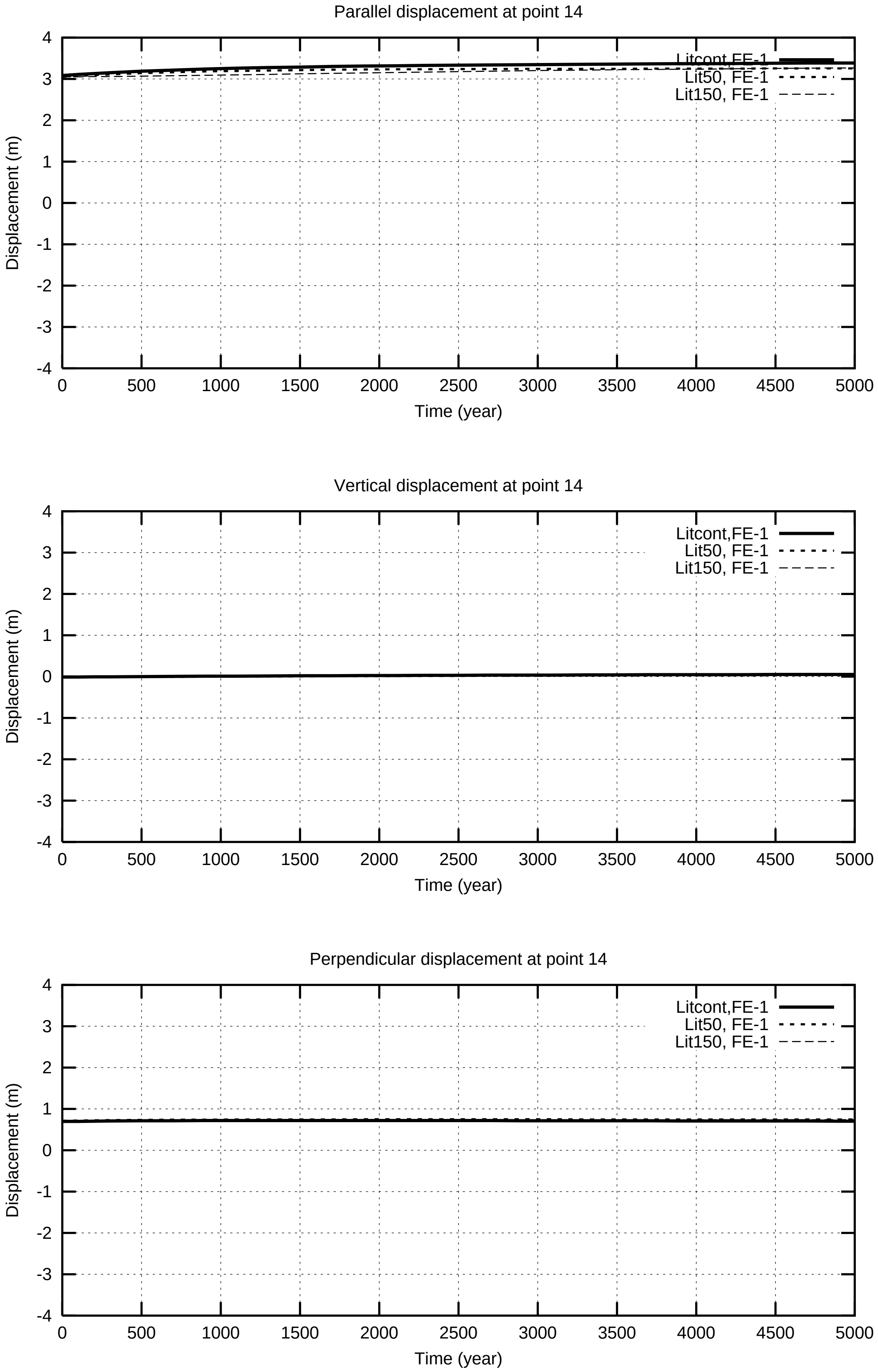

Figure 4.44: Temporal variations of displacement components at point 14 (figure 29) on the continental plate (Model D, Litcont), in radial models B and C (Lit50 and Lit150, 50 km and 150 km thick lithospheres, respectively)

4.3.4 Rigidity Profile

Model E (§3.3.5) allows us to study the effect of the rigidity profile. This model includes a homogeneous lithosphere and differs from model C (§3.3.3) only in the rigidity of the upper 50 km of the lithosphere.

Figure (4.45) represents the effect of the lithosphere on the three displacement components at point 5 (figure 4.1) for models C (Lit150) and E (Litr). The two horizontal components show that, as expected, the elastic response is smaller for the more rigid body, but the relaxation is not affected, at least in the time span of 5000 years. The vertical component may not be judged based on this model only, because of the reasons already discussed.

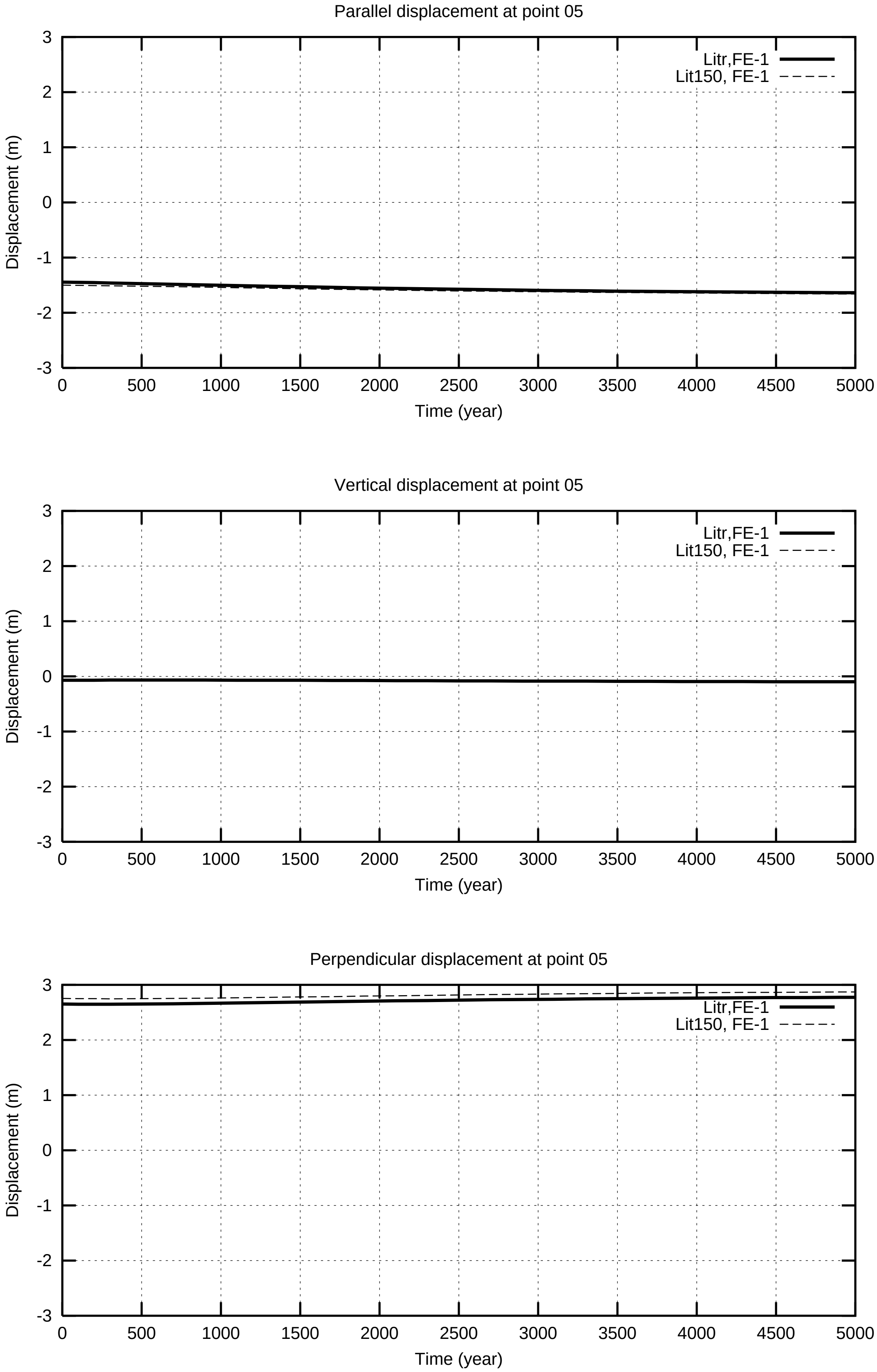

Figure 4.45: Displacement curves at point 5 (figure 4.1) in two models with 150 km thick lithosphere but different rigidity profiles (models C and E, §3.3.3 and §3.3.5)

Chapter 5

CONCLUSION AND FURTHER STUDIES

The displacement fields of different models were analyzed in chapter 4. Moreover in two cases, where the analytical solutions are well known, the analytical and numerical results were compared. This chapter presents conclusions and suggestion for further studies.

5.1 CONCLUSION

Consideration of the results of chapter 4 suggests the following:

- Figure (4.21) shows the importance of the self-gravitational pre-stress field in the analysis of the earth response to a surface load. The effect of pre-stresses may happen to be negligible for certain stress fields or in certain areas, but in general it is to be considered in order to get a realistic picture of the deformation field.

- From figure (4.14) it is concluded that the numerical technique nicely approximates the analytical solution of this model.

- The same conclusion can be drawn from figure (4.22) for the pre-stressed model. Worth noting is that this model does not completely include all the effect to be considered in a proper modeling of the response to surface loads, because the incremental gravitational field is not taken into account. Since the main purpose of the present work is to model a horizontal dislocation's deformation field, where the vertical field is not expected to play a decisive role, only those model specifications which are important for this purpose have been considered. Therefore although the analytical curves have been fairly good approximated by the numerical solutions, this method is not appropriate to apply to a load problem. For that purpose, the incremental gravitational field is to be modeled as well as the pre-stress field.

- Comparison of the figures (4.14 and 4.22) shows that there is better approximation in case of no pre-stress. This could be due to the elements' sizes, and it is expected that a the decrease of elements' sizes, a pre-stressed model leads to similar results as for the other model. Generally, the more effects are taken into account, the more refined the model must be.

- Figures (4.24 and 4.25) follow the expectations of a Maxwell viscoelastic material.

- There is no special problem in the definition of a multi-layered sphere, the number and the geometry of the elements are important.

- Defining internal displacement discontinuity is possible, but one has to be careful with it. In this work, the displacement values on the fault surface were prescribed, so that there is no material overlap and no cavity, before and after the fault slip. If one intends to leave the motion of the discontinuous area, or at some parts of it, the direct definition of a discontinuity surface, like a fault, may lead to unacceptable results. One proper solution could be to specify the source as a three dimensional continuous but low rigidity area instead of a discontinuous surface.

- Definition of lateral heterogeneity is no problem as long as the element definition can properly separate the areas of different material from each other. Practically, each element can be assigned to a separate material, and this makes the method rather powerful to model non-homogeneity.

- In addition to the lateral variations of viscosity, the effect of the rigidity profile was analyzed in the last step.

- The price to pay for the flexibility of the method to model discontinuities and heterogeneities is a proper attention to the numerical stability of the results. A finer grid of nodes and elements around the deformation source could help improve the stability of the solution.

5.2 SUGGESTION FOR FURTHER STUDIES

Clearly this work, like any other, does not end with an end point to this field of study and instead, again like any other research, opens new subjects. The following ideas might be a reasonable continuation of this work:

- Increase of the elements density in the near zone of the source in order to see its effects on the results, especially on their stability.

- A gradual increase of the number of layers and comparison of results.

- Consideration of *geodetically observed displacements, e.g. at permanent GPS points, as boundary conditions* can help a model reflect the reality more efficiently. They can play the role of a bridge from the pure model environment to the real earth. Kostrov and Das [1988, p. 32] believe that (compared to tiltmetry):

  > *Geodetic measurements, which are representative of larger areas, are a better means of studying tectonic strains.*

Appendix A

ELEMENTS OF ELASTICITY THEORY

This appendix briefly reviews some basic laws of elasticity such as Hooke's law. It starts with the simplest model, a rod in tension, and continues with generalization to a three dimensional linear elastic body. Various deformation measures, strain and stress tensors are defined, their meanings are described, and their relation is derived. The main types of elastic deformations are treated later by application of these laws.

A.1 HOOKE'S LAW FOR ROD IN TENSION

The fundamental equations of elasticity are based on Hooke's law, which states that the extension δl of an elastic bar is proportional to the applied force F (figure A.1):

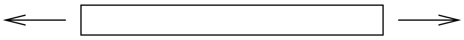

Figure A.1: A rod in tension

$$\delta l \sim F. \tag{A.1}$$

The relationship between the force F, the length l, the cross section S, and the extension δl of a bar is called *Hooke's law*:

$$\frac{F}{S} = E\frac{\delta l}{l}, \tag{A.2}$$

where the proportionality constant E is called *Young's modulus* and has the physical dimension of pressure.

Empirical results show that the same bar when extended in length is at the same time contracted in the transverse direction. The contraction δh and the extension δl are related by:

$$\frac{\delta h}{h} = -\gamma\frac{\delta l}{l} = -\frac{\gamma}{E}\frac{F}{S}\ , \tag{A.3}$$

in which the dimensionless proportionality constant γ is known as *Poisson's ratio.*

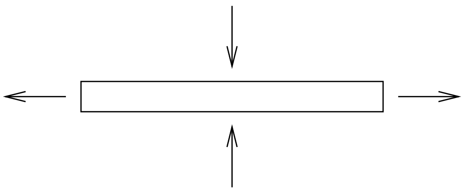

Figure A.2: Extension and contraction of a rod in tension

Hooke's law and eq. (A.3) constitute the basis for the linear elasticity theory of isotropic materials.

A.2 GENERAL CONTINUOUS MEDIUM

Tensor notation is the proper tool to generalize the case of a rod to a continuous three dimensional medium under the application of a force field instead of a simple force. The notation to write the equation of motion and to define various deformation measures for a generalized medium (figure A.3) is very different.

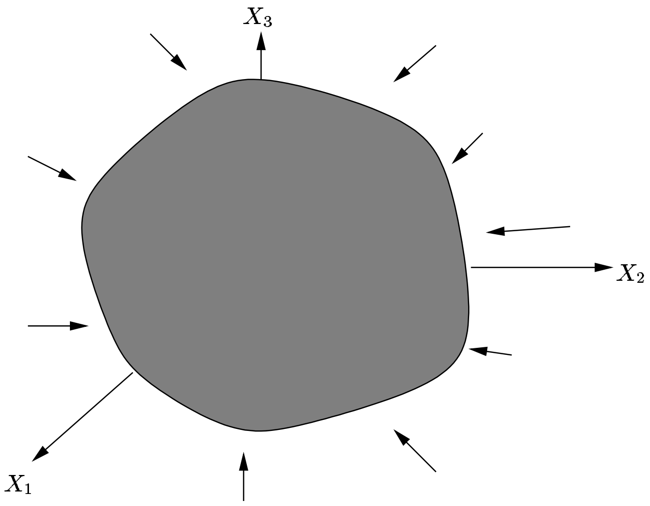

Figure A.3: A general three dimensional medium under a force field

A.2.1 Deformation Measures

Among different motions of a three dimensional medium, what is meant by *deformation* is the motion of its particles with respect to each other, i.e. rigid body translation (figure A.4) and rigid body rotation (figure A.5) are excluded from the present discussion. The parameters which quantify this deformation are known as *deformation measures,* two of them are defined in the following.

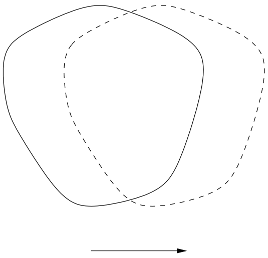

Figure A.4: Rigid body translation

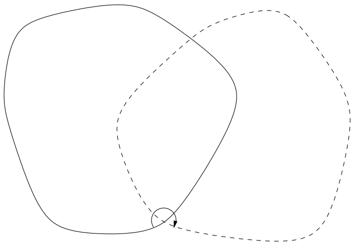

Figure A.5: Rigid body rotation

Consider two points of a body in an infinitesimal neighborhood. We show their coordinates by capital and small letters before and after the deformation, respectively. The points are separated by the vectors $d\boldsymbol{X}$ and $d\boldsymbol{x}$ at the two epochs, when their distances are dS and ds (figure A.6), respectively.

Applying the summation convention in the Cartesian representation of the coordinates yields:

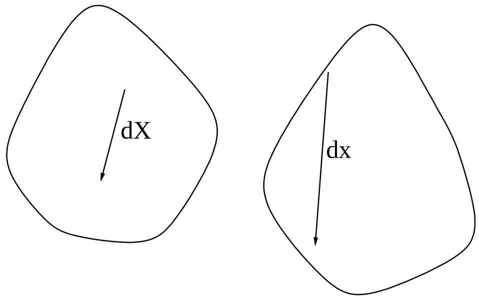

(a) (b)

Figure A.6: The separation vector (a) before and (b) after the deformation

$$
\begin{aligned}
dS^2 &= dX^K dX^K \ , &\text{(A.4)}\\
ds^2 &= dx^k dx^k \ . &\text{(A.5)}
\end{aligned}
$$

The distance before the deformation can be derived in terms of the deformed coordinates:

$$dX^K = \frac{\partial X^K}{\partial x^k} dx^k \tag{A.6}$$

or vice versa:

$$dx^k = \frac{\partial x^k}{\partial X^K} dX^K . \tag{A.7}$$

Then

$$
\begin{aligned}
dS^2 &= \frac{\partial X^K}{\partial x^k}\frac{\partial X^K}{\partial x^l} dx^k dx^l &\text{(A.8)}\\
&= C_{kl} dx^k dx^l &\text{(A.9)}
\end{aligned}
$$

and

$$
\begin{aligned}
ds^2 &= \frac{\partial x^k}{\partial X^K}\frac{\partial x^k}{\partial X^L} dX^K dx^L ds^2 &\text{(A.10)}\\
&= c_{KL} dX^K dX^L \ , &\text{(A.11)}
\end{aligned}
$$

where C_{kl} and c_{KL} are the coefficients of *Cauchy's deformation tensor* and *Green's deformation tensor:*

$$
\begin{aligned}
C_{kl} &:= \frac{\partial X^K}{\partial x^k}\frac{\partial X^K}{\partial x^l} \ , &\text{(A.12)}\\
c_{KL} &:= \frac{\partial x^k}{\partial X^K}\frac{\partial x^k}{\partial X^L} \ . &\text{(A.13)}
\end{aligned}
$$

The change of the squared differential length is another *deformation measure*:

$$\boxed{ds^2 - dS^2 = 2\epsilon_{KL}(\boldsymbol{X}, t) dX^K dX^L} \tag{A.14}$$

or

$$\boxed{ds^2 - dS^2 = 2E_{kl}(\boldsymbol{x}, t) dx^k dx^l} \tag{A.15}$$

where

$$
\begin{aligned}
e_{KL} &:= \frac{1}{2}(c_{KL}(\boldsymbol{X}, t) - \delta_{KL}) \ , &\text{(A.16)}\\
E_{kl} &:= \frac{1}{2}(\delta_{kl} - C_{kl}(\boldsymbol{x}, t)) &\text{(A.17)}
\end{aligned}
$$

are the coefficients of the *Lagrangian strain tensor* and the *Eulerian strain tensor,* respectively. δ_{ij} is the Kronecker delta, for $i = j$ $\delta_{ij} = 1$, otherwise $\delta_{ij} = 0$.

A.2.2 Strain Tensor

For an arbitrary point of the deformation medium, e.g. i, we define the displacement vector as:

$$\boldsymbol{U}_i = \boldsymbol{x}_i - \boldsymbol{X}_i \ . \tag{A.18}$$

Then, for any neighboring points, e.g. $\boldsymbol{X}_1$ and $\boldsymbol{X}_2$ (figure A.7), separated by the separation vector $d\boldsymbol{X}$:

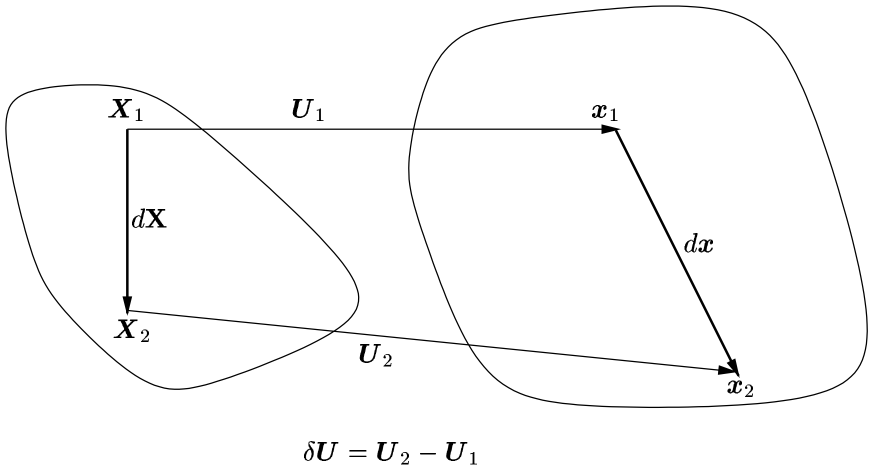

Figure A.7: Two neighboring points in a deforming medium

$$\delta\boldsymbol{X} = \boldsymbol{X}_2 - \boldsymbol{X}_1 \tag{A.19}$$

we have:

$$\boldsymbol{U}_1 = \boldsymbol{x}_1 - \boldsymbol{X}_1 \tag{A.20}$$

and

$$\boldsymbol{U}_2 = \boldsymbol{x}_2 - \boldsymbol{X}_2 \ , \tag{A.21}$$

and the the differential displacement is defined as:

$$\delta\boldsymbol{U} = \boldsymbol{U}_2 - \boldsymbol{U}_1 \ . \tag{A.22}$$

Series expansion and neglect of the terms of second and higher orders leads to

$$\begin{aligned} \delta\boldsymbol{U} &\simeq [(\boldsymbol{X}_2 - \boldsymbol{X}_1).\nabla]\boldsymbol{U} && \text{(A.23)} \\ &= (\delta\boldsymbol{X}.\nabla)\boldsymbol{U} \ , && \text{(A.24)} \end{aligned}$$

where

$$(\delta\boldsymbol{X}.\nabla)\boldsymbol{U} = (\delta\boldsymbol{X}.\nabla U_1, \delta\boldsymbol{X}.\nabla U_2, \delta\boldsymbol{X}.\nabla U_3) \tag{A.25}$$

or in indicial notation:

$$\delta U^i = \frac{\partial U^i}{\partial X^j}\delta X^j. \tag{A.26}$$

Since

$$[(\nabla \times \boldsymbol{U}) \times \delta\boldsymbol{X}]^i = (\frac{\partial U^i}{\partial X^j} - \frac{\partial U^j}{\partial X^i})\delta X^j \ , \tag{A.27}$$

where $\nabla\times$ is the curl operator, we can rewrite the eq. (A.26) as:

$$\begin{aligned} \delta U^i &= \frac{1}{2}\left(\frac{\partial U^i}{\partial X^j} + \frac{\partial U^j}{\partial X^i}\right)\delta X^j + \frac{1}{2}\left(\frac{\partial U^i}{\partial X^j} - \frac{\partial U^j}{\partial X^i}\right)\delta X^j && \text{(A.28)} \\ &= \frac{1}{2}\left(\frac{\partial U^i}{\partial X^j} + \frac{\partial U^j}{\partial X^i}\right)\delta X^j + \frac{1}{2}[(\nabla \times \boldsymbol{U}) \times \boldsymbol{X}] \ . && \text{(A.29)} \end{aligned}$$

The two right hand terms of the last equation:

$$\boxed{\boldsymbol{E} := \frac{1}{2}\left(\frac{\partial U^i}{\partial X^j} + \frac{\partial U^j}{\partial X^i}\right)(\boldsymbol{e}_i \otimes \boldsymbol{e}_j)} \tag{A.30}$$

where $\otimes$ shows the tensor product, and

$$\boxed{\boldsymbol{R} := \frac{1}{2}(\nabla \times \boldsymbol{U})} \tag{A.31}$$

are called *(infinitesimal) strain tensor* and *rigid body rotation* because of their geometrical meanings.

A.2.3 Geometrical Meanings of Strain Tensor Elements

Strain tensor elements convey helpful concepts, as follows.

A.2.3.1 Strain

The length of the infinitesimal segment after the deformation is computed by:

$$ds = (\delta\boldsymbol{X}.\delta\boldsymbol{X} + 2\delta\boldsymbol{U}.\delta\boldsymbol{X})^{\frac{1}{2}} \ . \tag{A.32}$$

Since $\delta\mathbf{U}.\delta\mathbf{U} \simeq 0$, it follows:

$$\begin{aligned} ds &= (\delta X^i \delta X^i + 2\delta U^i \delta X^i)^{\frac{1}{2}} && \text{(A.33)}\\ &= \left\{\delta X^i \delta X^i + \left[\left(\frac{\partial U^i}{\partial X^j} + \frac{\partial U^j}{\partial X^i}\right)\delta X^j \delta X^i + \left[(\nabla \times \boldsymbol{U}) \times \delta X\right]^i \delta X^i\right]\right\}^{\frac{1}{2}} . && \text{(A.34)}\end{aligned}$$

With

$$\left[(\nabla \times \boldsymbol{U}) \times \delta\boldsymbol{X}\right]^i \delta X^i = 0 \ , \tag{A.35}$$

we have

$$\begin{aligned} ds &= \left(\delta X^i \delta X^i + 2E_{ij}\delta X^i \delta X^j\right)^{\frac{1}{2}} && \text{(A.36)}\\ &\simeq dS\left(1 + E_{ij}N^i N^j\right) \ , && \text{(A.37)}\end{aligned}$$

where:

$$\boldsymbol{N} = \frac{\delta\boldsymbol{X}}{|\boldsymbol{X}|} \ . \tag{A.38}$$

Therefore:

$$\frac{ds}{dS} = 1 + E_{ij}N^i N^j. \tag{A.39}$$

This equation shows that the extensional strain of the line segment in the direction N is equal to $E_{ij}N^i N^j$.

In this way, the stretch $\frac{ds}{dS}$ in the coordinate directions is obtained as:

$$\left(\frac{ds}{dS}\right)_i = 1 + E_{ii} \text{ (no summation convention)}, \tag{A.40}$$

which shows that the diagonal elements of the strain tensor define stretches along the coordinate lines.

A.2.3.2 Volume Change

The relative volume change can be computed from the relative length changes of the sides of a cube along the three axes of a local Cartesian coordinate system (figure A.8). The side changes are:

$$\left(\frac{ds}{dS}\right)_i = 1 + E_{ii} \text{ (no summation convention)}, \tag{A.41}$$

With V and v the volumes before and after the deformation, it follows:

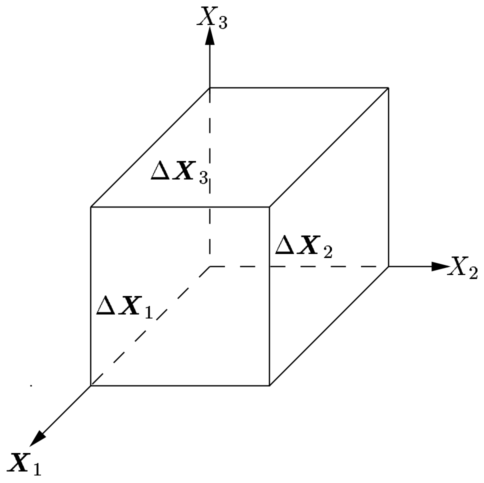

Figure A.8: Small cube along the local Cartesian coordinate system

$$V = dS^1 dS^2 dS^3 \tag{A.42}$$

$$v = ds^1 ds^2 ds^3 \tag{A.43}$$

$$= dS^1 dS^2 dS^3 \left(1 + E_{11}\right)\left(1 + E_{22}\right)\left(1 + E_{33}\right) \tag{A.44}$$

$$\simeq dS^1 dS^2 dS^3 \left(1 + E_{ii}\right). \tag{A.45}$$

The relative volume change is thus:

$$E_{ii} \simeq \frac{v - V}{V}. \tag{A.46}$$

A.2.3.3 Non-diagonal Terms

Consider again the cube of figure A.8, assuming that the $OABC$ side lying on the $X_1 X_2$ plane is deformed to $O'A'B'C'$ (figure A.9). Then:

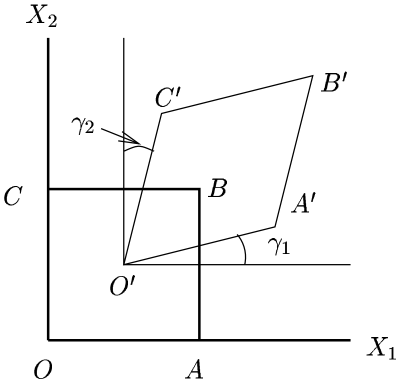

Figure A.9: Horizontal section of the deformed cube along the local Cartesian coordinate system

$$\gamma_1 \simeq \tan \gamma_1 \tag{A.47}$$

$$\simeq \frac{\partial U^2}{\partial X^1}, \tag{A.48}$$

$$\gamma_2 \simeq \tan \gamma_2 \tag{A.49}$$

$$\begin{aligned} &\simeq \frac{\partial U^1}{\partial X^2}\ , && \text{(A.50)} \\ 2E_{12} &= \frac{\partial U^1}{\partial X^2} + \frac{\partial U^2}{\partial X^1} && \text{(A.51)} \\ &= E_{12} + E_{21}\ . && \text{(A.52)} \end{aligned}$$

This shows that the symmetric non-diagonal terms of the strain tensor define the angular distortions. They are known as *shear strains.*

A.2.4 Stress Tensor

The action of an external force field causes stresses in the deforming body. The state of stress at each point is represented by the stress tensor defined as follows.

Let us go back to the small cube along the Cartesian coordinate axes $X_1,\ X_2,\ X_3$. Consider areas:

$$\begin{aligned} \Delta S_1 &= \Delta X_2 \Delta X_3\ , && \text{(A.53)} \\ \Delta S_2 &= \Delta X_1 \Delta X_3\ , && \text{(A.54)} \\ \Delta S_3 &= \Delta X_1 \Delta X_2 && \text{(A.55)} \end{aligned}$$

(figure A.10) small enough that the force ΔF_i acting on ΔS^i can be considered proportional to the associated area. If we denote the components of $\Delta \boldsymbol{F}_i$ by ΔF_i^k, we can introduce the quantities:

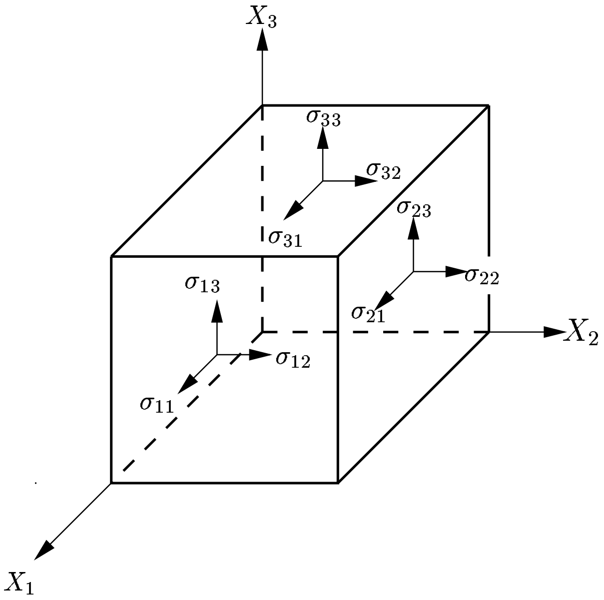

Figure A.10: Stress tensor elements

$$\boxed{\sigma_{ik} = \frac{\Delta F_i^k}{\Delta S_i}\ .} \tag{A.56}$$

The nine quantities $\sigma_{ik},\ i,k = 1,2,3$ completely define the state of stress at the origin of the coordinate system $X_1X_2X_3$, and are known as *stress tensor.* The following symmetry (Aki and Richards [1980]) reduces the number of independent elements of the stress tensor to six:

$$\sigma_{ik} = \sigma_{ki}. \tag{A.57}$$

Given the stress tensor at an arbitrary point, the surface force at this point can be computed with respect to any surface:

$$f_i = \sigma_{ki} n_k. \tag{A.58}$$

(See any textbook in elasticity theory, e.g. Eringen [1980])

A.2.5 Stress-Strain Relation

In an *elastic medium*, a medium in which strains vanish when stresses are removed sufficiently slowly, the stress is always proportional to strain. When the stresses are removed abruptly, oscillations can arise in the medium [BRECHKOVSKI and GONCHAROV, 1994]. An important characteristic of the medium is the relation between stress and strain, which is known as *constitutive relation.*

There are different constitutive relations for different types of materials. *Linear elastic* bodies are those materials whose constitutive relation is a generalization of Hooke's law, i.e. each component of the stress tensor is a linear combination of the components of the strain tensor:

$$\boxed{\sigma_{ij} = c_{ijpq} e_{pq}\ .} \tag{A.59}$$

The quantities c_{ijpq} are components of a fourth order tensor who has the symmetries [AKI and ROCHARDS, 1980]:

$$c_{jipq} = c_{ijpq} \tag{A.60}$$

$$c_{ijqp} = c_{ijpq} \tag{A.61}$$

and

$$c_{pqij} = c_{ijpq} \tag{A.62}$$

The symmetries reduce the number of independent components (elastic moduli) from 81 to 27 [MASE, 1970].

Elastic moduli do not vary with strains, they are generally functions of position and the coordinate system in the used. In the special case where they don't vary with the coordinate system (*isotropic medium)*, the constitutive relation is highly simplified. The independent elastic moduli are reduced to *Lame constants* λ and μ:

$$c_{ijkl} = \lambda \delta_{ij} \delta_{kl} + \mu(\delta_{ik}\delta_{jl} + \delta_{il}\delta_{jk}) \tag{A.63}$$

The results are valid for small deformations from a reference state, which refers to the state of no stress. This can't be applied to cases like earth's interior where pressures of 1 Mbar are expected. For this reason we can refer the reference state to a presumed stress, e.g. $\boldsymbol{\sigma}_0$, then investigate the relation between strain and incremental stresses, e.g. $\Delta\boldsymbol{\sigma}$, the relation is again as before:

$$\Delta\sigma_{ij} = c_{ijkl} e_{kl} \tag{A.64}$$

Alternative to Lame constants, the material behaviour can be specified by Young's modulus and Poisson's ratio. The two sets of quantities are interrelated by:

$$\begin{aligned} \lambda &= \frac{E\nu}{(1+\nu)(1-2\nu)} \\ \mu &= \frac{E}{2(1+\nu)} \end{aligned} \quad , \tag{A.65}$$

or

$$\begin{aligned} E &= \mu \frac{3\lambda + 2\mu}{\lambda + \mu} \\ \nu &= \frac{\lambda}{2(\lambda+\mu)} \end{aligned} \quad . \tag{A.66}$$

A.3 EQUATION OF MOTION

In the displacement field $\boldsymbol{U}$ of the body V bounded by the surface S (figure A.11), there is a constraint on the accelerations, body forces and tractions. By setting equal the rate of change of momentum of the particles in V to the acting forces:

$$\frac{\partial}{\partial t}\int\!\!\int\!\!\int_V \rho \frac{\partial \boldsymbol{u}}{\partial t} dV = \int\!\!\int\!\!\int_V \boldsymbol{f} dV + \int\!\!\int_S \boldsymbol{T}(\boldsymbol{n}) dS \tag{A.67}$$

or in index notation

$$\frac{\partial}{\partial t}\int\!\!\int\!\!\int_V \rho \frac{\partial u^i}{\partial t} dV = \int\!\!\int\!\!\int_V f_i dV + \int\!\!\int_S T_i(\boldsymbol{n}) dS \tag{A.68}$$

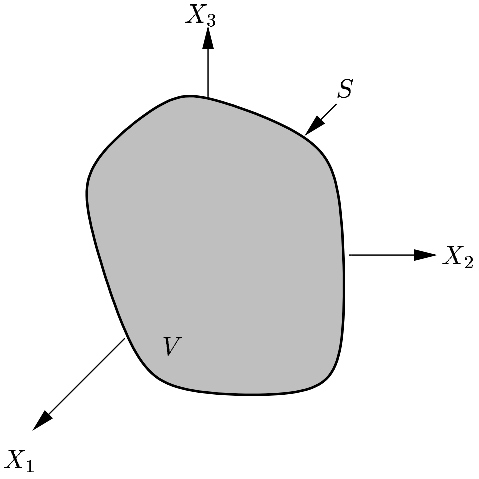

Figure A.11: Current volume V, bounded by the current surface S

where V is the current volume and S the current surface.

Note that using the Lagrangian approach, i.e. expressing the space time dependent functions as functions of the reference position $\boldsymbol{X}$ and time t, the argument $\boldsymbol{X}$, e.g. in $\boldsymbol{U}(\boldsymbol{X},t)$ is a fixed position and not a function of time, therefore $\frac{\partial}{\partial t}$ in the above equation can be replaced by $\frac{d}{dt}$:

$$\frac{\partial \boldsymbol{u}(\boldsymbol{X},t)}{\partial t} = \frac{d\boldsymbol{u}(\boldsymbol{X},t)}{dt}, \tag{A.69}$$

and

$$\frac{\partial \rho(\boldsymbol{X},t)}{\partial t} = \frac{d\rho(\boldsymbol{X},t)}{dt}. \tag{A.70}$$

Moreover although the volume elements are deformed, their masses are constant in the Lagrangian approach:

$$\frac{\partial}{\partial t}(\rho dV) = 0. \tag{A.71}$$

Therefore:

$$\frac{\partial}{\partial t}\int\int\int_V \rho\frac{\partial \boldsymbol{u}}{\partial t}dV = \int\int\int_V \rho\frac{d^2\boldsymbol{u}}{dt^2}dV. \tag{A.72}$$

Applying the Gauss theorem:

$$\int\int\int_v \nabla.\boldsymbol{u}dV = \int\int_S \boldsymbol{u}.d\boldsymbol{S}\ , \tag{A.73}$$

where $d\boldsymbol{S}$ is the normal outward vector to the surface element $\boldsymbol{S}$ with a magnitude equal to the area of the surface element dS, and the dot denotes the inner product of the two vectors. In index notation we can write:

$$\int\int\int_V u^i_{,i}dV = \int\int_S u^i n_i dS \tag{A.74}$$

where we used the abbreviation $\frac{\partial u^i}{\partial X_j} = u^i_{,j}$. By eq. (A.58):

$$T_i = \sigma_{ji}n_j \tag{A.75}$$

where $\boldsymbol{T}$ =Traction vector, $\boldsymbol{\sigma}$ =stress tensor and $\boldsymbol{n}$ =unit normal vector. One concludes that :

$$\int\int_S T_i dS = \int\int_S \sigma_{ji}n_j dS = \int\int\int_V \sigma_{ji,j}dV, \tag{A.76}$$

then

$$\int\int\int_V (\rho\ddot{u}_i - f_i - \sigma_{ji,j})dV = 0. \tag{A.77}$$

This equation is valid for any partial body of a continuous material, therefore:

$$\boxed{\rho \ddot{u}_i = f_i + \sigma_{ji,j}\ .} \tag{A.78}$$

This is one of the several forms of the equation of motion.

In the initial state, i.e. before the deformation, the medium is assumed to be at rest, therefore we can write:

$$0 = f_i + \sigma_{0ji,j}. \tag{A.79}$$

In the pre-stressed form of eq. (A.64), one term is added to the eq. (A.67) and eq. (A.68):

$$\frac{\partial}{\partial t} \int\int\int_V \rho \frac{\partial u_i}{\partial t} dV = \int\int\int_V f_i dV + \int\int_S T_i(\boldsymbol{n}) dS + \int\int_S \Delta\sigma_{ji} n_j dS\ . \tag{A.80}$$

Following the same principles:

$$\boxed{\rho \ddot{u}_i = f_i + \sigma_{0ji,j} + \Delta\sigma_{ji,j}\ .} \tag{A.81}$$

One has to be careful in the applications of the last equation, since here $\Delta\sigma_{ji,j}$ is in the deforming coordinates. By transforming it into the initial coordinates:

$$\sigma_{0_{ji,i}} = \frac{\partial \sigma_{0ji}}{\partial X_K} \frac{\partial X_K}{\partial x_i}. \tag{A.82}$$

With:

$$u^K = x^K - X^K, \tag{A.83}$$

we have:

$$\begin{aligned}
\sigma_{0ji,j} &= \frac{\partial \sigma_{0ji}}{\partial X^K} \left(\frac{\partial x^K}{\partial x^i} - \frac{\partial u^K}{\partial x^i} \right) && \text{(A.84)} \\
&= \frac{\partial \sigma_{0ji}}{\partial X^K} \left(\delta_{iK} - \frac{\partial u^K}{\partial X^L} \frac{\partial X^L}{\partial x^i} \right) && \text{(A.85)} \\
&= \frac{\partial \sigma_{0ji}}{\partial X^K} \left[\delta_{iK} - \frac{\partial u^K}{\partial X^L} \left(\frac{\partial x^L}{\partial x^i} - \frac{\partial u^L}{\partial x^i} \right) \right] && \text{(A.86)} \\
&= \frac{\partial \sigma_{0ji}}{\partial X^K} \left(\delta_{iK} - \frac{\partial u^K}{\partial X^L} \delta_i^L + \frac{\partial u^K}{\partial X^L} \frac{\partial u^L}{\partial x^i} \right) && \text{(A.87)} \\
&= \frac{\partial \sigma_{0ji}}{\partial X^K} \left(\delta_{iK} - \frac{\partial u^K}{\partial X^L} \delta_i^L + O^2 \right). && \text{(A.88)}
\end{aligned}$$

A.3.1 Reynold's Transport Theorem

Reynold's Transport Theorem states an important property of the variations in a continuum. To understand this theorem, we need the following definitions and relations.

1. *Material Derivative*: When a property of a continuum is formulated by a scalar $P(\boldsymbol{x}, t)$ which can also be a component of a vector or a matrix, and if $\mathbf{x}$ is itself a function of time, $\boldsymbol{x}\,(\boldsymbol{X}, t)$, we have:

$$\frac{dP}{dt} = \frac{\partial P}{\partial t} + \frac{\partial P}{\partial x_p} \frac{dx_p}{dt} = \frac{\partial P}{\partial t} + v_p \frac{\partial P}{\partial x_p} = \frac{\partial P}{\partial t} + \boldsymbol{v}.\nabla_x P. \tag{A.89}$$

2. When

$$dV = dX^1 dX^2 dX^3, \tag{A.90}$$

$$dv = dx^1 dx^2 dx^3\ , \tag{A.91}$$

then

$$dv = J dV\ , \tag{A.92}$$

where

$$J = \epsilon_{ijk} \frac{\partial x_i}{\partial X_1} \frac{\partial x_j}{\partial X_2} \frac{\partial x_k}{\partial X_3}, \tag{A.93}$$

where ϵ_{ijk} is the permutation symbol defines as:

$$\epsilon_{123} = \epsilon_{231} = \epsilon_{312} = -\epsilon_{132} = -\epsilon_{213} = -\epsilon_{321} = 1$$

and

$$\epsilon_{ijk} = 0 \text{ otherwise}$$

3. In the Eulerian description, i.e. writing the equations in the deforming coordinate system $\mathbf{x}$, the volume element dv is a function of position and time, and

$$\frac{d}{dt}(dv) = \frac{d}{dt}(JdV). \tag{A.94}$$

Since dV, the volume element before the deformation, does not depend on time:

$$\frac{d}{dt}(dv) = \frac{dJ}{dt}dV, \tag{A.95}$$

with $\frac{dJ}{dt} = J\frac{\partial v_i}{\partial x_i}$ [MASE, 1970]:

$$\frac{d}{dt}(dv) = J\frac{\partial v_i}{\partial x_i}dV = \frac{\partial v_i}{\partial x_i}dv = \nabla\mathbf{v}dv. \tag{A.96}$$

Note that $\mathbf{v}$ is the velocity vector, while dv is the volume element in the deforming coordinate system.

4. In time derivatives of volume integrals in Eulerian formulation, one should not forget that dv is a function of time, therefore :

$$\frac{d}{dt}\int\int\int_v P(\boldsymbol{x},t)dv = \int\int\int_v \frac{d}{dt}(Pdv) = \int\int\int_v \left[\frac{dP}{dt}dv + P\frac{d}{dt}(dv)\right]. \tag{A.97}$$

Since v is a definite portion of the continuum, the integration and differentiation are interchangeable. Applying material derivatives and $\frac{d}{dt}dv$:

$$\begin{aligned}\frac{d}{dt}\int\int\int_v P(\boldsymbol{x},t)dv &= \int\int\int_v \left[\left(\frac{\partial P}{\partial t} + v_p\frac{\partial P}{\partial x_p}\right)dv + P\frac{\partial v_p}{\partial x_p}dv\right] \\ &= \int\int\int_v \frac{\partial P}{\partial t}dv + \int\int\int_v \left[vp\frac{\partial P}{\partial x_p} + \frac{\partial v_p}{\partial x_p}P\right]dv \\ &= \int\int\int_v \frac{\partial P}{\partial t}dv + \int\int\int_v \frac{\partial}{\partial x_p}(v_pP)dv\ .\end{aligned} \tag{A.98}$$

Applying Gauss theorem:

$$\boxed{\frac{d}{dt}\int\int\int_v P(\boldsymbol{x},t)dv = \int\int\int_v \frac{\partial P}{\partial t}dv + \int\int_s v_pn_pds\ .} \tag{A.99}$$

This equation is known as *Reynold's transport theorem* and states that the rate of increase of the property P in a continuum occupying the volume v is equal to the sum of the amount of the property created within v plus the flux of the property through the surface s of v.

Appendix B

DESCRIPTION OF BODY FORCES

B.1 INTRODUCTION

There are basically two different categories of seismic sources, classified as *external* and *internal* [AKI and RICHARDS, 1980]. External sources are located on the earth's surface and are usually modeled as time varying tractions applied to the earth's surface. Some examples are meteorite impacts, rocket launching and ocean waves. Internal sources, such as earthquakes and underground explosions, are located inside the earth. We will deal with internal sources in this chapter.

Internal sources are more difficult to treat analytically because the source functions are more complicated. Internal sources my be subdivided into two parts:

- faulting sources,
- volume sources,

which are events associated with internal surfaces and internal volumes, respectively. Slip across a fracture plane is an example of a faulting source, and sudden expansion (explosion) of a three dimensional internal region may be taken as an example of a volume source.

The main aim of this chapter is to represent the displacement field of a seismic source, i.e. to obtain a formula for the displacement at an arbitrary point in space and time in terms of quantities related to the source. In most cases, e.g. earthquake faulting, the seismic source extends over a finite fault plane (or volume) and over a finite time interval and involves motions in different directions and magnitudes near the source. Therefore the seismic source is too complicated to be represented by one formula, but there are some solution techniques to handle this problem.

In one of the techniques discussed in this chapter a discontinuous source modeled as a traction or displacement discontinuity is replaced by an equivalent body force, i.e. a non-existing body force which could produce the same displacement field outside the source region.

B.2 FUNDAMENTALS

The technique is based on Betti's theorem, as follows [AKI and RICHARDS, 1980].

B.2.1 Betti's Theorem

Suppose that there are two sources of displacement in one medium:

1. Body force field $\boldsymbol{F}(\boldsymbol{x}, t)$:
   $\boldsymbol{F}(\boldsymbol{x}, t)$: the body force acting per unit volume on the particle at position $\boldsymbol{x}$ at time t,
   $\boldsymbol{T}^{(\boldsymbol{U})}(\boldsymbol{n})$: the traction on the surface designated by its unit normal vector $\boldsymbol{n}$,
   $\boldsymbol{U}(\boldsymbol{x}, t)$: the displacement field at point $\boldsymbol{x}$ at time t.
2. Another body force field:
   $\boldsymbol{G}(\boldsymbol{x}, t)$: the force field, acting per unit volume,
   $\boldsymbol{T}^{(\boldsymbol{V})}(\boldsymbol{n})$: the traction,
   $\boldsymbol{V}(\boldsymbol{x}, t)$ displacement.

The notation $\boldsymbol{T}^{(\boldsymbol{U})}(\boldsymbol{n})$ and $\boldsymbol{T}^{(\boldsymbol{V})}(\boldsymbol{n})$ helps distinguish tractions of the two fields $\boldsymbol{U}$ and $\boldsymbol{V}$ from each other, and does not mean that the tractions depend on the displacements.

Betti's theorem stated that the above functions are functionally related as:

$$\boxed{\int\int\int_V (\boldsymbol{F}-\rho\ddot{\boldsymbol{U}}).\boldsymbol{V}dV + \int\int_S \boldsymbol{T}^{(\boldsymbol{U})}(\boldsymbol{n}).\boldsymbol{V}dS = \int\int\int_V (\boldsymbol{G}-\rho\ddot{V})\boldsymbol{U}dV + \int\int_S \boldsymbol{T}^{(V)}(\boldsymbol{n}).\boldsymbol{U}dS\ .} \tag{B.1}$$

Proof: Starting from left hand side (LHS) of eq. (B.1) it follows:

$$LHS = \int\int\int_V (f_i - \rho\ddot{u}_i)v_i dV + \int\int_S T_i^{(\boldsymbol{U})}(\boldsymbol{n})v_i dS\ . \tag{B.2}$$

From eq. (A.75) and eq. (A.78):

$$\begin{aligned} LHS &= \int\int\int_V -\sigma_{ij,j}^{(\boldsymbol{U})}v_i dV + \int\int_S \sigma_{ij}^{(\boldsymbol{U})}n_j v_i dS \\ &= \int\int\int_V -\sigma_{ij,j}^{(\boldsymbol{U})}v_i dV + \int\int_S (\sigma_{ij}^{(\boldsymbol{U})}v_i)n_j dS. \end{aligned} \tag{B.3}$$

where $\boldsymbol{\sigma}^{(\boldsymbol{U})}$ is the stress field of the $\boldsymbol{U}$. From the Gauss theorem eq. (A.74):

$$\begin{aligned} LHS &= \int\int\int_V -\sigma_{ij,j}^{(\boldsymbol{U})}v_i dV + \int\int\int_V (\sigma_{ij}^{(\boldsymbol{U})}v_i)_{,j} dV \\ &= \int\int\int_V -\sigma_{ij,j}^{(\boldsymbol{U})}v_i dV + \int\int\int_V (\sigma_{ij,j}^{(\boldsymbol{U})}v_i + \sigma_{ij}^{(\boldsymbol{U})}v_{i,j}) dV\ . \end{aligned} \tag{B.4}$$

Applying the constitutive equation of linear elastic bodies (eqs. A.59 and A.64) and denoting strain field of $\boldsymbol{U}$ by $\boldsymbol{e}^{(\boldsymbol{U})}$:

$$\begin{aligned} LHS &= \int\int\int_V c_{ijkl}e_{kl}^{(\boldsymbol{U})}v_{i,j} dV \\ &= \frac{1}{2}\int\int\int_V c_{ijkl}v_{i,j}(u_{k,l}+u_{l,k})dV \\ &= \frac{1}{2}\int\int\int_V c_{ijkl}v_{i,j}u_{k,l}dV + \frac{1}{2}\int\int\int c_{ijkl}v_{i,j}u_{l,k}dV \\ &= \frac{1}{2}\int\int\int_V c_{ijkl}v_{i,j}u_{k,l}dV + \frac{1}{2}\int\int\int_V c_{ijlk}v_{i,j}u_{k,l}dV. \end{aligned} \tag{B.5}$$

From the symmetries of c_{ijkl} (eq. A.61):

$$\begin{aligned} LHS &= \frac{1}{2}\int\int\int_V c_{ijkl}v_{i,j}u_{k,l}dV + \frac{1}{2}\int\int\int_V c_{ijkl}v_{i,j}u_{k,l}dV \\ &= \int\int\int_V c_{ijkl}v_{i,j}u_{k,l}dV. \end{aligned} \tag{B.6}$$

This can be rewritten in the form:

$$\begin{aligned} LHS &= \frac{1}{2}\int\int\int_V c_{ijkl}u_{k,l}v_{i,j}dV + \frac{1}{2}\int\int\int_V c_{ijkl}u_{k,l}v_{i,j}dV \\ &= \frac{1}{2}\int\int\int_V c_{ijkl}u_{k,l}v_{i,j}dV + \frac{1}{2}\int\int\int_V c_{ijkl}u_{k,l}v_{j,i}dV = \\ &= \frac{1}{2}\int\int\int_V c_{ijkl}u_{k,l}(v_{i,j}+v_{j,i})dV = \\ &= \int\int\int_V c_{ijkl}u_{k,l}e_{ij}^{(\boldsymbol{v})}dV. \end{aligned} \tag{B.7}$$

From eqs. (A.77 and A.78), the last equation can be transformed to:

$$\begin{aligned} LHS &= \int\int\int_V (g_k - \rho \ddot{v}_k) u_k dV + \int\int_S T_k^{(\boldsymbol{V})}(\boldsymbol{n}) u_k dV \\ &= \int\int\int_V (\boldsymbol{g} - \rho \ddot{\boldsymbol{v}}).\boldsymbol{u} dV + \int\int_S \boldsymbol{T}^{(\boldsymbol{V})}(\boldsymbol{n}).\boldsymbol{u} dV \ , \end{aligned} \tag{B.8}$$

which proves the Betti's theorem.

B.2.2 Displacement Field with a Quiescent Past

A special case of Betti's theorem which refers to a medium with quiescent past, i.e. when there has been no displacement before a specified time, is very helpful.

Betti's theorem holds even when F, $\boldsymbol{U}$ and $\boldsymbol{T}^{(\boldsymbol{U})}$ refer to time t, but $\boldsymbol{G}$, $\boldsymbol{V}$ and $\boldsymbol{T}^{(\boldsymbol{V})}$ to time $\tau - t$ [Aki and Richards, 1980]. Rearrangement of Betti's theorem (eq. B.1) yields:

$$\begin{aligned} \int\int\int_V \rho \left[\ddot{\boldsymbol{U}}(t).\boldsymbol{V}(\tau - t) - \boldsymbol{U}(t).\ddot{\boldsymbol{V}}(\tau - t)\right] dV &= \int\int\int_V [\boldsymbol{F}(t).\boldsymbol{V}(\tau - t) - \boldsymbol{G}(\tau - t).\boldsymbol{U}(t)] \, dV \\ &+ \int\int_S \left[\boldsymbol{T}^{(\boldsymbol{U})}(\boldsymbol{n}, t).\boldsymbol{V}(\tau - t) - \boldsymbol{T}^{(\boldsymbol{V})}(\boldsymbol{n}, \tau - t).\boldsymbol{U}(t)\right] dS \ . \end{aligned} \tag{B.9}$$

We integrate over the temporal range $-\infty$ to ∞:

$$\begin{aligned} \int_{-\infty}^{\infty} \left\{\int\int\int_V \rho \left[\ddot{\boldsymbol{u}}(t).\boldsymbol{V}(\tau - t) - \boldsymbol{U}(t).\ddot{\boldsymbol{V}}\right]\right\} dt \ &= \\ \int_{-\infty}^{\infty} \left\{\int\int\int_V [\boldsymbol{F}(t).\boldsymbol{V}(\tau - t) - \boldsymbol{G}(\tau - t).\boldsymbol{U}(t)] \, dV\right\} dt & \\ + \int_{-\infty}^{\infty} \left\{\int\int_S \left[\boldsymbol{T}^{(\boldsymbol{U})}(\boldsymbol{n}, t).\boldsymbol{V}(\tau - t) - \boldsymbol{T}^{(\boldsymbol{V})}(\boldsymbol{n}, \tau - t).\boldsymbol{u}(t)\right] dS\right\} dt \ . & \end{aligned} \tag{B.10}$$

For an incompressible material, $\left(\frac{d\rho}{dt} = 0\right)$ and we can write the last equation as:

$$\begin{aligned} \int\int\int_V \left\{\rho \int_{-\infty}^{\infty} \left[\ddot{\boldsymbol{U}}(t).\boldsymbol{V}(\tau - t) - \boldsymbol{U}(t).\ddot{\boldsymbol{V}}(\tau - t)\right] dt\right\} dV &= \\ \int_{-\infty} \left\{\int\int\int_V [\boldsymbol{F}(t)\boldsymbol{V}(\tau - t) \ \ -\boldsymbol{G}(\tau - t).\boldsymbol{U}(t)] \, dV\right\} dt & \\ + \int_{-\infty}^{\infty} \left\{\int\int_S \left[\boldsymbol{T}^{(\boldsymbol{U})}(\boldsymbol{n}, t).\boldsymbol{V}(\tau - t) \ \ -\boldsymbol{T}^{(\boldsymbol{V})}(\boldsymbol{n}, \tau - t).\boldsymbol{U}(t) dS\right] dt\right\} \ . & \end{aligned} \tag{B.11}$$

Integrating the left hand side gives:

$$\int\int\int_V \left\{\rho \int_{-\infty}^{\infty} \left[\ddot{\boldsymbol{U}}(t).\boldsymbol{V}(\tau - t) - \boldsymbol{U}(t).\ddot{\boldsymbol{V}}(\tau - t)\right] dt\right\} dV = \int\int\int_V \rho \left\{\dot{\boldsymbol{U}}(t).\boldsymbol{V}(\tau - t) - \boldsymbol{U}(t).\dot{\boldsymbol{V}}(\tau - t)\right\}_{-\infty}^{\infty} dV \ . \tag{B.12}$$

Quiescent past means no motion before a specified time τ_0:

$$\boldsymbol{U}(t) = \dot{\boldsymbol{U}}(t) = 0; \ t < \tau_0 \ , \tag{B.13}$$

$$\boldsymbol{V}(\tau - t) = \dot{\boldsymbol{V}}(\tau - t) = 0; \ \tau - t < \tau_0. \tag{B.14}$$

We introduce integral boundaries:

$$\boldsymbol{U}(-\infty) = \dot{\boldsymbol{U}}(-\infty) = \boldsymbol{V}(\tau - \infty) = \dot{\boldsymbol{V}}(\tau - \infty) = 0 \tag{B.15}$$

for any τ and τ_0. The right hand side is zero as well, and we conclude that for $\tau < \tau_0$:

$$\boxed{\begin{aligned}&\int_{-\infty}^{\infty} dt \int\int\int_V \{\boldsymbol{U}(\boldsymbol{x},t).\boldsymbol{G}(\boldsymbol{x},\tau-t) - \boldsymbol{V}(\boldsymbol{x},\tau-t).\boldsymbol{F}(\boldsymbol{x},t)\}\, dV = \\ &\int_{-\infty}^{\infty} dt \int\int_S \left\{\boldsymbol{V}(\boldsymbol{x},\tau-t).\boldsymbol{T}^{(\boldsymbol{U})}(\boldsymbol{n},t) - \boldsymbol{U}(\boldsymbol{x},t).\boldsymbol{T}^{(\boldsymbol{V})}(\boldsymbol{n},\tau-t)\right\} dS\ .\end{aligned}} \tag{B.16}$$

Therefore having a displacement source, i.e. the body force field and surface tractions, in a body of incompressible material with quiescent past, the last formula helps calculate the unknown displacement field of any other known source. This is done by introducing *Green's function.*

B.2.3 Green's Function

In order to compute the displacement field of a known source in an incompressible body with quiescent past, we define the simplest possible source, a concentrated unit force, calculate its displacement field, which is called Green's function, then introduce this to the eq. (B.16) together with the body forces and tractions of another source, and obtain the displacement field.

The case of earthquakes is not dealt with in terms of forces and tractions as they appear in the eq. (B.16). There is a *fault,* for which an *equivalent body force field* is computed, i.e. a non-existing force field which would produce the same displacement field as the fault, if it existed. Then this equivalent force field is used as one source in Betti's theorem, and the displacement field of the slip across the fault is computed. This process requires some mathematical tools as follows.

Suppose that the a unit impulse is applied at $\boldsymbol{x} = \boldsymbol{x}_0$ and $t = t_0$ along the direction $\boldsymbol{e}_n$. The impulse is known can be written as:

$$f_i(\boldsymbol{x},t) = A\delta(\boldsymbol{x}-\boldsymbol{x}_0)\delta(t-t_0)\delta_{in}\ , \tag{B.17}$$

where:

- A is the unit constant with the dimension of force,
- $\delta(\boldsymbol{x})$ is the three dimensional Dirac delta function with the dimension of $\dfrac{1}{\text{volume}}$,
- $\delta(t)$ is the one dimensional Dirac delta function with dimension of $\dfrac{1}{\text{time}}$,
- δ_{in} is the dimensionless Kronecker delta function.

Such a source is sometimes called *concentrated force.*

The displacement field generated by the concentrated force is denoted as $AG_{in}(\boldsymbol{x},t;\boldsymbol{x}_0,t_0)$ and is known as *elastodynamic Green's function.* The value of the function $G(\boldsymbol{x},t;\boldsymbol{x}_0,t_0)$ would be equal to the displacement value at point $\boldsymbol{x}$, at time t in the direction $\boldsymbol{e}_i$, caused by the concentrated unit force applied at point $\boldsymbol{x}_0$ and time t_0 in the direction $\boldsymbol{e}_0$, i.e. it depends on the receiver and source coordinates. The Green's function must satisfy the condition:

$$\rho\frac{\partial^2}{\partial t^2}G_{in}(\boldsymbol{x},t;\boldsymbol{x}_0,t_0) = \delta_{in}\delta(\boldsymbol{x}-\boldsymbol{x}_0)\delta(t-t_0) + \frac{\partial}{\partial x_j}\left[c_{ijkl}\frac{\partial}{\partial x_l}G_{kn}(\boldsymbol{x},t;\boldsymbol{x}_0,t_0)\right] \tag{B.18}$$

throughout the source [Aki and Richards, 1980], where c_{ijkl} are the coefficients of the constitutive equation of linearly elastic bodies. The following initial and boundary conditions apply:

1. Initial conditions:

$$\left.\begin{aligned}\boldsymbol{G}(\boldsymbol{x},t;\boldsymbol{x}_0,t_0) &= \boldsymbol{0}\\ \frac{\partial}{\partial t}\boldsymbol{G}(\boldsymbol{x},t;\boldsymbol{x}_0,t_0) &= \boldsymbol{0}\end{aligned}\right\}\ \text{for } t < t_0\ . \tag{B.19}$$

2. Either of the following homogeneous boundary conditions:

   (a) The surface of the body is rigid:

$$u_i(\boldsymbol{x}) = 0\ ;\ \boldsymbol{x}\in S\ . \tag{B.20}$$

   Therefore the boundary conditions are independent of time. Then the time origin can be shifted, and $\boldsymbol{G}$ does not depend on absolute time, but on $t-t_0$:

$$\boldsymbol{G}(\boldsymbol{x},t;\boldsymbol{x}_0,t_0) = \boldsymbol{G}(\boldsymbol{x},t-t_0;\boldsymbol{x}_0,0) = \boldsymbol{G}(\boldsymbol{x},-t_0;\boldsymbol{x}_0,-t) \tag{B.21}$$

which is called a *reciprocal relation,* i.e. a relation between a pair of solutions for the displacements throughout an elastic body. This equation is a reciprocal relation for source and receiver times.

(b) No tractions on surface S:

$$\sigma_{ij} n_i = 0 \ . \tag{B.22}$$

B.2.4 Proof of Some Reciprocity Theorems

From Betti's theorem for the displacement field of an incompressible body with quiescent past, and with:
$\boldsymbol{f}$:=unit impulse applied in m-direction at $\boldsymbol{x} = \boldsymbol{x}_1$ and $t = t_1$;
$\boldsymbol{g}$:=unit impulse applied in n-direction at $\boldsymbol{x} = \boldsymbol{x}_2$ and $t = t_2$:

$$f_i(\boldsymbol{x}, t) = A\delta(\boldsymbol{x} - \boldsymbol{x}_1)\delta(t - t_1)\delta_{im} \ , \tag{B.23}$$

$$g_i(\boldsymbol{x}, t) = A\delta(\boldsymbol{x} - \boldsymbol{x}_2)\delta(t + t_2)\delta_{in} \ , \tag{B.24}$$

the corresponding displacements fields are:

$$u_i(\boldsymbol{x}, t) = AG_{im}(\boldsymbol{x}, t; \boldsymbol{x}_1, t_1) \ , \tag{B.25}$$

$$v_i(\boldsymbol{x}, t) = AG_{in}(\boldsymbol{x}, t; \boldsymbol{x}_2, -t_2) \ , \tag{B.26}$$

respectively. The presence of the unit impulse A guarantees the dimensional identity of the above two sides.

We substitute eqs. (B.23-B.26) into eq. (B.16). The right hand side vanishes for both homogeneous cases:

1. Rigid surface, i.e. no displacement on the surface :

$$\boldsymbol{U}(\boldsymbol{x}, t) = \boldsymbol{V}(\boldsymbol{x}, t) = 0 \ ; \ \boldsymbol{x} \in S \ . \tag{B.27}$$

2. No traction:

$$\boldsymbol{T}^{(\boldsymbol{U})}(\boldsymbol{n}) = \boldsymbol{T}^{(\boldsymbol{V})}(\boldsymbol{n}) = 0 \ ; \ \boldsymbol{x} \in S \ . \tag{B.28}$$

Therefore

$$\int_{-\infty}^{\infty} dt \int\int\int_V \{\boldsymbol{U}(\boldsymbol{x}, t).G(\boldsymbol{x}, \tau - t) - \boldsymbol{V}(\boldsymbol{x}, \tau - t).\boldsymbol{F}(\boldsymbol{x}, t)\} \, dV \ , \tag{B.29}$$

$$\int_{-\infty}^{\infty} dt \int\int\int_V u_i(\boldsymbol{x}, t) g_i(\boldsymbol{x}, \tau - t) dV = \int_{-\infty}^{\infty} dt \int\int\int_V v_i(\boldsymbol{x}, \tau - t) f_i(\boldsymbol{x}, t) dV. \tag{B.30}$$

Substituting eqs. (B.23-B.26):

$$\begin{aligned} \int_{-\infty}^{\infty} dt \int\int\int_V G_{im}(\boldsymbol{x}, t; \boldsymbol{x}_1, t_1) A\delta(\boldsymbol{x} - \boldsymbol{x}_2)\delta(\tau - t + t_2)\delta_{in} dV &= \\ = \int_{-\infty}^{\infty} dt \int\int\int_V G_{in}(\boldsymbol{x}, \tau - t; \boldsymbol{x}_2, -t_2) A\delta(\boldsymbol{x} - \boldsymbol{x}_1)\delta(t - t_1)\delta_{im} dV. \end{aligned} \tag{B.31}$$

Summation over index i yields:

$$\begin{aligned} \int_{-\infty}^{\infty} dt \int\int\int_V G_{nm}(\boldsymbol{x}, t; \boldsymbol{x}_1, t_1) A\delta(\boldsymbol{x} - \boldsymbol{x}_2)\delta(\tau - t + t_2) dV &= \\ = \int_{-\infty}^{\infty} dt \int\int\int_V G_{mn}(\boldsymbol{x}, \tau - t; \boldsymbol{x}_2, -t_2) A\delta(\boldsymbol{x} - \boldsymbol{x}_1)\delta(t - t_1) dV. \end{aligned} \tag{B.32}$$

After integration over the volume:

$$\begin{aligned} \int_{-\infty}^{\infty} AG_{nm}(\boldsymbol{x}_2, t; \boldsymbol{x}_1, t_1)\delta(\tau - t + t_2) dt &= \\ = \int_{-\infty}^{\infty} AG_{mn}(\boldsymbol{x}_1, \tau - t; \boldsymbol{x}_2, -t_2)\delta(t - t_1) dt \ . \end{aligned} \tag{B.33}$$

Integration over time and eliminating the constant A from both sides finally yields:

$$G_{nm}(\boldsymbol{x}_2, \tau + t_2; \boldsymbol{x}_1, t_1) = G_{mn}(\boldsymbol{x}_1, \tau - t_1; \boldsymbol{x}_2, -t_2). \tag{B.34}$$

For $t_1 = t_2 = 0$:

$$G_{nm}(\boldsymbol{x}_2, \tau; \boldsymbol{x}_1, 0) = G_{mn}(\boldsymbol{x}_1, \tau; \boldsymbol{x}_2, 0) \tag{B.35}$$

which is a spatial reciprocity, i.e. a reciprocal relation for source and receiver positions, saying that the n-th displacement component at the position $\boldsymbol{x}_2$ due to a concentrated force at the position $\boldsymbol{x}_1$ applied in direction $\boldsymbol{e}_m$ after the time τ equals the m-th displacement component at the position $\boldsymbol{x}_1$ due to a concentrated force at the position $\boldsymbol{x}_2$ applied in direction $\boldsymbol{e}_n$ after the same time τ.

For $\tau = 0$ in eq. (B.34):

$$G_{nm}(\boldsymbol{x}_2, t_2; \boldsymbol{x}_1, t_1) = G_{mn}(\boldsymbol{x}_1, -t_1; \boldsymbol{x}_2, -t_2) \ , \tag{B.36}$$

which is a space-time reciprocity.

B.2.5 Important Cases

A number of important formulae can be derived from the fundamental equation (eq. B.16). Three of them are considered here, others are discussed in the next section.

1. The displacement field of a general source is computed when the Green's function is known, assuming that the incompressible body has been at rest before the action of the source.
   Known functions:

   - A unit concentrated force applied at space-time point $(\boldsymbol{x}_0, t_0)$:

   $$g_i(\boldsymbol{x}, t) = A\delta(\boldsymbol{x} - \boldsymbol{x}_0)\delta(t - t_0)\delta_{in} \ . \tag{B.37}$$

   - Green's function is the normalized displacement field of the above source:

   $$v_i(\boldsymbol{x}, t) = AG_{in}(\boldsymbol{x}, t; \boldsymbol{x}_0, t_0). \tag{B.38}$$

   - A general source:

   $$f_i(\boldsymbol{x}, t) \ ; \ \boldsymbol{x} \in V \ ,$$

   with the physical dimension of force per volume, which is not necessarily a point source.
   Unknown function:
   - Displacement field generated by the source

   $$u_i(\boldsymbol{x}, t) \ .$$

   Homogeneous boundary conditions:
   Substituting into eq. (B.16) and eliminating the dimensionality factor A from both sides gives:

   $$\int_{-\infty}^{\infty} dt \int\int\int_V u_i(\boldsymbol{x}, t)\delta(\boldsymbol{x} - \boldsymbol{x}_0)\delta(t - t_0)\delta_{in} dV = \int_{-\infty}^{\infty} dt \int\int\int_V G_{in}(\boldsymbol{x}, t; \boldsymbol{x}_0, t_0) f_i(\boldsymbol{x}, t) dV \ . \tag{B.39}$$

   Carrying out the integrations on the left hand side, this reduces to:

   $$u_n(\mathbf{x}_0, t_0) = \int_{-\infty}^{\infty} dt \int\int\int_V G_{in}(\boldsymbol{x}, t; \boldsymbol{x}_0, t_0) f_i(\boldsymbol{x}, t) dV \ , \tag{B.40}$$

   which is the classical definition of a Green's function as the kernel of a convolution integral. Since the argument of the displacement field is usually denoted by $(\boldsymbol{x}, t)$, we may change the notation as follows:

   - $(\boldsymbol{x}, t)$ instead of $(\boldsymbol{x}_0, t_0)$,
   - $(\boldsymbol{\xi}, \tau)$ instead of $(\boldsymbol{x}, t)$.

   Therefore:

   $$u_n(,t) = \int_{-\infty}^{\infty} d\tau \int\int\int_V G_{in}(\boldsymbol{\xi}, \tau; \boldsymbol{x}, t) f_i(\boldsymbol{\xi}, \tau) dV \ , \tag{B.41}$$

   which my be abbreviated using the convolution symbol:

   $$u_n(\boldsymbol{x}, t) = \int\int\int_V G_{in}(\boldsymbol{\xi}, \tau; \boldsymbol{x}, t) \star f_i(\boldsymbol{\xi}, \tau) dV \ . \tag{B.42}$$

2. For non-homogeneous boundary conditions with:

   - Displacement values for the unit impulse on the boundary surface:

     $$AG_{in}(\boldsymbol{\xi};\tau;\boldsymbol{x},t)\ ;\ \boldsymbol{x}\in S\ .$$

   - Known values of the displacement field on the boundary surface:

     $$u_i(\boldsymbol{x},t)\ ;\ \boldsymbol{x}\in S\ .$$

   - Unknown function is the displacement field over the deforming body:

     $$u_i(\boldsymbol{x},t)\ ;\ \boldsymbol{x}\in V-S\ .$$

   Eq. (B.16):

   $$\begin{aligned}\int_{-\infty}^{\infty}d\tau\int\int\int_V u_i(\boldsymbol{x},t)\delta(\boldsymbol{x}-\boldsymbol{\xi})\delta(\tau-t)\delta_{in}G_{in}(\boldsymbol{\xi},\tau-t;\boldsymbol{x},0)f_i(\boldsymbol{\xi},\tau)dV(\boldsymbol{\xi}) \quad &= \\ =\int_{-\infty}^{\infty}d\tau\int\int_S\left[G_{in}(\boldsymbol{\xi},\tau-t;\boldsymbol{x},0)T_i^{(\boldsymbol{U})}(\boldsymbol{\nu})-\frac{1}{A}u_i(\boldsymbol{\xi},\tau)T_i^{(\boldsymbol{V})}(\boldsymbol{\nu})\right]dS(\boldsymbol{\xi})\ , \qquad &\text{(B.43)}\end{aligned}$$

   where $\boldsymbol{\nu}$ is unit normal of S. Carrying out the integration over the first term of the integrand in left hand side, we obtain:

   $$\begin{aligned}u_n(\boldsymbol{x},t) \quad = \quad & \int_{-\infty}^{\infty}d\tau\int\int\int_V G_{in}(\boldsymbol{\xi},\tau-t;\boldsymbol{x},0)f_i(\boldsymbol{\xi},\tau)dV(\boldsymbol{\xi}) \\ + \quad & \int_{-\infty}^{\infty}d\tau\int\int_S\Big[G_{in}(\boldsymbol{\xi},\tau-t;\boldsymbol{x},0)T_i^{(U(\boldsymbol{\xi},\tau))}(\boldsymbol{\nu}) \\ - \quad & \frac{1}{A}\,u_i(\boldsymbol{\xi},\tau)T_i^{(\boldsymbol{V}(\boldsymbol{\xi},\tau-t))}(\boldsymbol{\nu})\Big]\,dS(\boldsymbol{\xi})\ . \qquad \text{(B.44)}\end{aligned}$$

   We know from eq. (A.75) that:

   $$T_i^{(\boldsymbol{V}(\boldsymbol{\xi},\tau-t))}(\boldsymbol{\nu})=\sigma_{ji}(\boldsymbol{\xi},\tau-t)n_j(\boldsymbol{\xi})\ . \qquad \text{(B.45)}$$

   $$\sigma_{ji}^{(\boldsymbol{v})}(\boldsymbol{\xi},\tau-t)=c_{jikl}(\boldsymbol{\xi})e_{kl}^{(\boldsymbol{v})}\ , \qquad \text{(B.46)}$$

   $$e_{ji}^{(\boldsymbol{V})}(\boldsymbol{\xi},\tau-t)=\frac{1}{2}\left[\frac{\partial v_k(\boldsymbol{\xi},\tau-t)}{\partial\xi_l}+\frac{\partial v_l(\boldsymbol{\xi},\tau-t)}{\partial\xi_k}\right]\ , \qquad \text{(B.47)}$$

   Combining the last three equations yields:

   $$T_i^{(\boldsymbol{V}(\boldsymbol{\xi},\tau-t))}(\boldsymbol{\nu})=c_{ijkl}(\boldsymbol{\xi})\nu_j(\boldsymbol{\xi})v_{k,l}(\boldsymbol{\xi},\tau-t)\ . \qquad \text{(B.48)}$$

   From eq. (B.38):

   $$v_{k,l}(\boldsymbol{\xi},\tau-t)=AG_{kn,l}(\boldsymbol{\xi},\tau-t;\boldsymbol{x},0)\ . \qquad \text{(B.49)}$$

   Therefore:

   $$T_i^{(\boldsymbol{V}(\boldsymbol{\xi},\tau-t))}(\boldsymbol{\nu})=AC_{ijkl}(\boldsymbol{\xi})\nu_j(\boldsymbol{\xi})G_{kn,l}(\boldsymbol{\xi},\tau-t;\boldsymbol{x},0)\ . \qquad \text{(B.50)}$$

   If this result is applied to the eq. (B.44), we obtain:

   $$\begin{aligned}u_n(\boldsymbol{x},t) \quad = \quad & \int_{-\infty}^{\infty}d\tau\int\int\int_V G_{in}(\boldsymbol{\xi},\tau-t;\boldsymbol{x},0)f_i(\boldsymbol{\xi},\tau)dV(\boldsymbol{\xi}) \\ + \quad & \int_{-\infty}^{\infty}d\tau\int\int_S\Big[G_{in}(\boldsymbol{\xi},\tau-t;\boldsymbol{x},0)T_i^{(\boldsymbol{U}(\boldsymbol{\xi},\tau))}(\boldsymbol{\nu}) \\ - \quad & u_i(\boldsymbol{\xi}\,\tau)c_{ijkl}(\boldsymbol{\xi})\nu_j(\boldsymbol{\xi})G_{kn,l}(\boldsymbol{\xi},\tau-t;\boldsymbol{x},0)\,]dS(\boldsymbol{\xi})\ . \qquad \text{(B.51)}\end{aligned}$$

3. In the special case of homogeneous boundary conditions and with the source of the unknown displacement field a non-unit impulse applied at $(\boldsymbol{x}_0, t_0)$ in the direction $\boldsymbol{e}_0$, we may write:

$$\boldsymbol{f}(\boldsymbol{\xi}, \tau) = f_n \delta(\boldsymbol{\xi} - \boldsymbol{x}_0) \delta(\tau - t_0) \boldsymbol{e}_0 \ , \tag{B.52}$$

with physical dimensions as in eq. (B.17). From eq. (B.41) we have:

$$u_n(\boldsymbol{x}, t) = \int_{-\infty}^{\infty} d\tau \int\int\int_V G_{in}(\boldsymbol{\xi}, \tau; \boldsymbol{x}, t) f_i \delta(\boldsymbol{\xi} - \boldsymbol{x}_0) \delta(\tau - \tau_0) dV \ . \tag{B.53}$$

Eliminating the delta functions finally yields:

$$u_n(\boldsymbol{x}, t) = G_{in}(\boldsymbol{x}_0, t_0; \boldsymbol{x}, t) f_i \ . \tag{B.54}$$

Special combinations of concentrated forces are very important in earthquake studies and are discussed later.

B.3 EQUIVALENT BODY FORCES

In order to apply the mathematical tools for solving the displacement field of a source, e.g. an earthquake, we need one more concept: *equivalent body forces.* They are non-real forces which produce the same displacement field as the actual source. The resultant equivalent body forces for traction discontinuities and displacement discontinuities are considered in the following. Readers interested in a more detailed discussion are recommended to refer to Aki and Richards [1980].

Displacement Discontinuity

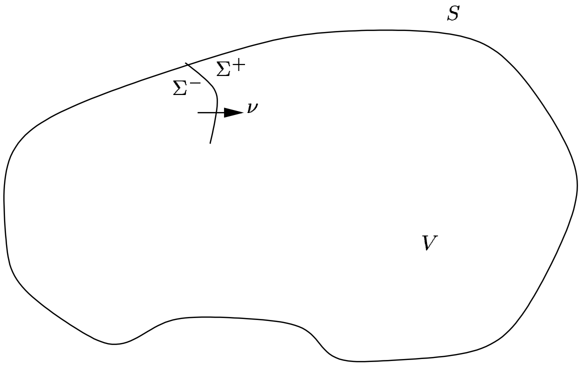

Figure B.1: An elastic body, with volume V, external surface S, and internal discontinuity surface Σ

Suppose that a slip occurs across a fault Σ with the sides Σ^+ and Σ^- (figure B.1), the displacement $\boldsymbol{u}$, the Green's function $\boldsymbol{G}$, the unit normal of the fault $\boldsymbol{\nu}$, and the elastic constants c_{ijkl}. The difference of any function f on the two sides of the fault is denoted by $[f]$:

$$[f(\boldsymbol{x})] := f(\boldsymbol{x} \in \Sigma^+) - f(\boldsymbol{x} \in \Sigma^-) \ . \tag{B.55}$$

We assume that $\boldsymbol{u}$ and $\boldsymbol{G}$ satisfy homogeneous boundary conditions on S.

The discontinuity surface Σ is considered as part of the boundary surface. The selection of positive and negative sides and therefore the positive and negative directions of $\boldsymbol{\nu}$ are arbitrary. A positive and a negative neighborhood of Σ are defined. The boundary integral turns to include the discontinuity surface as well as the outer surface of the body.

When the two sides of the discontinuity surface slip with respect to each other, e.g. in response to a point source in the body, the equation of motion, eq. (A.78), is not valid on it any more. This slippage in turn becomes a source, i.e. each point of it acts as a point source, and deforms the body in addition to the deformation caused by the first point source.

The point on the fracture surface $\boldsymbol{\xi} \in \Sigma$ is displaced by the first point source, therefore:

$$u_i(\boldsymbol{\xi}, \tau) = A G_{in}(\boldsymbol{\xi}, \tau; \boldsymbol{x}_0, t_0) \ ; \ \boldsymbol{\xi} \in \Sigma \ . \tag{B.56}$$

The strain tensor for this displacement is:

$$e_{pq}(\boldsymbol{\xi},\tau)=\frac{A}{2}\left\{G_{pn,q}(\boldsymbol{\xi},\tau;\boldsymbol{x}_0,t_0)+G_{qn,p}(\boldsymbol{\xi},\tau;\boldsymbol{x}_0,t_0)\right\}\ , \tag{B.57}$$

From eq. (A.64), the stress tensor becomes:

$$\tau_{ij}(\boldsymbol{\xi},\tau)=c_{ijpq}(\boldsymbol{\xi})e_{pq}(\boldsymbol{\xi},\tau)\ , \tag{B.58}$$

and the resulting surface tractions acts on the body particles as another source (eq. A.75):

$$h_i^{[\boldsymbol{U}]}(\boldsymbol{\xi},\tau)=\tau_{ij}(\boldsymbol{\xi})\nu_j(\boldsymbol{\xi})\ ;\ \boldsymbol{\xi}\in\Sigma\ . \tag{B.59}$$

Therefore, the following term is added to the equations as a new dislocation source:

$$\begin{aligned}h_i^{[\boldsymbol{U}]}(\boldsymbol{\xi},\tau) &= c_{ijpq}(\boldsymbol{\xi})e_{pq}(\boldsymbol{\xi},\tau)\nu_j(\boldsymbol{\xi})\\ &= \frac{A}{2}c_{ijpq}(\boldsymbol{\xi})\nu_j(\boldsymbol{\xi})\left\{G_{pn,q}(\boldsymbol{\xi},\tau;\boldsymbol{x}_0,t_0)+G_{qn,p}(\boldsymbol{\xi},\tau;\boldsymbol{x}_0,t_0)\right\}\ .\end{aligned} \tag{B.60}$$

In view of the summation convention and the symmetries of c_{ijpq}, this reduces to:

$$h_i^{[\boldsymbol{U}]}=c_{ijpq}\nu_j G_{pn,q}\ . \tag{B.61}$$

Traction Discontinuity

If for any reason, e.g. application of external forces, the reaction on Σ is discontinuous, then:

$$\boldsymbol{h}^{[\boldsymbol{T}]}=\left[\boldsymbol{T}^{(\boldsymbol{\xi},\tau)}(\boldsymbol{\nu})\right]\neq\boldsymbol{0}\ ;\ \boldsymbol{\xi}\in\Sigma\ ,\ \boldsymbol{\nu}\perp\Sigma \tag{B.62}$$

acts as another source.

In order to have a correct solution for the deformation in the elastic body under consideration, the discontinuity surface has to be taken into account. One way to do this is to include the surface in the boundary surface as in eq. (B.51). Then this form can be simplified by a mathematical trick. We can compute non-real body forces which produce the same effect as the discontinuity. These forces are called *equivalent body forces.* They allow us to replace the surface integration over discontinuity surface by the volume integration over equivalent body forces and thus exclude the discontinuity surface from the boundary integration. The equivalent body forces are added to the body forces in eq. (B.51).

The body force equivalents to traction discontinuity and displacement discontinuity are considered in the following.

Having included the discontinuity in the boundary surface (figure B.1), we have:

$$\text{Boundary}=S+\Sigma\ ,$$

where S is the outer surface of the elastic boy and Σ is the discontinuity surface. Eq. (B.51) can be rewritten as:

$$\begin{aligned}u_n(\boldsymbol{x},t) &= \int_{-\infty}^{\infty}d\tau\int\!\!\int\!\!\int_V G_{in}(\boldsymbol{\xi},\tau-t;\boldsymbol{x},0)f_i(\boldsymbol{\xi},\tau)dV(\boldsymbol{\xi})\\ &+ \int_{-\infty}^{\infty}d\tau\int\!\!\int_S\Big\{G_{in}(\boldsymbol{\xi},\tau-t;\boldsymbol{x},0)T_i^{(\boldsymbol{U}(\boldsymbol{\xi},\tau))}(\boldsymbol{\nu})\\ &- \{Au_i(\boldsymbol{\xi},\tau)c_{ijkl}(\boldsymbol{\xi})\nu_j G_{kn,l}(\boldsymbol{\xi},\tau-t;\boldsymbol{x},0)\ dS(\boldsymbol{\xi})\\ &+ \int_{-\infty}^{\infty}d\tau\int\!\!\int_\Sigma\Big\{G_{in}(\boldsymbol{\xi},\tau-t;\boldsymbol{x},0)T_i^{(\boldsymbol{U}(\boldsymbol{\xi},\tau))}(\boldsymbol{\nu})\\ &- Au_i(\boldsymbol{\xi},\tau)c_{ijkl}(\boldsymbol{\xi})\nu_j(\boldsymbol{\xi})G_{kn,l}(\boldsymbol{\xi},\tau-t;\boldsymbol{x},0)\}\,d\Sigma(\boldsymbol{\xi})\ .\end{aligned} \tag{B.63}$$

Therefore

$$\begin{aligned}u_n(\boldsymbol{x},t) &= \int_{-\infty}^{\infty}d\tau\int\!\!\int\!\!\int_V G_{in}(\boldsymbol{\xi},\tau-t;\boldsymbol{x},0)f_i(\boldsymbol{\xi}\,\tau)dV(\boldsymbol{\xi})\\ &+ \int_{-\infty}^{\infty}d\tau\int\!\!\int_S\Big\{G_{in}(\boldsymbol{\xi},\tau-t;\boldsymbol{x},0)T_i^{(\boldsymbol{U}(\boldsymbol{\xi},\tau))}(\boldsymbol{\nu})\end{aligned}$$

$$
\begin{aligned}
&- \{Au_i(\boldsymbol{\xi},\tau)c_{ijkl}(\boldsymbol{\xi})\nu_j G_{kn,l}(\boldsymbol{\xi},\tau-t;\boldsymbol{x},0)\ dS(\boldsymbol{\xi})\\
&+ \int_{-\infty}^{\infty} d\tau \int\int_{\Sigma^+} \Big\{G_{in}(\boldsymbol{\xi},\tau-t;\boldsymbol{x},0)T_i^{(\boldsymbol{U}(\boldsymbol{\xi},\tau))}(\boldsymbol{\nu})\\
&- Au_i(\boldsymbol{\xi},\tau)c_{ijkl}(\boldsymbol{\xi})\nu_j(\boldsymbol{\xi})G_{kn,l}(\boldsymbol{\xi},\tau-t;\boldsymbol{x},0)\}\,d\Sigma^+(\boldsymbol{\xi})\\
&- \int_{-\infty}^{\infty} d\tau \int\int_{\Sigma^-} \Big\{G_{in}(\boldsymbol{\xi},\tau-t;\boldsymbol{x},0)T_i^{(\boldsymbol{U}(\boldsymbol{\xi},\tau))}(\boldsymbol{\nu})\\
&- Au_i(\boldsymbol{\xi},\tau)c_{ijkl}(\boldsymbol{\xi})\nu_j(\boldsymbol{\xi})G_{kn,l}(\boldsymbol{\xi},\tau-t;\boldsymbol{x},0)\}\,d\Sigma^-(\boldsymbol{\xi})\}.
\end{aligned}
\tag{B.64}
$$

The next to last integral is preceeded by a minus sign because of the sign change of $\boldsymbol{\nu}$ from Σ^+ to Σ^-. Rearranging the surface integrals over Σ^+ and Σ^-, we obtain:

$$
\begin{aligned}
u_n(\boldsymbol{x},t) &= \int_{-\infty}^{\infty} d\tau \int\int\int_V G_{in}(\boldsymbol{\xi},\tau-t;\boldsymbol{x},0)f_i(\boldsymbol{\xi}\,\tau)dV(\boldsymbol{\xi})\\
&+ \int_{-\infty}^{\infty} d\tau \int\int_S \Big\{G_{in}(\boldsymbol{\xi},\tau-t;\boldsymbol{x},0)T_i^{(\boldsymbol{U}(\boldsymbol{\xi},\tau))}(\boldsymbol{\nu})\\
&- \{Au_i(\boldsymbol{\xi},\tau)c_{ijkl}(\boldsymbol{\xi})\nu_j G_{kn,l}(\boldsymbol{\xi},\tau-t;\boldsymbol{x},0)\ dS(\boldsymbol{\xi})\\
&+ \int_{-\infty}^{\infty} d\tau \int\int_\Sigma G_{in}(\boldsymbol{\xi},\tau-t;\boldsymbol{x},0)\left\{T_i^{(\boldsymbol{U}(\boldsymbol{\xi}^+,\tau))}(\boldsymbol{\nu}) - T_i^{((\boldsymbol{\xi}^-,\tau))}(\boldsymbol{\nu})\right\}d\Sigma(\boldsymbol{\xi})\\
&- A\int_{-\infty}^{\infty}\int\int_\Sigma (u_i(\boldsymbol{\xi}^+,\tau)-u_i(\boldsymbol{\xi}^-,\tau))c_{ijkl}(\boldsymbol{\xi})\nu_j(\boldsymbol{\xi})G_{kn,l}(\boldsymbol{\xi},\tau-t;\boldsymbol{x},0)d\Sigma
\end{aligned}
\tag{B.65}
$$

where $\boldsymbol{\xi}^+$ and $\boldsymbol{\xi}^-$ are two neighboring points on Σ^+ and Σ^- respectively. Using the notation introduced by eq. (B.55), this may be rewritten as:

$$
\boxed{
\begin{aligned}
u_n(\boldsymbol{x},t) &= \int_{-\infty}^{\infty} d\tau \int\int\int_V G_{in}(\boldsymbol{\xi},\tau-t;\boldsymbol{x},0)f_i(\boldsymbol{\xi},\tau)dV(\boldsymbol{\xi})\\
&+ \int_{-\infty}^{\infty} d\tau \int\int_S \Big\{G_{in}(\boldsymbol{\xi},\tau-t;\boldsymbol{x},0)T_i^{(\boldsymbol{u}(\boldsymbol{\xi},\tau))}(\boldsymbol{\nu})\\
&- Au_i(\boldsymbol{\xi},\tau)c_{ijkl}(\boldsymbol{\xi})\nu_j(\boldsymbol{\xi})G_{kn,l}(\boldsymbol{\xi},\tau-t;\boldsymbol{x},0)\}\,dS(\boldsymbol{\xi})\\
&+ \int_{-\infty}^{\infty} d\tau \int\int_\Sigma G_{in}(\boldsymbol{\xi},\tau-t;\boldsymbol{x},0)\left[T_i^{(\boldsymbol{u}(\boldsymbol{\xi},\tau))}(\boldsymbol{\nu})\right]d\Sigma(\boldsymbol{\xi})\\
&- \int_{-\infty}^{\infty} d\tau \int\int_\Sigma \left[u_i(\boldsymbol{\xi},\tau)\right]c_{ijkl}(\boldsymbol{\xi})\nu_j(\boldsymbol{\xi})G_{kn,l}(\boldsymbol{\xi},\tau-t;\boldsymbol{x},0)d\Sigma(\boldsymbol{\xi})\ .
\end{aligned}
}
\tag{B.66}
$$

B.3.1 Body Force Equivalent to Traction Discontinuity

From eq. (B.66) we see the effect of the traction discontinuity on Σ as:

$$
u_n^{[\boldsymbol{T}]}(\boldsymbol{x},t) = \int_{-\infty}^{\infty} d\tau \int\int_\Sigma G_{in}(\boldsymbol{\xi},\tau-t;\boldsymbol{x},0)\left[T_i^{(\boldsymbol{u}(\boldsymbol{\xi},\tau))}(\boldsymbol{\nu})\right]d\Sigma(\boldsymbol{\xi})\ . \tag{B.67}
$$

We need an expression equivalent to $\left[T_i^{(\boldsymbol{u}(\boldsymbol{\xi},\tau))}(\boldsymbol{\nu})\right]$ with the dimension of volume force density. Using the properties of the delta function, we can rewrite the last equation as:

$$
u_n^{[\boldsymbol{T}]} = \int_{-\infty}^{\infty} d\tau \int\int_\Sigma G_{in}(\boldsymbol{\xi},\tau-t;\boldsymbol{x},0)\left\{\int\int\int_V \left[T_i^{(\boldsymbol{u}(\boldsymbol{\xi},\tau)}(\boldsymbol{\nu})\right]\delta(\boldsymbol{\eta}-\boldsymbol{\xi})dV(\boldsymbol{\eta})\right\}d\Sigma(\boldsymbol{\xi}) \tag{B.68}
$$

According to Fubini's theory of interchanging the order of integration:

$$
\begin{aligned}
u_n^{[\boldsymbol{T}]}(\boldsymbol{x},t) &= \int_{-\infty}^{\infty} d\tau \int\int\int_V G_{in}(\boldsymbol{\xi},\tau-t;\boldsymbol{x},0)\left\{\int\int_\Sigma \left[T_i^{(\boldsymbol{u}(\boldsymbol{\xi},\tau)}(\boldsymbol{\nu})\right]\delta(\boldsymbol{\eta}-\boldsymbol{\xi})d\Sigma(\boldsymbol{\xi})\right\}dV(\boldsymbol{\eta})\\
&= \int_{-\infty}^{\infty} d\tau \int\int\int_V G_{in}(\boldsymbol{\xi},\tau-t;\boldsymbol{x},0)f_i^{[\boldsymbol{T}]}(\boldsymbol{\eta},\tau)dV(\boldsymbol{\eta})
\end{aligned}
\tag{B.69}
$$

where

$$
\boxed{f_i^{[\boldsymbol{T}]} = \int\int_\Sigma \left[T_i^{(\boldsymbol{u}(\boldsymbol{\xi},\tau)}(\boldsymbol{\nu})\right]\delta(\boldsymbol{\eta}-\boldsymbol{\xi})d\Sigma(\boldsymbol{\xi})} \tag{B.70}
$$

with the dimension of volume force density, i.e. $\frac{\text{force}}{\text{volume}}$, is *equivalent body force field for traction discontinuity.* This is a non-real force field which will produce displacement field equal to the displacement field of the actual traction discontinuity.

B.3.2 Body Force Equivalent to Displacement Discontinuity

The same method is applied to the case of displacement discontinuity. From eq. (B.66):

$$u_n^{[\boldsymbol{U}]}(\boldsymbol{x},t) = -A\int_{-\infty}^{\infty} d\tau \int\!\!\int_{\Sigma} [u_i(\boldsymbol{\xi},t)]\, c_{ijkl}(\boldsymbol{\xi})\nu_j(\boldsymbol{\xi})G_{kn,l}(\boldsymbol{\xi},\tau-t;\boldsymbol{x},0)d\Sigma(\boldsymbol{\xi})\ . \tag{B.71}$$

Using the three dimensional delta function with the physical dimension $\frac{1}{\text{volume}}$ we can write:

$$G_{kn}(\boldsymbol{\xi},\tau-t;\boldsymbol{x},0) = \int\!\!\int\!\!\int_V G_{kn}(\boldsymbol{\eta},\tau-t;\boldsymbol{x},0)\delta(\boldsymbol{\eta}-\boldsymbol{\xi})dV(\boldsymbol{\eta})\ . \tag{B.72}$$

Therefore:

$$\frac{\partial}{\partial\xi_l}G_{kn}(\boldsymbol{\eta},\tau-t;\boldsymbol{x},0) = \frac{\partial}{\partial\xi_l}\left\{\int\!\!\int\!\!\int_V G_{kn}(\boldsymbol{\eta},\tau-t;\boldsymbol{x},0)\delta(\boldsymbol{\eta}-\boldsymbol{\xi})dV(\boldsymbol{\eta})\right\}\ . \tag{B.73}$$

Since G_{kn} is no longer a function of $\boldsymbol{\xi}$:

$$\frac{\partial}{\partial\xi_l}G_{kn}(\boldsymbol{\xi},\tau-t;\boldsymbol{x},0) = \left[\int\!\!\int\!\!\int_V G_{kn}(\boldsymbol{\eta},\tau-t;\boldsymbol{x},0)\frac{\partial}{\partial\xi_l}\delta(\boldsymbol{\eta}-\boldsymbol{\xi})dV(\boldsymbol{\eta})\right]\ . \tag{B.74}$$

In virtue of

$$\frac{\partial}{\partial\xi_l}\delta(\boldsymbol{\eta}-\boldsymbol{\xi}) = -\frac{\partial}{\partial\eta_l}\delta(\boldsymbol{\eta}-\boldsymbol{\xi})\ , \tag{B.75}$$

we can write eq. (B.73) as:

$$\frac{\partial}{\partial\xi_l}G_{kn}(\boldsymbol{\xi},\tau-t;\boldsymbol{x},0) = -\int\!\!\int\!\!\int_V G_{kn}(\boldsymbol{\eta},\tau-t;\boldsymbol{x},0)\frac{\partial}{\partial\eta_l}\delta(\boldsymbol{\eta}-\boldsymbol{\xi})dV(\boldsymbol{\eta})\ . \tag{B.76}$$

Therefore, eq. (B.71) yields:

$$\begin{aligned} u_n^{[\boldsymbol{U}]}(\boldsymbol{x},t) &= \\ = -A\int_{-\infty}^{\infty} d\tau \int\!\!\int_{\Sigma} [u_i(\boldsymbol{\xi},\tau)]\, c_{ijkl}(\boldsymbol{\eta})\nu_j(\boldsymbol{\xi}) &\left\{-\int\!\!\int\!\!\int_V G_{kn}(\boldsymbol{\eta},\tau-t;\boldsymbol{x},0)\frac{\partial}{\partial\eta_l}\delta(\boldsymbol{\eta}-\boldsymbol{\xi})dV(\boldsymbol{\eta})\right\}d\Sigma(\boldsymbol{\xi})\ . \end{aligned} \tag{B.77}$$

Again with Fubini's theory [Fubini, 1983]:

$$\begin{aligned} u_n^{[\boldsymbol{U}]}(\boldsymbol{x},t) = \int_{-\infty}^{\infty} d\tau \int\!\!\int\!\!\int_V &\left\{\int\!\!\int_{\Sigma} [u_i(\boldsymbol{\xi},\tau)]\, c_{ijpq}(\boldsymbol{\xi})\nu_j(\boldsymbol{\xi})\frac{\partial}{\partial\eta_l}\delta(\boldsymbol{\eta}-\boldsymbol{\xi})d\Sigma(\boldsymbol{\xi})\right\} \\ &\times G_{kn}(\boldsymbol{\eta},\tau-t;\boldsymbol{x},0)dV(\boldsymbol{\eta})\ . \end{aligned} \tag{B.78}$$

Therefore, the *body force equivalent for a displacement discontinuity* is:

$$\boxed{f_i^{[\boldsymbol{U}]}(\boldsymbol{\eta},\tau) = A\int\!\!\int_{\Sigma} [u_i(\boldsymbol{\xi},\tau)]\, c_{ijpq}(\boldsymbol{\xi})\nu_j(\boldsymbol{\xi})\frac{\partial}{\partial\eta_l}\delta(\boldsymbol{\eta}-\boldsymbol{\xi})d\Sigma(\boldsymbol{\xi})}\ . \tag{B.79}$$

B.4 VOLUME SOURCES

When the source is not a point, but a volume, and to each element of the volume a time varying force is applied, then the generated displacement field is the summation of all the displacement fields due to the forces applied at different volume elements and different instants of time. Therefore for an incompressible earth with homogeneous boundary conditions, without discontinuity surfaces and with quiescent past, the displacement field of a volume source is represented by eq. (B.41):

$$u_n(\boldsymbol{x},t) = \int_{-\infty}^{\infty} d\tau \int\!\!\int\!\!\int_V G_{in}(\boldsymbol{\xi},\tau;\boldsymbol{x},t)f_i(\boldsymbol{\xi},\tau)dV\ . \tag{B.80}$$

One way to solve for such a displacement field is suggested by Eshelby [1957] and is described by [Aki and Richards, 1980]. Although volume sources are not considered in the present study, the description is rewritten in the following in order to complete this chapter:

> Let us illustrate this concept by a set of imaginary cutting, straining, and welding operations described by Eshelby [1957]. First we separate the source material by cutting along the surface Σ enclosing it and removing the source volume (the *inclusion*) from its surrounding (the *matrix*). At this stage, we suppose that the material removed is held in its original shape by tractions having the same volume over Σ as the tractions imposed across Σ by the matrix before the cutting operation. Second, we let the source material undergo transformational strain Δe_{rs}. By this, we mean that Δe_{rs} occurs without changing the stress within the inclusion, *stress-free strain.* It is this strain that characterizes the seismic source. .... Third, we apply extra surface tractions that will restore the source volume to its original shape: this will result in an additional stress field $-c_{pqrs}\Delta e_{rs} = -\Delta\tau_{pq}$ throughout the inclusion, and the additional tractions applied on its surface Σ are $-c_{pqrs}\Delta e_{rs}\nu_q$, where ν_q is the outward normal on Σ. Since $\Delta\tau_{pq}$ is a static field, $\Delta\tau_{pq,q} = 0$. The stress in the matrix is still unchanged, being held at its original value by tractions imposed across the internal surface Σ, and having the same value as tractions imposed on the matrix by the inclusion before it was cut out. Fourth, we put the inclusion back in its hole (which is exactly the correct shape) and weld the material across the cut. The traction on Σ^- is now an amount $-c_{pqrs}\Delta e_{rs}\nu_q$ greater than that on Σ^+, leading to a traction discontinuity (in the $\boldsymbol{\nu}$ direction) of amount $+c_{pqrs}\Delta e_{rs}\nu_q$. This traction is due to applied surface forces that are external to the source and which act on the inclusion to maintain its correct shape. Fifth, we release the applied surface forces over Σ^-. Since tractions is actually continuous across Σ, this amount to imposing an apparent traction discontinuity of $-(c_{pqrs}\Delta e_{rs})\nu_q$. The elastic field produced in the matrix by the whole process is that due to apparent tractions discontinuity across Σ.

The displacement field is given as for traction discontinuity, i.e. eq. (B.51) with $[T_p] = -(c_{pqrs})\Delta e_{rs}\nu_q$:

$$u_n(\boldsymbol{x}) = \int_{-\infty}^{\infty} \int \int_{-\Sigma} c_{pqrs}\Delta e_{rs}\nu_q G_{np}(\boldsymbol{\xi}, \tau - t; \boldsymbol{x}, 0) d\Sigma(\boldsymbol{\xi}) \ . \tag{B.81}$$

If the integrand and its derivatives with respect to $\boldsymbol{\xi}$ are continuous, we can apply Gauss theorem to obtain:

$$\boxed{u_n(\boldsymbol{x}) = \int_{-\infty}^{\infty} d\tau \int \int \int_V \frac{\partial}{\partial \xi_q} \left[c_{pqrs}\Delta e_{rs}\nu_q G_{np}(\boldsymbol{\xi}, \tau - t; \boldsymbol{x}, 0)\right] dV(\boldsymbol{\xi})} \ . \tag{B.82}$$

B.5 DESCRIPTION IN TEMRS OF MOMENTS

So far, we have discussed point sources, and their displacement fields as Green's functions. Here we continue with a special combination of two point sources, i.e. a *dipolar source*, and its Green's function.

B.5.1 Dipolar Source

One important combination of two concentrated forces in earthquake analysis is a *dipolar source.*

Suppose that two concentrated forces of the same magnitude f in opposite directions denoted by the unit vectors $\boldsymbol{a}$ and $-\boldsymbol{a}$ are applied at the same time τ at two points, each $\frac{\epsilon}{2}$ distant from $\boldsymbol{r}_0$ in the directions $\boldsymbol{\nu}$ and $-\boldsymbol{\nu}$ (figure B.2). Such a source is called *double force* and its displacement field is the vector addition of displacement fields of the two concentrated forces [Aki and Richards, 1980]. Ben-Menahem and Singh [1981]:

$$\boldsymbol{u}(\boldsymbol{x}, t) = A\boldsymbol{f}.\left[\boldsymbol{G}(\boldsymbol{x}, t; \boldsymbol{r}_0 + \frac{\epsilon}{2}\boldsymbol{\nu}, \tau) - \boldsymbol{G}(\boldsymbol{x}, t; \boldsymbol{r}_0 - \frac{\epsilon}{2}\boldsymbol{\nu}, \tau)\right] \tag{B.83}$$

or

$$u_i(\boldsymbol{x}, t) = Af_j\left[G_{ij}(\boldsymbol{x}, t; \boldsymbol{r}_0 + \frac{\epsilon}{2}\boldsymbol{\nu}, \tau) - G_{ij}(\boldsymbol{x}, t; \boldsymbol{r}_0 - \frac{\epsilon}{2}\boldsymbol{\nu}, \tau)\right] \ . \tag{B.84}$$

In the limiting case of $\epsilon \longrightarrow 0$, we can write the displacement field as:

$$u_i(\boldsymbol{x}, t) = Af_j \nabla_{r_0} G_{ij}(\boldsymbol{x}, t; \boldsymbol{r}_0, \tau).\epsilon\boldsymbol{\nu} \tag{B.85}$$

in which ∇_{r_0} represents gradient with respect to the $\boldsymbol{r}_0$ components, i.e.:

$$u_i(\boldsymbol{x}, t) = A\epsilon f_j \frac{\partial G_{ij}}{\partial q_k}(\boldsymbol{x}, t; \boldsymbol{r}_0, \tau)\boldsymbol{e}_k.\boldsymbol{\nu} = A\epsilon f_j \frac{\partial G_{ij}}{\partial q_k} \ . \tag{B.86}$$

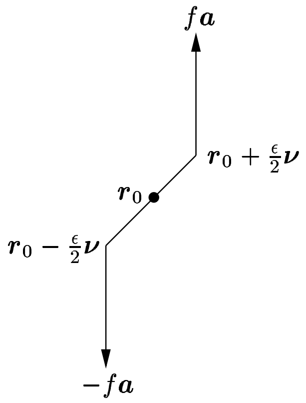

Figure B.2: A double force

If at the same time as $\epsilon \longrightarrow 0$, also $f \longrightarrow \infty$ so that $\epsilon f_j \longrightarrow F_j$, then:

$$u_i(\boldsymbol{x}, t) = AF_j \frac{\partial G_{ij}}{\partial q_k} \nu_k \ . \tag{B.87}$$

The derivative in the above formula is defined by:

$$\frac{\partial G_{ij}}{\partial q_k} := \lim_{\Delta q_k \to 0} \frac{G_{ij}(\boldsymbol{x}, t; \boldsymbol{r}_0 + \frac{\Delta q_k}{2}\boldsymbol{e}_k, \tau) - G_{ij}(\boldsymbol{x}, t; \boldsymbol{r}_0 - \frac{\Delta q_k}{2}\boldsymbol{e}_k, \tau)}{\Delta q_k} \ . \tag{B.88}$$

The denominator of the last fraction gives the effect of a force couple applied at $(\boldsymbol{r}_0, \tau)$. Therefore the displacement at $(\boldsymbol{x}, t)$ is a summation of nine different double forces at $(\boldsymbol{r}_0, \tau)$. According to the relative directions of $\boldsymbol{a}$ and $\boldsymbol{\nu}$, two special cases are distinguished (figure B.3):

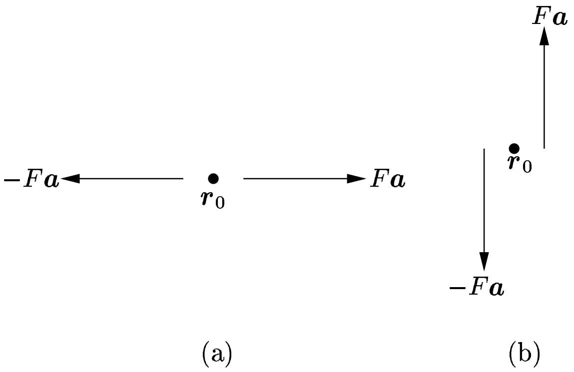

Figure B.3: (a) Dipole, and (b) single couple

1. If $\boldsymbol{a}$ is parallel to $\boldsymbol{\nu}$, i.e. the forces lie on the line of separation, the source is called a *dipole.*
2. If $\boldsymbol{a}$ is orthogonal to $\boldsymbol{\nu}$, i.e. the forces are perpendicular to the line of separation, the source is called a *single couple.*

Having defined a Cartesian coordinate system, three different directions of the forces and three different directions of separation give rise to nine possibilities: three dipoles and six single couples in the coordinate directions (figure B.4).

The single couple (i, j); i.e. $i \neq j$, exerts a torque in the direction $\pm k$ on the medium. The single couple (i, j) exerts another torque in the direction $\mp k$. This means that having the six single couples with equal magnitudes, the total implied rotational motion vanishes.

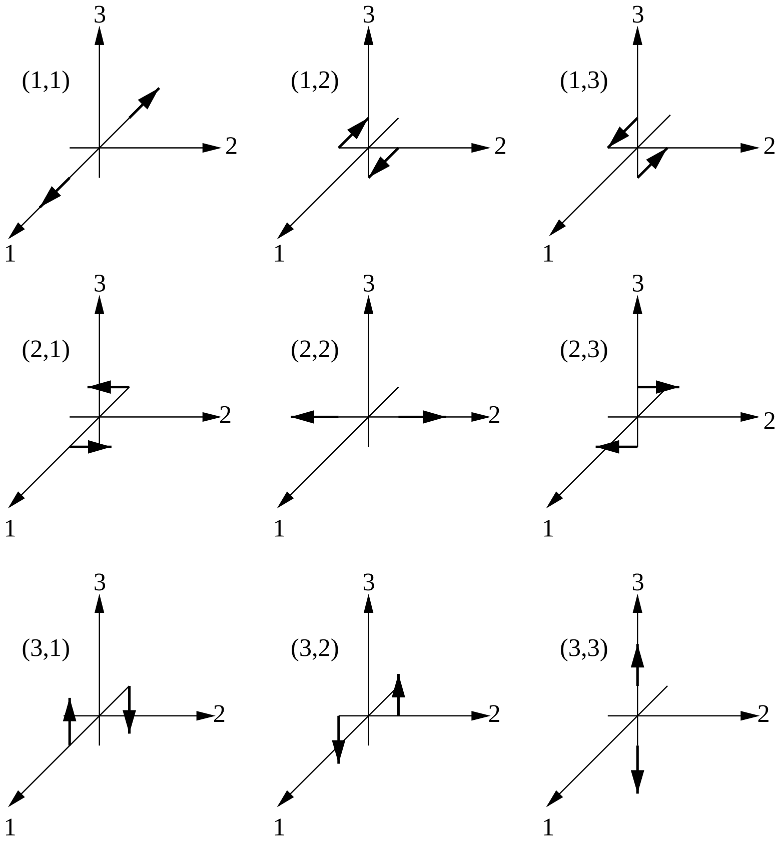

Figure B.4: Dipoles and single couples along Cartesian coordinate axes.

B.5.2 Description by Moments

From eq. (B.71) and for the displacement field associated with a displacement discontinuity in an incompressible material with homogeneous boundary conditions we can write:

$$u_n(\boldsymbol{x},t) = A\int_{-\infty}^{\infty} d\tau \int\int_{\Sigma} [u_i(\boldsymbol{\xi},\tau)]\, c_{ijkl}(\boldsymbol{\xi})\nu_j(\boldsymbol{\xi})G_{kn,l}(\boldsymbol{\xi},\tau-t;\boldsymbol{x},0)d\Sigma(\boldsymbol{\xi}) \tag{B.89}$$

or, using the convolution symbol (eq. B.42) in brief notation:

$$u_n(\boldsymbol{x},t) = A\int\int_{\Sigma} [u_i(\boldsymbol{\xi},\tau)]\, c_{ijkl}\nu_j \star \frac{\partial G_{kn}}{\partial \xi_l} d\Sigma\ . \tag{B.90}$$

G_{kn} in this formula expresses the effect of the k-component of the displacement discontinuity at $\boldsymbol{\xi}$ on the n-component of the displacement at $\boldsymbol{x}$. $\partial G_{kn}/\partial\xi_l$ can be interpreted physically as a single couple with the arm in l-direction. Therefore the summation over l and integration on Σ means that the displacement at $(\boldsymbol{x},t)$ is the effect of the distributed couples on Σ.

$[u_i]\,\nu_j c_{ijkl}$ is the strength of the (k,l) couple with the dimension moment per unit area. Therefore:

$$\boxed{\boldsymbol{m} := [u_i]\,\nu_j c_{ijkl}\boldsymbol{e}_k \otimes \boldsymbol{e}_l} \tag{B.91}$$

is called *moment density tensor*. With this, eq. (B.90) takes the form:

$$u_n(\boldsymbol{x},t) = A\int\int_{\Sigma} m_{kl} \star G_{kn,l} d\Sigma\ . \tag{B.92}$$

Sufficiently far from Σ, it can be regarded as an effective point and we can define the *moment tensor* by:

$$\boxed{\boldsymbol{M} := \int\int_{\Sigma} m_{kl} d\Sigma(\boldsymbol{e}_k \otimes \boldsymbol{e}_l)}\ . \tag{B.93}$$

With this, eq. (B.92) reduces to

$$\boxed{u_n(\boldsymbol{x},t) = AM_{kl}(\boldsymbol{\xi},\tau) \star G_{kn,l}(\boldsymbol{\xi},\tau;\boldsymbol{x},t)}\ . \tag{B.94}$$

The last equation is very important in seismology and the representation of seismic source displacement fields.

B.5.3 Simplified Examples of Buried Faults

At the end of this appendix some examples of slip across a buried fault are considered.

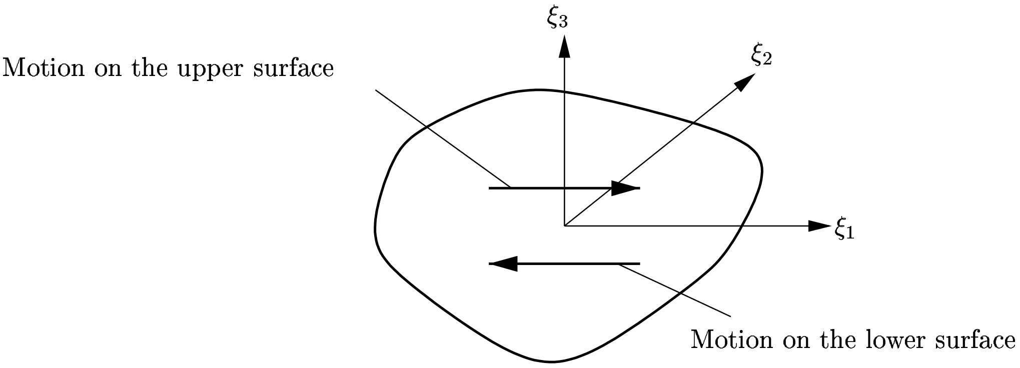

Figure B.5: A simple example of a buried fault normal to the ξ_3 axis with slip parallel to the axis $\xi_1$axis.

A buried fault may be regarded as an internal displacement discontinuity. In this section the moment density tensor of such a fault is computed for an incompressible, isotropic, homogeneous earth. In the following, the moment density tensor elements are referred to the point of fracture, i.e. $(\boldsymbol{\xi},\tau)$.

For this simplified earth, the elastic constants are evaluated from eq. (A.63). Then the moment density tensor elements from eq. (B.91) are:

$$\begin{aligned} m_{pq} &= [u_i]\,\nu_j\,\{\lambda\delta_{ij}\delta_{pq} + \mu(\delta_{ip}\delta_{jq} + \delta_{iq}\delta_{jp})\} \\ &= \lambda\,(\nu_j\delta_{ij})\,[u_i] + \mu\,(\nu_j\delta_{jq})\,([u_i]\,\delta_{ip}) + \mu\,(\nu_j\delta_{jp})\,([u_i]\,\delta_{iq}) \\ &= \lambda\nu_i\,[u_i] + \mu\nu_q\,[u_p] + \mu\nu_p\,[u_q]\ . \end{aligned} \tag{B.95}$$

On account of the properties of δ_{ij}, this reduces to

$$\boxed{m_{pq} = \lambda\nu_i\,[u_i]\,\delta_{pq} + \mu\,(\nu_q\,[u_p] + \nu_p\,[u_q])}\ . \tag{B.96}$$

If the slip occurs on the plane of Σ, $\boldsymbol{\nu} \perp [\boldsymbol{u}]$ and

$$\nu_i\,[u_i] = 0\ , \tag{B.97}$$

and eq. (B.96) reduces to

$$m_{pq} = \mu\,(\nu_q\,[u_p] + \nu_p\,[u_q])\ . \tag{B.98}$$

If the slip happens to be along a coordinate axis (figure B.5), the moment density tensor is further reduced. For example, if the slip is parallel to the ξ_3 coordinate axis, then $[u_2] = [u_3] = 0$, with the third axis normal to the fault plane $\nu_1 = \nu_2 = 0$, we then obtain:

$$\boldsymbol{m} = \begin{bmatrix} 0 & 0 & \mu\,[u_1] \\ 0 & 0 & 0 \\ \mu\,[u_1] & 0 & 0 \end{bmatrix}\ . \tag{B.99}$$

Appendix C

ELEMENTS OF VISCOELASTICITY THEORY

Sofar, we have described elastic materials. However there are many materials which do not obey the elasticity laws. Sometimes, the deformations take place gradually after the application of a force field. It may also happen that the body is deformed suddenly, but the deformations continue and are not recovered after the removal of the applied force field. Viscoelasticity is one proper theory to study the behaviour of one class of such materials.

This appendix briefly presents the basic idea of viscoelasticity theory and concentrates on the type of viscoelasticity most common in the earth deformations studies, i.e. the Maxwell fluid. We begin with the concepts for one dimension, i.e. uni-axial extension, and continue with the generalizations for three dimensions. The discussion is confined to infinitesimal deformation, therefore the non-deformed and deformed coordinate frames are not distinguished.

C.1 BASIC ELEMENTS

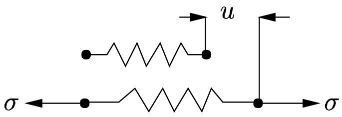

Figure C.1: Helical spring represents elastic behaviour

A helical spring (figure C.1) is the basic element representing elastic deformations. Deformations (extension and contraction) happen simultaneously with the action of forces. This behaviour is presented by eq. (A.2) and is the subject of appendix B.

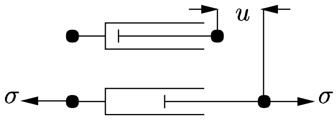

Figure C.2: Dashpot represents viscous behaviour

The basic element which represents viscous behaviour is the dashpot of figure C.2. In this model it is not the elongation which is proportion to the applied stress, but it is its time derivative:

$$\sigma = F\dot{\epsilon} \ , \tag{C.1}$$

where dot denotes the time derivative. $\dot{\epsilon}$ is called *strain rate*, and the material whose deformations follow eq. (C.1) is known as *viscous material.*

C.2 VISCOELASTIC BEHAVIOUR

Viscoelastic behaviour is a combination of the elastic behaviour of the spring element and the viscous behaviour of the dashpot. Different viscoelastic materials are defined, depending on whether the spring and dashpot are coupled parallel or in series and how many basic elements are coupled.

C.2.1 Maxwell Fluid

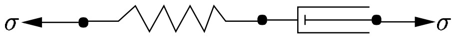

Figure C.3: Maxwell fluid

The first viscoelastic model combines a spring and a dashpot in series (figure C.3). The applied stress at the two elements are equal

$$\sigma_d = \sigma_s = \sigma \ , \tag{C.2}$$

but the total strain is the sum of the initial strains:

$$\epsilon = \epsilon_s + \epsilon_d \ , \tag{C.3}$$

where indices s and d refer to spring and dashpot respectively.

According to the assumed constitutive equation of the spring, i.e. linear elasticity, and the dashpot, i.e. viscosity, we may write:

$$\sigma = \sigma_s = E\epsilon_s \tag{C.4}$$

where E and ϵ_s are Young's modulus and infinitesimal strain in spring respectively, and

$$\sigma = \sigma_d = F\dot{\epsilon}_d \ , \tag{C.5}$$

where F and $\dot{\epsilon}_d$ are the viscosity and strain rate of the dashpot, respectively.

From eq. (C.1):

$$\dot{\epsilon}_s = \frac{\dot{\sigma}}{E} \tag{C.6}$$

and from eq. (C.5):

$$\dot{\epsilon}_d = \frac{\sigma}{F} \ . \tag{C.7}$$

Eqs. (C.3), (C.6) and (C.7) yield:

$$\dot{\epsilon} = \frac{\sigma}{F} + \frac{\dot{\sigma}}{E} \tag{C.8}$$

which is the constitutive equation of a Maxwell fluid. An alternative form is:

$$\sigma + p_1\dot{\sigma} = q_1\dot{\epsilon} \ , \tag{C.9}$$

with:

$$p_1 = \frac{F}{E} \ , \tag{C.10}$$

$$q_1 = F \ . \tag{C.11}$$

In order to study the behaviour of a Maxwell fluid, we subject it to a two step test [Flügge, 1975].

Step 1: Creep Phase: In the first step a constant stress$\sigma = \sigma_0$ is applied at instant $t = 0$, and eq. (C.9) is solved for $\epsilon(t)$. The general solution of the differential equation (C.9) is:

$$\epsilon(t) = \frac{\sigma_0}{q_1}t + C_1 \ ; \ t > 0 \ . \tag{C.12}$$

The initial condition of applying σ_0 at t implies that

$$\lim_{\tau\to 0}\int_{-\tau}^{\tau} \sigma dt = 0 \ , \tag{C.13}$$

but

$$\lim_{\tau\to 0} \dot{\sigma}(\tau) = \sigma_0 \ . \tag{C.14}$$

Eqs. (C.13) and (C.14) allow us to integrate both sides of eq. (C.9) as $\tau \to 0$, which yields:

$$p_1\sigma_0 = q_1\epsilon_0 \ . \tag{C.15}$$

With eqs. (C.9) and (C.10) we thus obtain:

$$\epsilon_0 = \frac{p_1}{q_1}\sigma_0 = \frac{\sigma_0}{E} \ , \tag{C.16}$$

where ϵ_0 is the strain value at 0^+time immediately after the application of σ_0. Substituting this into eq. (C.12) for $t = 0^+$yields:

$$\epsilon_0 = C_1 = \frac{p_1}{q_1}\sigma_0 \ . \tag{C.17}$$

Therefore, from eq. (C.12):

$$\epsilon(t) = \frac{\sigma_0}{q_1}t + \frac{p_1}{q_1}\sigma_0 = (t + p_1)\frac{\sigma_0}{q_1} \ . \tag{C.18}$$

The creep phase of the test is shown in the time interval $0 < t < t_1$ of figure (C.4).

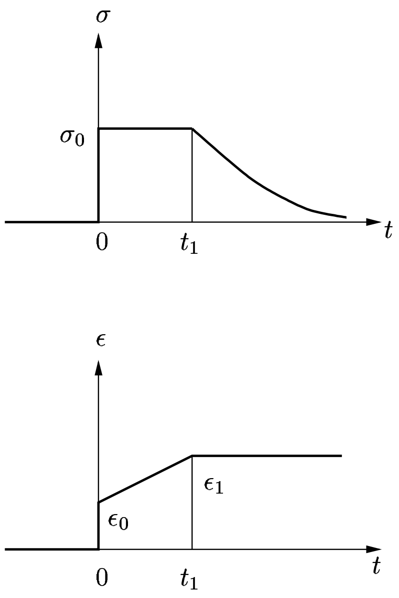

Figure C.4: The two step test for a Maxwell fluid

Step 2: Relaxation Phase: In the second step the stress is considered while the strain is kept constant for $t > t_1$:

$$\epsilon(t) = \epsilon(t_1) = \epsilon_1 \ ; \ t > t_1 \ . \tag{C.19}$$

Eq. (C.9) turns to:

$$\sigma + p_1\dot{\sigma} = 0 \tag{C.20}$$

which is a homogeneous first order differential equation with the general solution:

$$\sigma(t) = C_2 e^{-\frac{t}{p_1}} \ , \ t > t_1 \ . \tag{C.21}$$

The initial condition for $t = t_1$ is:

$$\sigma(t_1) = \sigma_0 \ . \tag{C.22}$$

With this we obtain from eq. (C.21):

$$\sigma_0 = C_2 e^{-\frac{t_1}{p_1}} \ , \tag{C.23}$$

$$C_2 = \sigma_0 e^{-\frac{t_1}{p_1}} \ , \tag{C.24}$$

$$\sigma(t) = \sigma_0 e^{-\frac{t-t_1}{p_1}} \ . \tag{C.25}$$

This phase is shown in figure C.4 for $t > t_1$.

C.2.2 Kelvin Solid

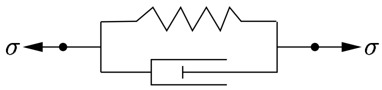

Figure C.5: Kelvin Solid

The second simple viscoelastic model is a parallel combination of spring and dashpot elements (figure C.5). In this model strain is equal at both elements:

$$\epsilon = \epsilon_s = \epsilon_d \ , \tag{C.26}$$

but the total stress is distributed over the two elements:

$$\sigma = \sigma_s + \sigma_d \ . \tag{C.27}$$

Again linear elasticity of the spring and viscosity of the dashpot imply, respectively:

$$\sigma_s = E\epsilon \ , \tag{C.28}$$

$$\sigma_d = F\dot{\epsilon} \ . \tag{C.29}$$

From eq. (C.27):

$$\sigma = E\epsilon + F\dot{\epsilon} \tag{C.30}$$

or

$$\sigma = q_0\epsilon + q_1\dot{\epsilon} \ , \tag{C.31}$$

where:

$$q_0 = E \ . \tag{C.32}$$

$$q_1 = F \ . \tag{C.33}$$

To discuss the behavior of a Kelvin material, the two step test is applied again [Flügge, 1975].

Step 1: Creep Phase: Constant stress $\sigma = \sigma_0$ is applied at $t = 0$ and eq. (C.31) is solved for $\epsilon(t)$:

$$\epsilon(t) = \frac{\sigma_0}{q_0} + C_1 e^{-\lambda t} \ ; \ \lambda = \frac{q_0}{q_1} \ . \tag{C.34}$$

Although σ jumps from 0 to σ_0 at $t = 0$, it remains finite and therefore $\dot{\epsilon}$ should remain finite too. This means that:

$$\epsilon(0^+) = \epsilon(0^-) = 0 \ . \tag{C.35}$$

Therefore:

$$\epsilon(0) = \frac{\sigma_0}{q_0} + C_1 = 0 \ , \tag{C.36}$$

which leads to

$$C_1 = -\frac{\sigma_0}{q_0} \ , \tag{C.37}$$

$$\epsilon(t) = \frac{\sigma_0}{q_0}(1 - e^{-\lambda t}) \ . \tag{C.38}$$

This creep phase is depicted in the time interval $0 < t < t_1$ of figure (C.6).

Step 2: Relaxation Phase: In this phase the strain is kept constant:

$$\epsilon(t) = \epsilon_1 = const. \ ; \ t > t_1 \ . \tag{C.39}$$

Then from eq. (C.31):

$$\sigma(t) = q_0\epsilon_1 \ , \tag{C.40}$$

which means that when strain is fixed, stress does not change either.

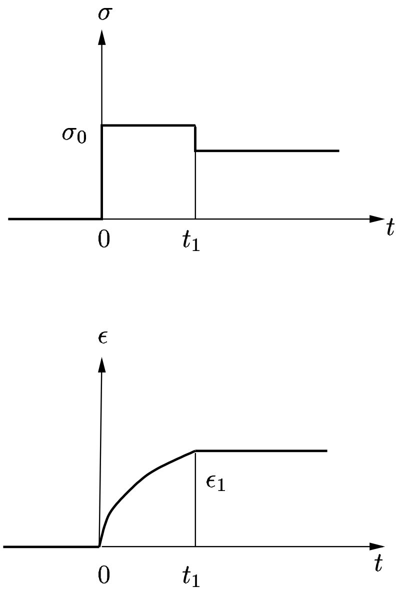

Figure C.6: The two step test of Kelvin material

C.2.3 More Complicated Materials

The possibility of combining the basic elements spring and dashpot is not confined to the two parameter Maxwell and Kelvin models. There may be more than one of each element type and they may be combined in different ways, parallel or series. A few of them are mentioned without detailed discussion. This will be useful when later, considering the solution method.

C.2.3.1 Three-parameter solid

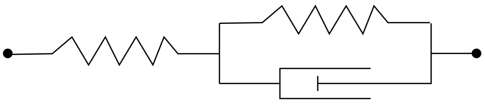

Figure C.7: Three-parameter solid

The three-parameter solid of figure (C.7) is described by the constitutive equation:

$$\sigma + p_1\dot{\sigma} = q_0\epsilon + q_1\dot{\epsilon}\ . \tag{C.41}$$

C.2.3.2 Three-parameter fluid

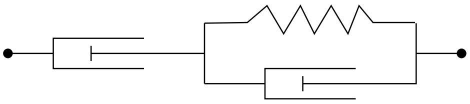

Figure C.8: Three-parameter fluid

The other three-parameter model is the fluid of figure (C.8). This type of material is described by the constitutive equation:

$$\sigma + p_1\dot{\sigma} = q_1\dot{\epsilon} + q_2\ddot{\epsilon} \tag{C.42}$$

C.2.3.3 Four-parameter solid

The following equation describes the constitutive behavior of a four-parameter solid (figure C.9):

$$\sigma + p_1\dot{\sigma} = q_0\epsilon + q_1\dot{\epsilon} + q_2\ddot{\epsilon}\ . \tag{C.43}$$

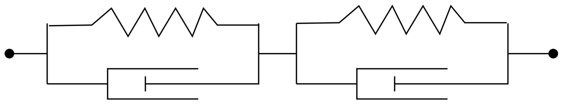

Figure C.9: Four-parameter solid

C.2.3.4 Four-parameter fluid

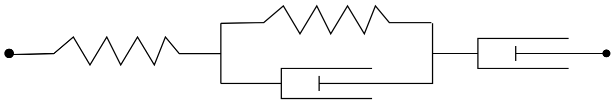

Figure C.10: Four-parameter fluid

The last material we introduce here is the four-parameter fluid of figure (C.10).The constitutive equation of this model is:

$$\sigma + p_1\dot{\sigma} + p_2\ddot{\epsilon} = q_1\dot{\epsilon} + q_2\ddot{\epsilon} \ . \tag{C.44}$$

C.2.4 General Material

The behavior of a general viscoelastic material could be specified as follows:

$$\sum_{k=0}^{n} p_k \frac{d^k\sigma}{dt^k} = \sum_{k=0}^{m} q_k \frac{d^k\epsilon}{dt^k} \tag{C.45}$$

or in a shorter notation:

$$\boldsymbol{P}\sigma = \boldsymbol{Q}\epsilon \ . \tag{C.46}$$

Here $\boldsymbol{P}$ and $\boldsymbol{Q}$ are differential operators defined by:

$$\boldsymbol{P} := \left[1 + \frac{d}{dt} + \frac{d^2}{dt^2} + \cdots + \frac{d^n}{dt^n}\right] \ , \tag{C.47}$$

$$\boldsymbol{Q} := \left[1 + \frac{d}{dt} + \frac{d^2}{dt^2} + \cdots + \frac{d^m}{dt^m}\right] \ . \tag{C.48}$$

C.3 SOLUTION TECHNIQUE

In order to solve eq. (C.45) or (C.46), we define two new functions related to the creep and relaxation phases of the standard test of sections §C.2.1 and §C.2.2.

In the creep phase we apply a constant stress σ_0 during the period $0 < t < t_1$. Since we consider only linear materials, strain and stress are proportional at any time, while the proportionality factor can change in time due to viscous behavior:

$$\epsilon(t) = \sigma_0 J(t) \ . \tag{C.49}$$

The function $J(t)$, which is equal to strain per unit stress, is known as *creep compliance* and defines the motion of the linear viscoelastic material in the creep phase.

During the relaxation phase, $t > t_1$, strain is kept constant. Similarly, because of the linearity of the material response and the viscous part of the behavior:

$$\sigma(t) = \epsilon_1 Y(t) \ . \tag{C.50}$$

The function $Y(t)$, which defines the stress per unit strain, is called *relaxation function* and expresses the material behavior in the relaxation phase. Creep and relaxation functions are related to each other. In order to find this relation, we consider their Laplace transformations with respect to time [Kreyszig, 1993].

The differential operators $\boldsymbol{P}$ and $\boldsymbol{Q}$ of eqs. (C.47) and (C.48) are first transformed to the Laplace domain. Assuming that the time derivatives of σ and ϵ are zero at $t = 0^-$, follows that:

$$\mathcal{L}\left\{\sigma + \frac{d\sigma}{dt} + \frac{d^2\sigma}{dt^2} + \cdots + \frac{d^n\sigma}{dt^n}\right\} = \left(1 + s + s^2 + \cdots + s^n\right)\bar{\sigma} \ , \tag{C.51}$$

where $\mathcal{L}\{.\}$ denotes Laplace transformation and $\bar{\sigma} := \mathcal{L}\{\sigma\}$. The last result states that:

$$\mathcal{L}\{\boldsymbol{P}\} = \mathcal{P}(s) = 1 + s + s^2 + \cdots + s^n \ . \tag{C.52}$$

By the same reasoning it follows that:

$$\mathcal{L}\{\boldsymbol{Q}\} = \mathcal{Q}(s) = 1 + s + s^2 + \cdots + s^m \ , \tag{C.53}$$

such that the differential equation (C.45) is transformed into the following algebraic equation:

$$\mathcal{P}(s)\bar{\sigma} = \mathcal{Q}(s)\bar{\epsilon} \ . \tag{C.54}$$

This equation is very similar to the generalized Hooke's law in elasticity theory (eq. A.59). This is the foundation of the *correspondence principle* of elasticity.

This principle of viscoelasticity states that of an elastic problem is known, the Laplace transform of the solution to the corresponding viscoelastic problem may be found by a similar equation in the Laplace domain.

Assuming a unit constant stress in the creep phase, eq. (C.49) becomes:

$$\epsilon(t) = J(t) \tag{C.55}$$

or in the Laplace transform domain:

$$\bar{\epsilon}(s) = \bar{J}(s) \ . \tag{C.56}$$

Comparison of the last equation with eq. (C.54) yields:

$$\bar{J}(s) = \frac{\mathcal{P}(s)}{s\mathcal{Q}(s)} \ . \tag{C.57}$$

In a similar way it follows:

$$\bar{Y}(t) = \frac{\mathcal{Q}(s)}{s\mathcal{P}(s)} \ . \tag{C.58}$$

Combining the last two equations, we obtain:

$$\boxed{\bar{J}(s)\bar{Y}(s) = \frac{1}{s^2}} \tag{C.59}$$

which shows that if any of the two functions, creep compliance or relaxation function, is known, the other one can be obtained in Laplace domain. This in turn implies that either of the two functions is sufficient to uniquely determine the linear viscoelastic behavior.

C.4 GENERALIZATION TO THREE DIMENSIONS

The one dimensional model of §C.2 forms the basic theory of viscoelasticity theory. In order to solve the final equations for any material in three dimensional space, we need to generalize these tools to three dimensions.

In the three dimensional physical space, we take advantage of the same mathematical tools as we discussed in case of three dimensional elastic bodies, i.e. stress and strain tensors (§A.2). The tensors, this time to be used in viscoelastic models, are manipulated so that they can be used in the general viscoelastic eq. (C.48) and its Laplace transforms, eqs. (C.51) and (C.53).

In three dimensions, instead of only extension or contraction, also hydrostatic pressure, dilatation and shear parts must be considered as discussed in §A.2. We decompose the stress and strain tensors into two parts.

The stress tensor can be split into spherical (hydrostatic) and deviatoric (shear) parts as follows:

$$\boldsymbol{\sigma} = \begin{bmatrix} \sigma_{11} & \sigma_{12} & \sigma_{13} \\ \sigma_{21} & \sigma_{22} & \sigma_{23} \\ \sigma_{31} & \sigma_{32} & \sigma_{33} \end{bmatrix} = \frac{1}{3}\sigma_{ii}\boldsymbol{I} + \frac{1}{3}\begin{bmatrix} 2\sigma_{11} - \sigma_{22} - \sigma_{33} & \sigma_{12} & \sigma_{13} \\ \sigma_{21} & -\sigma_{11} + 2\sigma_{22} - \sigma_{33} & \sigma_{23} \\ \sigma_{31} & \sigma_{32} & -\sigma_{11} - \sigma_{22} + 2\sigma_{33} \end{bmatrix} . \tag{C.60}$$

The first term on the right hand side is a diagonal matrix with equal diagonal elements, which specifies a hydrostatic stress field while the second term is a symmetric tensor with zero trace, i.e. shear stresses only. We show this separation by:

$$\boldsymbol{\sigma} = \boldsymbol{\sigma}_d + \boldsymbol{\sigma}_s \ . \tag{C.61}$$

σ_d and σ_s are called *spheroidal* and *deviatoric* stresses respectively.

In the same way, strain tensor is split into dilatation (spheroidal) and shear (deviatoric) strains as:

$$\boldsymbol{\epsilon} = \begin{bmatrix} \epsilon_{11} & \epsilon_{12} & \epsilon_{13} \\ \epsilon_{21} & \epsilon_{22} & \epsilon_{23} \\ \epsilon_{31} & \epsilon_{32} & \epsilon_{33} \end{bmatrix} = \frac{1}{3}\epsilon_{ii}\boldsymbol{I} + \frac{1}{3}\begin{bmatrix} 2\epsilon_{11} - \epsilon_{22} - \epsilon_{33} & \epsilon_{12} & \epsilon_{13} \\ \epsilon_{21} & -\epsilon_{11} + 2\epsilon_{22} - \epsilon_{33} & \epsilon_{23} \\ \epsilon_{31} & \epsilon_{32} & -\epsilon_{11} - \epsilon_{22} + 2\epsilon 33 \end{bmatrix} \tag{C.62}$$

which can be rewritten as:

$$\boldsymbol{\epsilon} = \boldsymbol{\epsilon}_d + \boldsymbol{\epsilon}_s \ . \tag{C.63}$$

If the stress field is equal to a hydrostatic stress plus a pure shear stress field, the equations are simplified, so that the diagonal elements of the shear stress tensor vanish. In that case, and for an isotropic material, the diagonal elements of the strain tensor vanish too and:

$$\boldsymbol{\sigma} = \sigma_{11}\boldsymbol{I} + \begin{bmatrix} 0 & \sigma_{12} & \sigma_{13} \\ \sigma_{21} & 0 & \sigma_{23} \\ \sigma_{31} & \sigma_{32} & 0 \end{bmatrix} , \tag{C.64}$$

$$\boldsymbol{\epsilon} = \epsilon_{11}\boldsymbol{I} + \begin{bmatrix} 0 & \epsilon_{12} & \epsilon_{13} \\ \epsilon_{21} & 0 & \epsilon_{23} \\ \epsilon_{31} & \epsilon_{32} & 0 \end{bmatrix} . \tag{C.65}$$

The same general relation as in the one dimensional case exists for three dimensional viscoelastic materials. What differs from the one dimensional case is that the type of viscoelastic behavior may be different for spheroidal and deviatoric parts. This is reflected in the formulation by the separation of the constitutive equations. Thus $\boldsymbol{P}$ and $\boldsymbol{Q}$ in eqs. (C.46) and (C.54) could are split into spheroidal and deviatoric parts as follows:

$$\begin{array}{l} \boldsymbol{P}_d\sigma = \boldsymbol{Q}_d\epsilon \ (\sigma := \frac{1}{3}\sigma_{ii} \ ; \ \epsilon := \frac{1}{3}\epsilon_{ii}) \\ \boldsymbol{P}_s\sigma_{ij} = \boldsymbol{Q}_s\epsilon_{ij} \ (i \neq j) \end{array} \tag{C.66}$$

where $\sigma := \frac{1}{3}\sigma_{ii}$, $\epsilon := \frac{1}{3}\epsilon_{ii}$ and indices d and s represent spheroidal and deviatoric parts respectively. In the Laplace transform domain we obtain:

$$\begin{array}{l} \boldsymbol{P}_d\bar{\sigma} = \boldsymbol{Q}_d\bar{\epsilon} \ , \\ \boldsymbol{P}_s\bar{\sigma}_{ij} = \boldsymbol{Q}_s\bar{\epsilon}_{ij} \ (i \neq j) \ . \end{array} \tag{C.67}$$

In many earth models, the dilatation is assumed elastic, while a Maxwell fluid is considered in shear deformation.

References

Aki K. and P.G. Richards, 1980. Quantitative Seismology, Theory and Methods. W.H. Freeman and Company.

Amelung F. and D. Wolf, 1994. Viscoelastic perturbations of the earth: significance of the incremental gravitational force in models of glacial isostasy. Geophys. J. Int., 117: 864-879.

Anzidei M., P. Baldi, G. Casula, M. Crespi and F. Riguzzi, 1996. Repeated GPS Surveys across the Ionian Sea: Evidence of Crustal Deformations. Geophys. J. Int., 127: 257-267.

Arnadottir T. and P. Segall, 1994. The 1989 Loma Prieta Earthquake Imaged from Inversion of Geodetic Data. J. Geophys. Res., 99: 21835-21855.

Arnadottir T., P. Segall and Delaney, 1991. A Fault Model for the 1989 Kilauea South Flank Earthquake from Leveling and Seismic Data. Geophys. Res. Let., 18, 2217-2220.

Barrientos S.E. and S.N. Ward, 1990. The 1960 Chile Earthquake: Inversion for Slip Distribution from Surface Deformation. Geophys. J. Int., 103: 589-598.

Båth M., 1973. Introduction to Seismology. Birkhaeuser Verlag.

Ben-Menahem, A. and S.J. Singh, 1981. Seismic Waves and Sources. Springer Verlag.

Bennett R.A., W. Rodi and R.E. Reilinger, 1996. Global Positioning System Constraints on Fault Slip Rates in Southern California and Northern Baja, Mexico. J. Geophys. Res, 101: 21943-21960.

Bock Y., S. Wdowinski, P. Fang, J. Zhang, S. Williams, H. Johnson, J. Behr, J. Genrich, J. Dean, M. van Domselaar, D. Agnew, F. Wyatt, K. Stark, B. Oral, K. Hudnut, R. King, T. Herring, S. Dinardo, W. Young, D. Jackson and W. Gurtner, 1997. Southern California Permanent GPS Geodetic Array: Continuous Measurements of Regional Crustal Deformation between the 1992 Landers and 1994 Northridge Earthquakes. J. Geophys. Res., 102: 18013-18033.

Bonafede M., M. Dragoni and F. Quareni, 1986. Displacement and Stress Fields Produced by a Centre of Dilation and by a Pressure Source in a Viscoelastic Half-Space: Application to the Study of Ground Deformation and Seismic Activity at Campi Flegrei, Italy. Geophys. J. R. astr. Soc., 87: 455-485.

Bouchon M., 1981. A Simple Method to Calculate Green's Function for Elastic Layered Media. Bull. Seism. Soc. Am., 71: 959-971.

Brechkovski, L.M. and V. Goncharov, 1994. Mechanics of Continuua and Wave Dynamics. Springer.

Buergmann R., P. Segall, M. Lisowski and J. Svarc, 1997. Post-seismic Strain Following the 1989 Loma Prieta Earthquake from GPS and Leveling Measurements. J. Geophys. Res., 102: 4933-4955.

Chinnery M.A., 1961. The Deformation of the Ground around Surface Faults. Bull. Seism. Soc. Am., 51: 355-372.

Chinnery M.A. 1963. The Stress Changes That Accompany Strike-Slip Faulting, Bull. Seism. Soc. Am., 53: 921-932.

Chinnery M.A. and D.B. Jovanovich, 1972. Effect of Earth Layering on Earthquake Displacement Fields. Bull. Seism. Soc. Am., 62: 1629-1639.

Cohen S.C., 1979. Postseismic Surface Deformations due to Lithospheric and Asthenospheric Viscoelasticity. Geophys. Res. Let., 6: 129-131.

Duquesnoy T., O. Bellier, M. Kassar, M. Sébrier, C. Vigny and I. Bahar, 1996. Deformation Related to the 1994 Liwa Earthquake Derived from Geodetic Measurements. Geophys. Res. Let., 23: 3055-3058.

Dziewonski A.M. and D.L. Anderson, 1981. Preliminary Reference Earth Model. Phys. Earth Plan. Inter., 25: 297-356.

Ekström G. and P. England 1989. Seismic Strain Rates in Regions of Distributed Continental Deformation. J. Geophys. Res., 94: 10231-10257.

Engels, J., 1991. Eine Approximative Loesung der Fixen Gravimetrischen Randwertaufgabe im Innen- und Aussenraum der Erde. Ph.D. thesis, Verlag der Bayerischen Akademie der Wissenschaften, Reihe C, Heft Nr. 379.

Eringen A.C., 1980. Mechanics of Continua. Robert E. Krieger Publishing Company.

Eshelby J.D., 1957. The determination of Elastic Field of an Ellipsoid Inclusion, and Related Problems. Proceedings of the Royal Society of London, A241: 376-396.

Fernández J., T.T. Yu and J.B. Rundle, 1996a. Horizontal Viscoelastic-Gravitational Displacement due to a Rectangular Dipping Thrust Fault in a Layered Earth Model. J. Geophys. Res., 101: 13581-13594.

Fernández J., T.T. Yu and J.B. Rundle 1996b. Deformation Produced by a Rectangular Dipping Fault in a Viscoelastic-Gravitational Layered Earth Model. Part I: Thrust Fault - FLTGRV and FLTGRH Fortran Programs. Computers and Geosciences, 22: 735-750.

Flügge W., 1975. Viscoelasticity. Second Edition, Springer-Verlag.

Grafarend E., 1977. Stress-Strain Relations in Geodetic Networks. Communications from the Geodetic Institute Uppsala University, Uppsala.

Grafarend E. ,1986. Three Dimensional Deformation Analysis: Global Vector Spherical Harmonic and Local Finite Element Representation. Tectonophysics, 130: 337-359.

Hibbit, Karlsson and Sorensen, Inc. 1995. ABAQUS/Standard, User's Manual, 2 volumes.

Hunstad I., M. Anzidei, M. Cocco, P. Baldi and A. Galvani, 1999. Modelling Coseismic Displacements During the 1997 Umbria-Marche Earthquake (Central Italy). Geophys. J. Int, 139: 283-295.

Iwasaki T. and M. Matsu'ura, 1981. Quasi-Static Strains and Tilts due to Faulting in a Layered Half-Space with an Intervenient Viscoelastic Layer. J. Phys. Earth, 29: 499-518, 1981.

Jackson D.D., Z.K. Shen, D. Potter, X.B. Ge and L.Y. Sung, 1997. Southern California Deformation. Science, 277: 1621-1622.

Jeffreys H., 1970. The Earth. Cambridge University Press.

Johnson H.O. and F. Wyatt, 1994. Geodetic Network Design for Fault-Mechanics Studies. Manus. Geod., 19: 309-323.

Jovanovic D.B., M.I. Husseini and M. Chinnery, 1974a. Elastic Dislocations in a Layered Half-Space-I. Basic Theory and Numerical Methods. Geophys. J. R. astr. Soc., 39: 205-217.

Jovanovic D.B., M.I. Husseini and M. Chinnery, 1974b. Elastic Dislocations in a Layered Half-Space-II. The Point Source. Geophys. J. R. astr. Soc., 39: 219-239.

Kagan Y.Y., 1987a. Point Sources of Elastic Deformation: Elementary Sources, Static Displacements. Geophys. J. R. astr. Soc., 90: 1-34.

Kagan Y.Y., 1987b. Point Sources of Elastic Deformation: Elementary Sources, Static Displacements. Geophys. J. R. astr. Soc., Vol. 91: 891-912.

Kato T., G.S. El-Fiky and E.N. Oware, 1998. Crustal Strains in the Japanese Islands as Deduced from Dense GPS Array. Geophys. Res. Let., 25: 3445-3448.

Kenner S.J. and P. Segall, 2000. Postseismic Deformation Following the 1906 San Francisco Earthquake. J. Geophys. Res., 105: 13195-13209.

Knopoff L. and F. Gilbert, 1959. Radiation from a Strike Slip Fault. Seism. Soc. Am. Bull., 49: 163.

Knopoff L. and F. Gilbert, 1960. First Motion from Seismic Sources, Seis. Soc. Am. Bull., 50: 117.

Kostrov V.V and S. Das, 1988. Principles of Earthquakes Source Mechanics. Cambridge University Press.

Kreyszig E., 1993. Advanced Engineering Mathematics., 7th edition, John Wiley and Sons.

Lisowski M., W.H. Prescott, J.C. Savage and M.J. Johnston, 1990. Geodetic Estimate of Coseismic Slip During the 1989 Loma Prieta, California, Earthquake. Geophys. Res. Let., 17: 1437-1440.

Martinec Z. and D. Wolf, 1999. Gravitational Viscoelastic Relaxation of Eccentrically Nested Sphere. Geophys. J. Int. 138: 45-66.

Maruyama T., 1964. Static Elastic Dislocations in an Infinite and Semi-Infinite Medium. Bull. Earthquake Res. Inst. Univ. Tokyo, 42: 289-368.

Mase G.E., 1970. Continuum Mechanics, Schaum's Outline Series, McGraw Hill Book Company.

Matsu'ura M. and T. Tanimoto, 1980. Quasi-Static Deformations due to an Inclined, Rectangular Fault in a Viscoelastic Half-Space. J. Phys. Earth, 28: 103-118.

Miyazaki S., T. Saito, M. Sasaki, Y. Hatanaka and Y. Iimura, 1997. Expansion of GSI's Nationwide GPS Array. Bull. Geogr. Surv. Inst., 43: 23-34.

Okada Y., 1985. Surface Deformation due to Shear and Tensile Faults in a Half-Space. Bull. Seism. Soc. Am., 75: 1135-1154.

Okubo S., 1993. Reciprocity Theorem to Comute the Static Deformation due to a Point Dislocation Buried in a Spherically Symmetric Earth. Geophys. J. Int. 115: 921-928.

Pavlov V.M., 1994a. On Non-uniqueness of the Inverse Problem for a Seismic Source-I. Treatment in terms of Equivalent Force. Geophys. J. Int., 119: 479-486.

Pavlov V.M., 1994b. On Non-uniqueness of the Inverse Problem for a Seismic Source-I. Treatment in terms of Polynomial Moments. Geophys. J. Int., 119: 487-496.

Piersanti A., G. Spada, R. Sabadini and M. Bonafede, 1995. Global Post-Seismic Deformation. Geophys. J.Int., 120: 544-566.

Pipkin A.C., 1986. Lectures on Viscoelasticity. Springer Verlag, Second Edition, 1986.

Pollitz F.F., 1997. Gravitational Viscoelastic Postseismic Relaxation on a Layered Spherical Earth. J. Geophys. Res., 192: 17291-17942.

Roth F., 1990. Subsurface Deformations in a Layered Media. Geophys. J. Int., 103: 147-155.

Roth F., 1993. New Methods Using Dislocation Theory. Proceedings of the CRCM 93, Kobe: 265-274.

Runcorn K., 1967. International Dictionary of Geophysics. Pergamon Press.

Rundle J.B. and D.D. Jackson 1977. A Three-Dimensional Viscoelastic Model of a Strike Slip Fault. Geophys. J. R. astr. Soc., 49: 575-591.

Sabadini R. and L.L.A. Vermeersen, 1997. Influence of Lithospheric and Mantle Stratification on Global Post-Seismic Deformation. Geophys. Res. Let., 24: 2075-2078.

Segall P. and M. Matthews, 1997. Time Dependent Inversion of Geodetic Data. J. Geophys. Res., 102: 22391-22409.

Smylie D.E. and L. Mansinha, 1971. The Elasticity Theory of Dislocations in Real Earth Models and Changes in the Rotation of the Earth. Geophys. J. R. astr. Soc. 23: 329-354.

Soldati G, A. Piersanti and E. Boschi, 1998. Global Postseismic Gravity Changes of a Viscoelastic Earth. J. Geophys. Res., 103: 29867-29885.

Steketee J.A., 1958. On Volterra's Dislocation in a semi-infinite elastic medium. Can. J. Phys. 36: 192-205.

Stokes G.G., 1883. Mathematical and Physical Papers. II, Cambridge, the University Press.

Sun W., 1992. Potential and Gravity Changes Caused by Dislocations in Spherically Symmetric Earth Models. Bull. Earthquake Res. Inst. Tokyo, 67: 89-238.

Sun W. and S. Okubo, 1993. Surface Potential and Gravity Changes due to Internal Dislocations in a Spherical Earth-I. Theory for a Point Source. Geophys. J. Int., 114: 569-592.

Sun W., S. Okubo and P. Vaníček, 1996. Global Displacements Casued by Dislocations in a Realistic Earth Model. J. Geophys. Res., 101: 8561-8577.

Szameitat, H.J. 1979. Modell einer elastischen Erde auf der Grundlage finiter Kugelschalen-Elemente. Deutsche Geoätische Kommission, C 249.

Vermeersen L.L.A, R. Sabadini and G.Spada, 1996a. Compressible Rotational Deformation. Geophys. J. Int., 126: 735-761.

Vermeersen L.L.A, R. Sabadini and G.Spada, 1996b. Analytical Visco-Elastic Relaxation Models. Geophys. Res. Let., 23: 679-700.

Vvedenskaya A.V., 1959. The Displacement Field Associated with Discontinuities in an Elastic Medium. Investia Akad. Nauk. S.S.S.R., Ser. Gefiz. 516: 357-362 in English edition, American Geophysical Union.

Wdowinski S., Y. Bock, J. Zhang, P. Fang and J. Genrich, 1997. Southern California Permanent GPS Geodetic Array: Spatial Filtering of Daily Positions for Estimating Coseismic and Postseismic Displacements Induced by the 1992 Landers Earthquake. J. Geophys. Res., 102: 18057-18070.

Williams C.R., T. Arnadottir and P. Segall, 1993. Coseismic Deformation and Dislocation Models of the 1989 Loma Prieta Earthquake Derived from Global Positioning System Measurements. J. Geophys. Res., 98: 4567-4578.

Wolf D., 1984. The Relaxation of Spherical and Flat Maxwell Earth Models and Effects due to the Presence of the Lithosphere. J. Geophys., 56: 24-33.

Wolf D., 1993. The Changing Role of the Lithosphere in Models of Glacial Isostasy: a Historical Review. Global and Planetary Change, 8: 95-106.

Wolf D., 1997. Gravitational Viscoelastodynamics for a Hydrostatic Planet. Deutsche Geodaetische Kommission, C 452.

Yoshida S. and K. Koketsu 1990. Simultaneous Inversion of Waveform and Geodetic Data for the Rupture Process of the 1984 Naganoken-Seibu, Japan, Earthquake. Geophys. J. Int., 103: 355-362.

Zhang J., Y. Bock, H. Johnson, P. Fang, S. Williams, J. Genrich, S. Wdowinski and J. Behr, 1997. Southern California Permanent GPS Geodetic Array: Error Analysis of Daily Position Estimates and Site Velocities. J. Geophys. Res., 102: 18035-18055.